



# Sterile Neutrinos and Non-Standard Interactions in Neutrino Telescopes

Martin Sjöborg

Particle and Astroparticle Physics, Department of Physics  
Royal Institute of Technology, SE-106 91 Stockholm, Sweden

Stockholm, Sweden 2021

Examensarbete för avläggande av masterexamen i Teknisk fysik, inom ämnesområdet teoretisk fysik.

Master's thesis for the degree of Master of Science, in the subject area of Theoretical Physics.

TRITA-SCI-GRU 2021:042

© Martin Sjöborg, December 2021

# Abstract

The failure of the Standard Model of particle physics to predict neutrino masses invites us to amend it. We have no reason to believe that the interactions currently described by the gauge group are the whole picture, nor should we expect that the number of fermions hitherto observed is correct. In this thesis, we explore two amendments to the Standard Model, and examine whether either of these are consistent with measured data.

Firstly, we consider the sterile neutrino, which has no interactions described by the Standard Model. We examine the effect of this new fermion on the neutrino oscillation probabilities, and present what could be a detectable signal in the TeV energy range. Secondly, we consider interactions beyond the Standard Model, possibly stemming from a higher-order theory. We show how the parameters of these Non-Standard Interactions (NSI) can modify the oscillation probabilities and within which energy range we expect to discern this signal. We use data from and simulate event counts in two Cherenkov detectors: IceCube and DeepCore. Moreover, we generate data and simulate a proposed upgrade of the DeepCore detector: PINGU.

Using IceCube track events, we obtain best-fit values  $\Delta m_{41}^2 = 0.01 \text{ eV}^2$  and  $\theta_{24} = 0.67$  for our sterile neutrino hypothesis at a p-value of 20%, which is not statistically significant. Hence, we found no evidence of a sterile neutrino in IceCube data. Moreover, we were unable to distinguish a signal from  $\theta_{34}$  in our IceCube simulation. We obtain stringent bounds on the NSI parameters and compare those to previous results in literature. We show that PINGU is expected to narrow the bound further on  $\epsilon_{\mu\tau}$ , especially by considering a joint analysis with IceCube and DeepCore. Finally, we see that an anti-correlation between  $\epsilon_{e\mu}$  and  $\epsilon_{e\tau}$  at probability level was propagated down to event level, which we expect to be observable by PINGU.



# Sammanfattning

Misslyckandet med partikelfysikens s.k. standardmodell att förutsäga neutrinosensor tvingar oss att ändra den. Vi har ingen anledning att tro att de interaktioner som för närvarande beskrivs av standardmodellens symmetrigrupp är hela bilden, och vi bör inte heller förvänta oss att antalet fermioner som hittills observerats. I detta examensarbete undersöker vi två modifieringar av standardmodellen och undersöker om dessa ändringar är förenliga med uppmätta data. Först introducerar vi den sterila neutrinoen, som inte har några interaktioner som beskrivs av standardmodellen. Vi undersöker effekten av denna nya fermion på neutrinoskensationssannolikheterna, och presentera vad som skulle vara en detekterbar signal i TeV-området. Vidare introducerar vi en ny interaktion som vi kallar Icke-Standard Interaktioner (NSI), som möjligt härrör från en högre ordningens teori. Vi visar hur NSI-parametrarna kan modifiera skensationssannolikheterna, och inom vilka energiområden vi förväntar oss att urskilja denna signal.

Vi samlar in data från och simulerar två Cherenkov-detektorer: IceCube och DeepCore. Dessutom presenterar vi resultat som vi kan förvänta sig att se i en kommande uppgradering av DeepCore-detektorn: PINGU.

Vi får resultat som indikerar att den aktuella 3+0-hypotesen överensstämmer med IceCube-data, med bästa anpassningsvärdet  $\Delta m_{41}^2 = 0.01 \text{ eV}^2$  och  $\theta_{24} = 0.67$  med ett p-värde på 33%. Vi kunde inte skilja en signal från  $\theta_{34}$ . Vi erhåller strängt gränser för NSI-parametrarna och jämför dem med tidigare resultat. Vi visar att PINGU förväntas minska gränsen ytterligare hos  $\epsilon_{\mu\tau}$ , särskilt genom att gemensamt analysera resultaten med IceCube och DeepCore. Slutligen ser vi att en anti-korrelation mellan  $\epsilon_{e\mu}$  och  $\epsilon_{e\tau}$  på sannolikhetsnivå spreds ner till händelsenivå, vilket kommer att kunna observeras av PINGU.



# Acknowledgements

The computations were enabled by resources provided by the Swedish National Infrastructure for Computing (SNIC) at HPC2N, Umeå University and NSC, Linköping University. The resources were partially funded by the Swedish Research Council through grant agreement no. 2018-05973



# Contents

Abstract . . . . .	iii
Sammanfattning . . . . .	v
Acknowledgements . . . . .	vii
<b>Contents</b>	<b>viii</b>
<b>1 Introduction</b>	<b>1</b>
1.1 Outline . . . . .	1
<b>2 Neutrino Oscillations</b>	<b>3</b>
2.1 The Standard Model . . . . .	4
2.1.1 Beyond the Standard Model . . . . .	5
2.2 Mass Generation . . . . .	5
2.3 Neutrino Mixing . . . . .	8
2.3.1 The Mixing Matrix . . . . .	8
2.3.2 Neutrino Propagation . . . . .	9
2.3.3 Neutrino Oscillations in Matter . . . . .	13
2.3.4 The Three Neutrino Picture . . . . .	17
2.3.5 Earth Propagation . . . . .	19
2.3.6 The Two Neutrino Picture . . . . .	23
<b>3 The Antarctic Detectors</b>	<b>27</b>
3.1 Atmospheric Neutrino Flux . . . . .	28
3.2 Neutrino Detection . . . . .	29
3.2.1 True and Reconstructed Parameters . . . . .	32
3.3 IceCube . . . . .	33
3.4 DeepCore . . . . .	39
3.5 PINGU . . . . .	39
<b>4 Beyond the <math>3\nu</math> Picture</b>	<b>41</b>
4.1 The Sterile State . . . . .	42
4.1.1 The Hamiltonian . . . . .	42
4.1.2 The Probability Effect of a Sterile Neutrino . . . . .	44
4.2 Non-Standard Interactions . . . . .	47

4.2.1	Non-Standard Effects on Neutrino Matter Interactions . . . . .	47
4.2.2	IceCube Signal . . . . .	49
4.2.3	DeepCore and PINGU Signals . . . . .	50
<b>5</b>	<b>Results</b>	<b>55</b>
5.1	The Sterile Neutrino Hypothesis . . . . .	56
5.1.1	$\chi^2$ Minimization . . . . .	56
5.1.2	Sterile Mass and Mixing . . . . .	57
5.2	The NSI Hypothesis . . . . .	61
5.2.1	$\chi^2$ Minimization . . . . .	61
5.2.2	Constraining the NSI parameters . . . . .	62
<b>6</b>	<b>Conclusion</b>	<b>73</b>
<b>Bibliography</b>		<b>77</b>

# Chapter 1

## Introduction

There is no reason for us to believe that our current knowledge in particle physics is complete. The most successful framework – the Standard Model – has notable shortcomings. Neither does it explain why there is something rather than nothing<sup>1</sup>, nor does it give a candidate for dark matter<sup>2</sup>. To make matters even worse, three of the particles which are massless according to the Standard Model have been observed to actually have mass. In this thesis, we focus on the said particles – the neutrinos – and propose extensions to the Standard Model related to them. We then compare the effects of these extensions with collected data to see if our new theory more closely describes Nature or not.

Ultimately, the purpose of this excursion is to guide future research where to uncover more accurate theories. Traces of this grander theory will be present as breadcrumbs scattered in Nature. We just need to know where and how carefully to look.

### 1.1 Outline

This thesis is outlined as follows. In Chapter 2, we briefly review the most relevant parts of the Standard Model that will be relevant for our extensions of it. Then we present the evidence and subsequent discovery of neutrino oscillations, which ultimately led to the 2015 Nobel prize in physics, along with the modifications to the Standard Model needed to accommodate the discovery. The reader is then introduced to a standard but detailed derivation of the neutrino mixing matrix and oscillation Hamiltonian, including the matter effects stemming from charged and neutral current weak interactions within the Earth.

---

<sup>1</sup>In the Standard Model, matter and antimatter come in pairs of one particle and one antiparticle. When interacting, antimatter *annihilates* the matter, resulting in pure light. Since the universe today contains matter, there must have been more matter than antimatter at the Big Bang. This baryon asymmetry is unexplained in the Standard Model.

<sup>2</sup>Dark matter is heavy matter which does not interact with electromagnetic radiation. No such particle exists in the Standard Model.

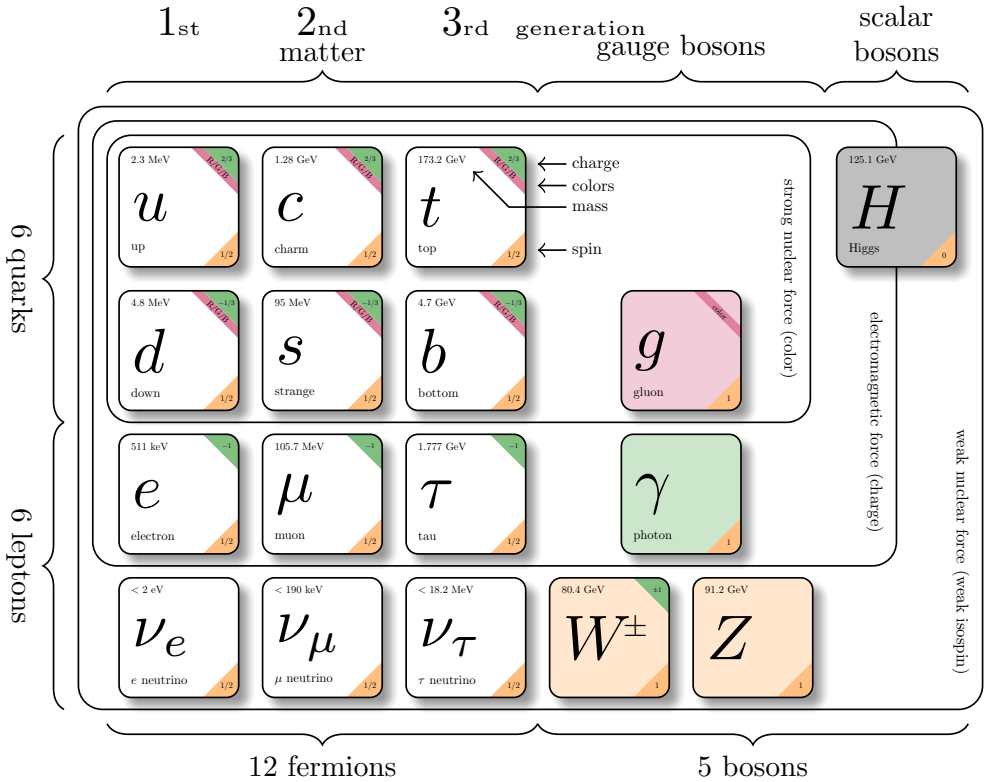
In Chapter 3, we present an experimental procedure used to observe signals from neutrinos originating from cosmic ray interactions in the atmosphere of the Earth. Furthermore, two Antarctic neutrino detectors are introduced: IceCube and DeepCore. We also summarize a proposed detector upgrade: Precision IceCube Next Generation Upgrade (PINGU), which we will use as a forecast in our analysis.

Chapter 4 consists of two parts. In Section 4.1, we consider a particle beyond the Standard Model: the sterile neutrino. We present how neutrino oscillations are modified by this hypothesized fourth neutrino and how these modifications would appear in IceCube if the particle is present in Nature. In Section 4.2, we set the sterile neutrino aside altogether and instead turn to the interactions between neutrinos and matter. We again amend the Standard Model by considering exotic interactions from a higher energy theory, manifesting themselves as sub-leading modifications to the matter potential. Since these new interactions are not present in the Standard Model, we call them non-standard interactions (NSI).

Finally, Chapter 5 contains the result from our two separate extensions of the Standard Model. In Section 5.1 we present our findings for the sterile neutrino. In Section 5.2, we present new constrained bounds on the NSI parameters compare those with literature.

## Chapter 2

# Neutrino Oscillations



## 2.1 The Standard Model

In order to describe the three quantizable forces of nature, we gather the mediators of each force – the vector bosons – into local (gauge) symmetry groups. Each vector boson has one corresponding generator, the set of which constitutes the group. The strong charge is mediated by eight massless gluons, which correspond to the eight independent generators of  $SU(3)_C$ . The weak charge is mediated by the three massive gauge bosons  $W^\pm$  and  $Z$ , and the massless photon  $\gamma$ , which constitute the generators of  $SU(2)_L$  and  $U(1)_Y$ .

The subscript of each group denotes by which mechanism that force is mediated. The gluons mediate the strong force through interactions of color, emphasized with subscript  $C$ . The weak force only sees left-handed particles, which we distinguish with the subscript  $L$ . And the electroweak interaction that a particle undergoes is determined by its hypercharge  $Y$ . For example, the quarks all have a non-zero color and non-zero hypercharge, so they participate in the strong and electromagnetic interactions. If a quark is left-handed, it will also feel the weak interaction. The neutrinos, on the other hand, have neither charge nor color, so they are invisible to

both the strong and electromagnetic force. We express this by letting their fields transform as singlets under those symmetry groups.

### 2.1.1 Beyond the Standard Model

Together, these three interactions make up the Standard Model gauge group  $SU(3)_C \times SU(2)_L \times U(1)_Y$ . This determines the form of the three coupling constants, which numerical values must be experimentally measured. Since the vector bosons are represented by the generators, they are uniquely determined by the symmetry group. However, the scalar boson(s) and fermions are free as long as they belong to representations of the symmetry group. By this construction, modifications to fermions rather than bosons are generally easier to make, allowing us to propose amendments to the model. Even the number of fermions must be experimentally verified and can be altered from a phenomenological standpoint. In this work, we will use this leniency to introduce a new particle and examine to which extent these modifications might be supported by experimental evidence. Moreover, we will examine the possibility of adding a new completely new interaction, which manifests itself as modifications to the neutrino-matter interactions.

## 2.2 Mass Generation

In the Standard Model, fermion masses are generated by the Higgs mechanism through Yukawa couplings with the fermion's right and left-handed components. All neutrinos are left-handed, and all antineutrinos are right-handed [1]. This observational fact is reflected in the left-handed lepton doublet and right-handed lepton singlet

$$L'_{\alpha L} = \begin{pmatrix} \nu'_{\alpha L} \\ \alpha'_L \end{pmatrix}, \quad \ell'_{\alpha R} = \alpha'_R, \quad (2.1)$$

where  $\alpha \in \{e, \mu, \tau\}$ , and the primes denotes that the fields do not have definite masses. The essential part here is that  $\nu'_{\alpha R}$  is missing from the right-handed lepton singlet. Thus, the neutrino fields do not pick up a Yukawa coupling, and will not undergo the Higgs mechanism, which leaves them massless. Moreover, all terms of a Lagrangian that we construct must respect the gauge invariance. This removes the possibility of the neutrino mass to be generated at loop level because any such attempt will violate the total lepton number by two units. In order to keep our theory renormalizable, we have one option left if we want to generate neutrino masses: introducing right-handed neutrino and left-handed antineutrino fields.

We consider a right-handed neutrino field,  $\nu'_R$ . Since the electroweak gauge group  $SU(2)_L \times U(1)_Y$  only couple to left-handed particles and right-handed antiparticles,

$\nu_R$  transforms as a singlet under the Standard Model symmetry group  $SU(3)_C \times SU(2)_L \times U(1)_Y$ .

We extend the Standard Model by adding a right-handed component of this field with neutrino Yukawa couplings  $Y_{\alpha\beta}^{\nu\nu}$  to the Higgs-lepton Yukawa part of the interaction Lagrangian

$$\mathcal{L}_{int} \subseteq - \left( \frac{v + H}{\sqrt{2}} \right) [\bar{\ell}'_{\alpha L} Y_{\alpha\beta}^{\nu\nu} \ell'_{\beta R} + \bar{\nu}'_{\alpha L} Y_{\alpha\beta}^{\nu\nu} \nu'_{\beta R}] , \quad (2.2)$$

where  $v$  is the Higgs vacuum expectation value,  $H$  the Higgs field,  $\ell'_{\alpha L} (\ell'_{\beta R})$  the left (right) handed charged lepton field, and summation over the lepton indices  $\alpha, \beta$  is implied.  $Y_{\alpha\beta}^{\nu\nu}$  are the charged lepton Yukawa couplings, and  $\nu'_{\alpha L} (\nu'_{\beta R})$  are the left (right) handed neutrino fields. Now, the Yukawa coupling matrices  $Y^{\ell\ell}$  and  $Y^{\nu\nu}$  are non-diagonal, as emphasized with their prime. This can be remedied by diagonalizing  $Y^{\ell\ell}$  with a biunitary transformation

$$V_L^{\ell\dagger} Y^{\ell\ell} V_R^\ell = Y^\ell . \quad (2.3)$$

where  $V_L^\ell$  and  $V_R^\ell$  are two unitary matrices. Similarly, we diagonalize and  $Y^{\nu\nu}$  with a unitary matrix  $V^\nu$ . Now we state a crucial difference between the properties of the charged lepton and the neutrino fields. While the charged lepton flavor eigenstate was uniquely determined by its mass eigenstate, the neutrino flavor is a superposition of mass eigenstates. This is because neutrinos are indirectly detected via the observation of its associated charged lepton, so there is no requirement for neutrino flavor eigenstates to have a definite mass. The flavor of a neutrino is then – by definition – the flavor of the associated charged lepton. This fact is denoted as giving the mass eigenstates Latin numerals and letters, while the flavor eigenstates stay as Greek letters.

So, let the neutrino field in the mass basis have components with Latin numerals to distinguish them from the flavour components, i.e

$$\nu_k = V_{k\beta}^{\nu\dagger} \nu'_\beta . \quad (2.4)$$

The diagonalized Lagrangian now takes the form

$$\begin{aligned} \mathcal{L}_{int} &\subseteq - \left( \frac{v + H}{\sqrt{2}} \right) [\bar{\ell}'_{\alpha L} Y_{\alpha\beta}^{\nu\nu} \ell'_{\beta R} + \bar{\nu}'_{\alpha L} Y_{\alpha\beta}^{\nu\nu} \nu'_{\beta R}] \\ &= - \left( \frac{v + H}{\sqrt{2}} \right) [\bar{\ell}'_{\alpha L} V_{\alpha\beta L}^\ell Y_{\alpha\beta}^{\ell\ell} V_{\alpha\beta R}^{\ell\dagger} \ell'_{\beta R} + \bar{\nu}'_{\alpha L} V_{\alpha k L}^\nu Y_{kj}^\nu V_{\beta j R}^{\nu\dagger} \nu'_{\beta R}] \\ &= - \left( \frac{v + H}{\sqrt{2}} \right) [\bar{\ell}_{\alpha L} Y_{\alpha\beta}^{\ell\ell} \ell_{\beta R} + \bar{\nu}_{k L} Y_{kj}^\nu \nu_{j R}] \\ &= - \left( \frac{v + H}{\sqrt{2}} \right) [\bar{\ell}_{\alpha L} Y_{\alpha\beta}^{\ell\ell} \ell_{\beta R} + \bar{\nu}_{k L} Y_{kj}^\nu \nu_{j R}] \end{aligned} \quad (2.5)$$

By construction,  $Y^\ell$  and  $Y^\nu$  are diagonal, so we write their components as  $y_\alpha^\ell \delta_{\alpha\beta}$  and  $y_k^\nu \delta_{kj}$  respectively, leaving the Lagrangian as

$$\begin{aligned}\mathcal{L}_{int} &\subseteq -\left(\frac{v+H}{\sqrt{2}}\right) [\bar{\ell}_{\alpha L} y_\alpha^\ell \delta_{\alpha\beta} \ell_{\beta R} + \bar{\nu}_{k L} y_k^\nu \delta_{kj} \nu_{j R}] \\ &= -\left(\frac{v+H}{\sqrt{2}}\right) [\bar{\ell}_{\alpha L} y_\alpha^\ell \ell_{\alpha R} + \bar{\nu}_{k L} y_k^\nu \nu_{k R}] \\ &= -\left(\frac{v+H}{\sqrt{2}}\right) [y_\alpha^\ell \bar{\ell}_{\alpha L} \ell_{\alpha R} + y_k^\nu \bar{\nu}_{k L} \nu_{k R}]\end{aligned}\quad (2.6)$$

Now, by the introduction of the right-handed field  $\nu_R$ , the Dirac neutrino field is

$$\nu_k = \nu_{k L} + \nu_{k R}. \quad (2.7)$$

Multiplying  $\nu_k$  with its conjugate  $\bar{\nu}_k$ , we get

$$\begin{aligned}\bar{\nu}_k \nu_k &= \bar{\nu}_{k L} \nu_{k L} + \bar{\nu}_{k R} \nu_{k L} + \bar{\nu}_{k L} \nu_{k R} + \bar{\nu}_{k R} \nu_{k R} \\ &= \bar{\nu}_{k L} \nu_{k R} + \bar{\nu}_{k R} \nu_{k L} \\ &= \bar{\nu}_{k L} \nu_{k R} + \text{h.c.}\end{aligned}\quad (2.8)$$

The same calculation for the charged lepton field yields the same result for  $\ell_k$ . Substituting this result and multiplying the Higgs vacuum expectation value  $v$  into the fields gives us

$$\begin{aligned}\mathcal{L}_H &= -\left(\frac{v+H}{\sqrt{2}}\right) [y_\alpha^\ell \bar{\ell}_{\alpha L} \ell_{\alpha R} + y_k^\nu \bar{\nu}_{k L} \nu_{k R}] \\ &= -\frac{y_\alpha^\ell v}{\sqrt{2}} \bar{\ell}_{\alpha L} \ell_{\alpha R} - \frac{y_k^\nu v}{\sqrt{2}} \bar{\nu}_{k L} \nu_{k R} - \frac{y_\alpha^\ell}{\sqrt{2}} \bar{\ell}_{\alpha L} \ell_{\alpha R} H - \frac{y_k^\nu}{\sqrt{2}} \bar{\nu}_{k L} \nu_{k R} H.\end{aligned}\quad (2.9)$$

Thus, this extension to the SM generates by the Higgs mechanism neutrino masses with terms

$$m_k = \frac{y_k^\nu v}{\sqrt{2}}, \quad (2.10)$$

where the Yukawa couplings  $y_k^\nu$  needs to be experimentally determined.

## 2.3 Neutrino Mixing

Japan 1998. The Super-Kamiokande experiment detects a  $\nu_\mu$  deficit that could not be explained by any other mechanism than the conversion of muon neutrinos to electron neutrinos [2]. This was the first conclusive evidence of a completely new physics phenomenon: neutrino flavor oscillations. An implication of the observation of oscillations is neutrino mass, which is identically zero according to the Standard Model. Thus, we are required to extend the Standard Model to incorporate neutrino masses before we discuss the neutrino oscillations themselves.

### 2.3.1 The Mixing Matrix

Substituting the new transformation from Eq. 2.4 into the expression for the weak charged current, we get

$$\begin{aligned} j_L^\rho &= 2\bar{\nu}'_{\alpha L}\gamma^\rho\ell'_{\alpha L} \\ &= 2\bar{\nu}_{kL}V'^{\nu\dagger}_{k\alpha}V'^\ell_{\alpha\alpha}\gamma^\rho\ell_{\alpha L} \end{aligned} \quad (2.11)$$

Call  $V'^{\nu\dagger}_{k\alpha}V'^\ell_{\alpha\alpha} = U_{k\alpha}^\dagger$ . We will refer to the matrix  $U$  built by the components  $U_{k\alpha}$  as the (neutrino) mixing matrix. It can also be referred to as the Pontecorvo-Maki-Nakagawa-Sakata (PMNS) matrix [3, 4]. We now have

$$j_L^\rho = 2\sum_\alpha\sum_k U_{\alpha k}^\dagger\bar{\nu}_{kL}\gamma^\rho\ell_{\alpha L}. \quad (2.12)$$

We construct the PMNS matrix by parametrizing it with the rotation matrices  $R_{ij}$  and a matrix  $P_{Maj}$  as

$$\begin{aligned} U &= R_{23}R_{13,\delta_{CP}}R_{12}P_{Maj} \\ &= \begin{pmatrix} U_{e1} & U_{e2} & U_{e3} \\ U_{\mu 1} & U_{\mu 2} & U_{\mu 3} \\ U_{\tau 1} & U_{\tau 2} & U_{\tau 3} \end{pmatrix} \\ &= \begin{pmatrix} 1 & 0 & 0 \\ 0 & c_{23} & s_{23} \\ 0 & -s_{23} & c_{23} \end{pmatrix} \begin{pmatrix} c_{13} & 0 & s_{13}e^{-i\delta_{CP}} \\ 0 & 1 & 0 \\ -s_{13}e^{i\delta_{CP}} & 0 & c_{13} \end{pmatrix} \begin{pmatrix} c_{12} & s_{12} & 0 \\ -s_{12} & c_{12} & 0 \\ 0 & 0 & 1 \end{pmatrix} \begin{pmatrix} 1 & 0 & 0 \\ 0 & e^{i\lambda_2} & 0 \\ 0 & 0 & e^{i\lambda_3} \end{pmatrix} \\ &= \begin{pmatrix} c_{12}c_{13} & s_{12}c_{13} & s_{13}e^{-i\delta_{CP}} \\ -s_{12}c_{23} - c_{12}s_{23}s_{13}e^{i\delta_{CP}} & c_{12}c_{23} - s_{12}s_{23}s_{13}e^{i\delta_{CP}} & s_{23}c_{13} \\ s_{12}s_{23} - c_{12}c_{23}s_{13}e^{i\delta_{CP}} & -c_{12}s_{23} - s_{12}c_{23}s_{13}e^{i\delta_{CP}} & c_{23}c_{13} \end{pmatrix} \begin{pmatrix} 1 & 0 & 0 \\ 0 & e^{i\lambda_2} & 0 \\ 0 & 0 & e^{i\lambda_3} \end{pmatrix}, \end{aligned} \quad (2.13)$$

where  $s_{ij} = \sin(\theta_{ij})$ ,  $c_{ij} = \cos(\theta_{ij})$ ,  $0 \leq \theta_{ij} \leq \pi/2$  and  $0 \leq \lambda_i, \delta_{CP} \leq 2\pi$ .

By construction, it provides the unitary transformation between the flavor and mass bases. Any unitary  $3 \times 3$  matrix can be parametrized using three angles and

six phases. However, not all phases affect the charged and weak currents and are thus not observable by us. Moreover, both the Lagrangian and the currents are invariant under global  $U(1)$  transformations, leaving only one physical phase for us to measure: one term in the form of a Dirac CP-violating phase  $\delta_{\text{CP}}$ . However, if the neutrinos are Majorana fermions, the rephasing of the left-handed fields would cause the neutrino masses to become complex. Thus, we include two Majorana phases  $\lambda_2, \lambda_3$  in the PMNS matrix through  $P_{Maj}$ . These two phases are detectable in processes that violate lepton number, such as neutrinoless double  $\beta$  decay. Majorana phases are not detectable in neutrino oscillation experiments because oscillations are not violating lepton number, and a Majorana phase would violate lepton number by two units.

We are now down to six degrees of freedom in the three dimensional case: three angles of the form  $s_{ij}, c_{ij}$ , and three phase of the form  $e^{i\delta_{\text{CP}}}$  and  $e^{i\lambda_i}$ . The angle  $\theta_{ij}$  specifies the amount of rotation in the  $i - j$  plane. The physical interpretation of a mixing matrix element  $U_{ij}$  is then the degree to which the  $\nu_i$  mass eigenstate mixes with the  $\nu_j$  mass eigenstate. Thus we refer to  $\theta_{ij}$  as the mixing angles. A non-zero mixing angle will then cause the flavor eigenstate  $\nu_\alpha$  to be a superposition of the mass eigenstates  $\nu_i$  that we allowed to mix. More on this in Section 2.3.2.

### 2.3.2 Neutrino Propagation

Since we now know how the neutrino mass and flavor eigenstates combine and have an expression for the flavor interaction with the neutrinos charged lepton partner, we are now ready to study the flavor oscillations themselves.

From the expression for the weak charged current in 2.12, we see that the summation over the mass index  $k$  with the mixing matrix elements constructs a flavor neutrino, which interacts with the charged lepton field  $\ell_{\alpha L}$ . In other words, the charged current generates a flavor neutrino  $\nu_\alpha$ , which is a superposition of the mass eigenstates  $\nu_k$  with weights  $U_{\alpha k}^*$ . In the ket-formalism, we express this as

$$|\nu_\alpha\rangle = \sum_k U_{\alpha k}^* |\nu_k\rangle . \quad (2.14)$$

It is the mass eigenstates  $|\nu_k\rangle$  that are eigenstates of the Hamiltonian, with eigenvalues

$$E_k = \sqrt{\vec{p}^2 + m_k^2} . \quad (2.15)$$

The solution to the time-dependent Schrödinger equation

$$i \frac{d}{dt} |\nu_k(t)\rangle = H_0 |\nu_k(t)\rangle , \quad (2.16)$$

where  $H_0$  is the vacuum Hamiltonian. The solution to Eq. 2.16 gives us the time evolution in the form of plane wave solutions:

$$|\nu_k(t)\rangle = e^{-iE_k t} |\nu_k\rangle . \quad (2.17)$$

Inserting the plane wave solution into Eq. 2.14, we get

$$|\nu_\alpha(t)\rangle = \sum_k U_{\alpha k}^* e^{-iE_k t} |\nu_k\rangle . \quad (2.18)$$

Now we know how to evolve and combine the mass eigenstates to form a flavor eigenstate, but how about the reverse? We swap the index  $k \rightarrow j$  in Eq. 2.14 and multiply by  $U_{\alpha k}$ :

$$\begin{aligned} \sum_\alpha U_{\alpha k} |\nu_\alpha\rangle &= \sum_{\alpha, j} U_{\alpha k} U_{\alpha j}^* |\nu_j\rangle \\ &= \sum_j \delta_{kj} |\nu_j\rangle \\ &= |\nu_k\rangle , \end{aligned} \quad (2.19)$$

where we have used the unitarity of the leptonic mixing matrix. Eqs. 2.14 and 2.18 yield

$$\begin{aligned} |\nu_\alpha(t)\rangle &= \sum_k U_{\alpha k}^* e^{-iE_k t} |\nu_k\rangle \\ &= \sum_k U_{\alpha k}^* e^{-iE_k t} \left( \sum_\beta U_{\beta k} |\nu_\beta\rangle \right) \\ &= \sum_{k, \beta} U_{\alpha k}^* U_{\beta k} e^{-iE_k t} |\nu_\beta\rangle . \end{aligned} \quad (2.20)$$

The probability of the flavor transition  $\nu_\alpha \rightarrow \nu_\beta$  at time  $t$  is  $|\langle \nu_\beta | \nu_\alpha(t) \rangle|^2$ :

$$\begin{aligned} P_{\nu_\alpha \rightarrow \nu_\beta}(t) &= \sum_{k, j} |\langle \nu_\beta | \nu_\alpha(t) \rangle|^2 \\ &= U_{\alpha k}^* U_{\beta k} U_{\beta j}^* U_{\alpha j} e^{-i(E_k - E_j)t} . \end{aligned} \quad (2.21)$$

We assume the neutrino masses  $m_k$  to be extremely small compared to their associated energies  $E_k$ . Thus,  $v \approx 1$ , and  $|\vec{p}| \approx E$  making the energy-dispersion

relation of Eq. 2.15 to first order:

$$\begin{aligned} E_k &= \sqrt{\vec{p}^2 + m_k^2} \\ &= \vec{p}^2 \sqrt{1 + \frac{m_k^2}{\vec{p}^2}} \\ &\approx E + \frac{m_k^2}{2E} \end{aligned} \quad (2.22)$$

Hence, the exponential can be simplified, and simplifying the notation  $P_{\nu_\alpha \rightarrow \nu_\beta}(t) \rightarrow P_{\alpha\beta}(t)$  we get

$$P_{\alpha\beta}(t) = \sum_{k,j} |U_{\alpha k}^* U_{\beta k} U_{\beta j}^* U_{\alpha j}| e^{-i(m_k^2 - m_j^2)t/2E}. \quad (2.23)$$

Now, our approximation  $v \approx 1$  implies  $x \approx t$ , thus

$$\begin{aligned} P_{\alpha\beta}(x) &= \sum_{k,j} |U_{\alpha k}^* U_{\beta k} U_{\beta j}^* U_{\alpha j}| e^{-i(m_k^2 - m_j^2)x/2E} \\ &= \sum_{k,j} |U_{\alpha k}^* U_{\beta k} U_{\beta j}^* U_{\alpha j}| \exp\left(-i \frac{\Delta m_{kj}^2 x}{2E}\right), \end{aligned} \quad (2.24)$$

where we in the last step have defined the *mass-squared difference*  $\Delta m_{kj}^2 = m_k^2 - m_j^2$ . Since the oscillation probability depends on this quantity rather than the individual masses, it is impossible to measure the absolute mass  $m_k$  through neutrino oscillations. We have to rely on other types of experiments to get us at least one absolute mass, from which we then can calculate the remaining. Squaring the unitarity condition  $\sum_k U_{\alpha k} U_{\beta k}^* = \delta_{\alpha\beta}$  yields

$$\sum_k |U_{\alpha k}|^2 |U_{\beta k}|^2 = \delta_{\alpha\beta} - 2 \sum_{k>j} \text{Re}[U_{\alpha k}^* U_{\beta k} U_{\alpha j} U_{\beta j}^*] \quad (2.25)$$

We have

$$\begin{aligned}
P_{\alpha\beta} &= \sum_{k,j} |U_{\alpha k}^* U_{\beta k} U_{\beta j}^* U_{\alpha j}| \exp\left(-i \frac{\Delta m_{kj}^2 x}{2E}\right) \\
&= \sum_k |U_{\alpha k}|^2 |U_{\beta k}|^2 + \sum_{k \neq j} |U_{\alpha k}^* U_{\beta k} U_{\beta j}^* U_{\alpha j}| \exp\left(-i \frac{\Delta m_{kj}^2 x}{2E}\right) \\
&= \delta_{\alpha\beta} - 2 \sum_{k>j} \text{Re}[U_{\alpha k}^* U_{\beta k} U_{\alpha j} U_{\beta j}] + \sum_{k \neq j} |U_{\alpha k}^* U_{\beta k} U_{\beta j}^* U_{\alpha j}| \exp\left(-i \frac{\Delta m_{kj}^2 x}{2E}\right) \\
&= \delta_{\alpha\beta} - 4 \sum_{k>j} \text{Re}[U_{\alpha k}^* U_{\beta k} U_{\beta j}^* U_{\alpha j}] \sin^2\left(\frac{\Delta m_{kj}^2 x}{4E}\right) \\
&\quad + 2 \sum_{k>j} \text{Im}[U_{\alpha k}^* U_{\beta k} U_{\beta j}^* U_{\alpha j}] \sin\left(\frac{\Delta m_{kj}^2 x}{4E}\right), \tag{2.26}
\end{aligned}$$

which is the probability of neutrino vacuum oscillations. A similar calculation for antineutrinos yield

$$\begin{aligned}
P_{\alpha\beta} &= \delta_{\alpha\beta} - 4 \sum_{k>j} \text{Re}[U_{\alpha k}^* U_{\beta k} U_{\beta j}^* U_{\alpha j}] \sin^2\left(\frac{\Delta m_{kj}^2 x}{4E}\right) \\
&\quad - 2 \sum_{k>j} \text{Im}[U_{\alpha k}^* U_{\beta k} U_{\beta j}^* U_{\alpha j}] \sin\left(\frac{\Delta m_{kj}^2 x}{4E}\right). \tag{2.27}
\end{aligned}$$

This form elucidates an important aspect of neutrino oscillations. The mixing matrix elements determine the amplitude of the oscillations, while the mass-squared differences together with the ratio  $L/E$  determine the frequency. So in vacuum, the mixing angles only influence the oscillation amplitude, while the energy, trajectory, and masses of the neutrinos only influence the oscillation frequency.

Experimental measurements show that  $\theta_{13}$  is the smallest of the mixing angles [5], causing  $\nu_\mu$  to primarily mix into  $\nu_\tau$ . Using values from [5], but taking  $\delta_{CP} = 0$  for simplicity, the mixing matrix from 2.13 takes the values

$$U = \begin{pmatrix} U_{e1} & U_{e2} & U_{e3} \\ U_{\mu 1} & U_{\mu 2} & U_{\mu 3} \\ U_{\tau 1} & U_{\tau 2} & U_{\tau 3} \end{pmatrix} = \begin{pmatrix} 0.825 & 0.545 & 0.149 \\ -0.455 & 0.485 & 0.746 \\ 0.334 & -0.684 & 0.649 \end{pmatrix}, \tag{2.28}$$

which we use to plot the  $P_{\mu\beta}$  probabilities in Fig. 2.1. Here, we show the energy spectra of these oscillations in the low GeV range for neutrinos that travel  $12\,742\,\text{km}^1$ . In the left-most panel, we see a suppressed  $\nu_\mu \rightarrow \nu_e$  transition. We can understand this behavior by studying Eq. 2.26 and the numerical values of the mixing matrix in Eq. 2.28. The smallness of  $U_{e3}$  reduces the effect of  $\Delta m_{21}^2$  mass-squared difference,

---

<sup>1</sup>This baseline is the Earth diameter, and will, apart from the atmosphere, be the maximum travel distance which we will use later on.

allowing  $\Delta m_{31}^2$  to drive the oscillations. Thus, The most important mixing matrix elements for  $P_{\alpha\beta}$  are the ones appearing in the term with  $\Delta m_{31}^2$ : namely the product  $U_{\alpha 3}^* U_{\beta 3} U_{\beta 1}^* U_{\alpha 1}$ .

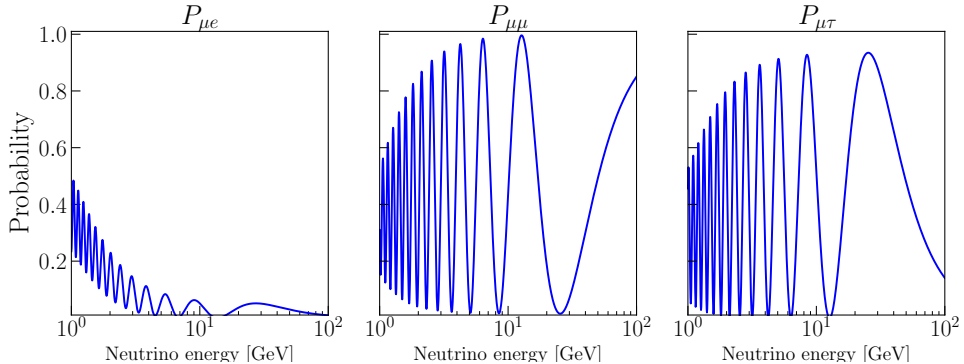


Figure 2.1: Probabilities of  $\nu_\mu$  oscillations after travelling 12 742 km in vacuum, using parameters from [5].

### 2.3.3 Neutrino Oscillations in Matter

So far, we have discussed neutrinos traveling in vacuum. Now we will concern ourselves with neutrino oscillations in matter. The possible interactions are shown in Fig. 2.2. The left panel shows that the only flavor that can undergo charged current (CC) interactions are the electron flavor. This is because the CC interaction requires a neutrino with flavor  $\alpha$  to interact with its charged lepton partner  $\alpha$ . Since the Earth does not consist of any muons or tau particles, the  $\nu_\mu$  and  $\nu_\tau$  have no charged leptons with which they can undergo CC interactions. The right panel shows any neutrino flavor interaction via the neutral current (NC) with matter, mediated by the neutral  $Z$  boson. The Earth is entirely composed of electrons, protons, and neutrons. Thus, the fundamental particles composing Earth are electrons, and up and down quarks. These are the fermions relevant for our matter oscillations. In these two diagrams, we see that the CC interactions happen in the flavor basis rather than in the mass basis. In other words, neutrinos propagate in their mass eigenstates but interact in their flavor eigenstate. The mixing of mass eigenstates during propagation determines if the flavor eigenstate has oscillated or not.

The interaction mediated by the  $W$  boson will give rise to an effective matter potential  $V_{CC}$ , while the  $Z$  boson is responsible for  $V_{NC}$ .

We start with the effective Hamiltonian for the CC process. The Feynman rules for the left panel give us

$$H_{CC} = \frac{G_F}{\sqrt{2}} [\bar{\nu}_e \gamma^\rho (1 - \gamma^5) e] [\bar{e} \gamma_\rho (1 - \gamma^5) \nu_e] \quad (2.29)$$

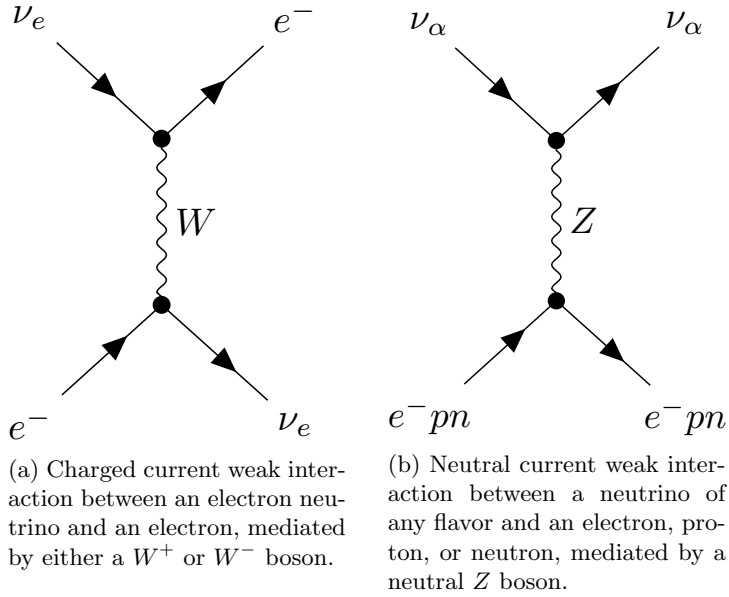


Figure 2.2: Feynmann diagrams showing neutrinos participating in the two types of weak interactions according to the Standard Model.

By using the Fierz transformation

$$\mathcal{L}^{V-A}(\psi_1, \psi_2, \psi_3, \psi_4) = \mathcal{L}^{V-A}(\psi_1, \psi_4, \psi_3, \psi_2), \quad (2.30)$$

we can permute the terms inside the brackets, yielding

$$H_{CC} = \frac{G_F}{\sqrt{2}} [\bar{\nu}_e \gamma^\rho (1 - \gamma^5) \nu_e] [\bar{e} \gamma_\rho (1 - \gamma^5) e]. \quad (2.31)$$

Now, lets consider a finite volume  $V$  with electron states defined as

$$|e(p_e, h_e)\rangle = \frac{1}{2E_e V} a_e^{(h_e)\dagger}(p_e) |0\rangle, \quad (2.32)$$

i.e. using the creation operator  $a_e^{(h_e)\dagger}(p_e)$  to create electron states from vacuum with momenta  $p_e$ , energy  $E_e$ , and helicity  $h_e$ . The density distribution of electrons in  $V$  is  $f(E_e, T)$ , which we normalize to the total number of electrons as we integrate out the momenta  $p_e$ :

$$\int dp_e^3 f(E_e, T) = N_e V = n_e \quad (2.33)$$

Here, the electron density  $N_e$  will ultimately determine the strength of the effective matter potential. To obtain the average effective Hamiltonian, project it on the

electron states in Eq. 2.32 and integrate over the density and sum over the helicities:

$$\begin{aligned}
\langle H_{CC} \rangle &= \int dp_e^3 \langle e(p_e, h_e) | \times \frac{1}{2} \sum_{h_e} H_{CC} f(E_e, T) | e(p_e, h_e) \rangle \\
&= \frac{G_F}{\sqrt{2}} \int dp_e^3 \langle e(p_e, h_e) | [\bar{\nu}_e \gamma^\rho (1 - \gamma^5) \nu_e] f(E_e, T) \\
&\quad \times \frac{1}{2} \sum_{h_e} [\bar{e}(x) \gamma_\rho (1 - \gamma^5) e(x)] | e(p_e, h_e) \rangle \\
&= \frac{G_F}{\sqrt{2}} \bar{\nu}_e \gamma^\rho (1 - \gamma^5) \nu_e \int dp_e^3 f(E_e, T) \\
&\quad \times \frac{1}{2} \sum_{h_e} \langle e(p_e, h_e) | \bar{e}(x) \gamma_\rho (1 - \gamma^5) e(x) | e(p_e, h_e) \rangle . \quad (2.34)
\end{aligned}$$

First, calculate the sum using trace technology

$$\begin{aligned}
\frac{1}{2} \sum_{h_e} \langle e(p_e, h_e) | \bar{e}(x) \gamma_\rho (1 - \gamma^5) e(x) | e(p_e, h_e) \rangle &= \frac{1}{4E_e V} \sum_{h_e} \bar{u}_e^{h_e}(p_e) \gamma_\rho (1 - \gamma^5) u_e^{h_e}(p_e) \\
&= \frac{1}{4E_e V} \text{Tr} \left[ \sum_{h_e} \bar{u}_e^{h_e}(p_e) u_e^{h_e}(p_e) \gamma_\rho (1 - \gamma^5) \right] \\
&= \frac{1}{4E_e V} \text{Tr} \left[ (\not{p}_e + m_e) \gamma_\rho (1 - \gamma^5) \right] \\
&= \frac{(p_e)_\rho}{E_e V} . \quad (2.35)
\end{aligned}$$

Eq. 2.34 now becomes

$$\langle H_{CC} \rangle = \frac{G_F}{\sqrt{2} E_e V} \bar{\nu}_e (1 - \gamma^5) \nu_e \int dp_e^3 \not{p}_e f(E_e, T) . \quad (2.36)$$

Expand the integral, and use the fact that  $\vec{p}_e$  is odd:

$$\begin{aligned}
\int dp_e^3 \not{p}_e f(E_e, T) &= \int dp_e^3 f(E_e, T) (\gamma^0 E_e - \vec{p}_e \cdot \vec{\gamma}) \\
&= \int dp_e^3 f(E_e, T) \gamma^0 E_e \\
&= \gamma_0 E_e N_e V . \quad (2.37)
\end{aligned}$$

Inserting this into Eq. 2.36, we have

$$\begin{aligned}
\langle H_{CC} \rangle &= \frac{G_F N_e}{\sqrt{2}} \bar{\nu}_e (1 - \gamma^5) \nu_e \gamma_0 \\
&= \sqrt{2} G_F N_e \bar{\nu}_{eR} \gamma^0 \nu_{eL} , \quad (2.38)
\end{aligned}$$

where the projection operator  $(1 - \gamma^5)$  in the first line ensures that only the left-hand

component of the neutrino fields interact. Here we see a crucial difference that we expected: comparing the eigenvectors between the vacuum Hamiltonian defined in Eq. 2.14 and  $H_{CC}$  shows us that by this construction, CC interactions occur in the flavor basis.

The effective potential that the electron neutrino experiences is then

$$V_{CC} = \sqrt{2}G_F N_e. \quad (2.39)$$

For neutral current, we replace the electron field  $e(x)$  in Eq. 2.31 by the more general fermion field  $f(x)$ , and the chiral projection operator  $(1 - \gamma^5)$  with  $(g_V^f - g_A^f \gamma^5)$ . Again, the  $\gamma^5$  will cause the spacial component of  $p_f$  to disappear after integration, and the only difference between the average effective Hamiltonian for the neutral current is then the factor  $g_V^f$ :

$$V_{NC}^f = \sqrt{2}G_F N_A g_V^f. \quad (2.40)$$

Summing over the fermions, and assuming electrical neutrality and equal abundance of protons and neutrons, we have

$$\begin{aligned} V_{NC} &= \sum_{f \in e, p, n} V_{NC}^f \\ &= \sqrt{2}G_F N_A \sum_{f \in e, p, n} g_V^f \\ &= \sqrt{2}G_F N_A \left[ -\frac{1}{2} + 2 \sin^2(\theta_W) + \frac{1}{2} - 2 \sin^2(\theta_W) - \frac{1}{2} \right] \\ &= -\frac{1}{\sqrt{2}}G_F N_e, \end{aligned} \quad (2.41)$$

where the electrical neutrality condition allows us to simply sum the vectorial couplings together, cancelling the electron and proton contributions (and hence, also the  $\theta_W$  dependence).

We now see that both matter potentials, regardless of the interaction is of type charged or neutral, are only dependent on the electron density in the medium,  $N_e$  times a constant. So to calculate the matter oscillations in an electrically neutral medium with an equal abundance of protons and neutrons, we are only required to consider the matter density of the medium.

Since only  $\nu_e$  undergo CC interactions in Earth-like matter, the  $V_{CC}$  potential is zero for all other flavors. However, since all flavors undergo NC interactions the total matter potential in the flavor basis is

$$V = \begin{bmatrix} V_{CC} + V_{NC} & 0 & 0 \\ 0 & V_{NC} & 0 \\ 0 & 0 & V_{NC} \end{bmatrix} = V_{CC} \delta_{\alpha e} \mathbb{I} + V_{NC} \mathbb{I}. \quad (2.42)$$

Just as in Eq. 2.16, we start with a Hamiltonian that solves the time-dependent Schrödinger equation. This time, let the Hamiltonian be

$$H = H_0 + H_I , \quad (2.43)$$

where  $H_0$  is the Hamiltonian in vacuum, and  $H_I$  is our interaction Hamiltonian associated with our matter potentials. Let the amplitude for the  $\nu_\alpha \rightarrow \nu_\beta$  transition be denoted as

$$\psi_{\alpha\beta}(t) = \langle \nu_\beta | \nu_\alpha(t) \rangle , \quad (2.44)$$

i.e. the evolution of the state of a neutrino emitted at  $t = 0$  with flavor  $\alpha$  to flavor  $\beta$  at time  $t$ . Now using Eq. 2.14 and Eq. 2.39, we are ready to see what form our Hamiltonians take. Let us start with the vacuum Hamiltonian  $H_0$ , and act on its Schrödinger equation with  $\langle \nu_\beta |$ :

$$i \frac{d}{dt} |\nu_\alpha(t)\rangle = H_0 |\nu_\alpha(t)\rangle \implies i \frac{d}{dt} \psi_{\alpha\beta} = \langle \nu_\beta | H_0 | \nu_\alpha(t) \rangle . \quad (2.45)$$

Eq. 2.45 with the full Hamiltonian from Eq. 2.43 is what we will numerically solve for the three neutrino picture for neutrino oscillations in matter.

### 2.3.4 The Three Neutrino Picture

Reminding ourselves that the vacuum Hamiltonian  $H_0$  has eigenstates in the mass basis, we write the following expression where we use the relations Eq. 2.14 and Eq. 2.19 to switch between the flavor and mass basis with the PMNS elements:

$$\begin{aligned} \langle \nu_\beta | H_0 &= \sum_k U_{\beta k} \langle \nu_k | H_0 \\ &= \sum_k U_{\beta k} E_k \langle \nu_k | \\ &= \sum_\eta \sum_k U_{\beta k} E_k U_{\eta k}^* \langle \nu_\eta | . \end{aligned} \quad (2.46)$$

Thus,

$$\begin{aligned} \langle \nu_\beta | H_0 | \nu_\alpha(t) \rangle &= \sum_\eta \sum_k U_{\beta k} E_k U_{\eta k}^* \langle \nu_\eta | \nu_\alpha(t) \rangle \\ &= \sum_\eta \sum_k U_{\beta k} E_k U_{\eta k}^* \psi_{\alpha\eta}(t) . \end{aligned} \quad (2.47)$$

Using the ultrarelativistic approximation from Eq. 2.22:

$$\begin{aligned} \sum_{\eta} \sum_k U_{\beta k} E_k U_{\eta k}^* \psi_{\alpha \eta}(t) &= \sum_{\eta} \sum_k U_{\beta k} \left( p + \frac{m_k^2}{2E} \right) U_{\eta k}^* \psi_{\alpha \eta}(x) \\ &= \sum_{\eta} \sum_k U_{\beta k} \left( p + \frac{m_k^2}{2E} \right) U_{\eta k}^* \psi_{\alpha \eta}(x). \end{aligned} \quad (2.48)$$

Use the fact that  $\sum_k m_k^2 = \sum m_1^2 + {}_k m_k^2 - m_1^2 = \sum_k m_1^2 + \Delta m_{k1}^2$  to pull out common terms out of the summation:

$$\begin{aligned} \sum_{\eta} \sum_k U_{\beta k} \left( p + \frac{m_k^2}{2E} \right) U_{\eta k}^* \psi_{\alpha \eta}(x) &= \sum_{\eta} \sum_k U_{\beta k} \left( p + \frac{m_1^2}{2E} + \frac{\Delta m_{k1}^2}{2E} \right) U_{\eta k}^* \psi_{\alpha \eta}(x) \\ &= \sum_{\eta} \sum_k \left( p + \frac{m_1^2}{2E} \right) U_{\beta k} U_{\eta k}^* \psi_{\alpha \eta}(x) \\ &\quad + \sum_{\eta} \sum_k U_{\beta k} \frac{\Delta m_{k1}^2}{2E} U_{\eta k}^* \psi_{\alpha \eta}(x). \end{aligned} \quad (2.49)$$

Unitarity gives  $\sum_k U_{\beta k} U_{\eta k}^* = \delta_{\eta \beta}$ , and the first term in the last step of Eq. 2.49 becomes

$$\sum_{\eta} \left( p + \frac{m_1^2}{2E} \right) \delta_{\beta \eta} \psi_{\alpha \eta}(x) = \left( p + \frac{m_1^2}{2E} \right) \psi_{\alpha \beta}(x). \quad (2.50)$$

Our treatment of the interaction Hamiltonian is similar except for the fact that its eigenstates lie in the flavor basis, conveniently allowing us to letting it act directly on the flavor eigenstates:

$$\begin{aligned} \langle \nu_{\beta} | H_I &= V_{\beta} \langle \nu_{\beta} | \\ &= \delta_{\beta \eta} V_{\beta} \langle \nu_{\eta} |. \end{aligned} \quad (2.51)$$

Using Eq. 2.42 in component form, we rewrite this as

$$\begin{aligned} \delta_{\beta \eta} V_{\beta} \langle \nu_{\eta} | &= \delta_{\beta \eta} (V_{CC} \delta_{\beta e} + V_{NC}) \langle \nu_{\eta} | \\ &= V_{CC} \delta_{\beta \eta} \delta_{\beta e} \langle \nu_{\eta} | + V_{NC} \langle \nu_{\beta} | \\ \implies \langle \nu_{\beta} | H_I | \nu_{\alpha} \rangle &= V_{CC} \delta_{\beta \eta} \delta_{\beta e} \langle \nu_{\eta} | \nu_{\alpha} \rangle + V_{NC} \langle \nu_{\beta} | \nu_{\alpha} \rangle \\ &= V_{CC} \delta_{\beta \eta} \delta_{\beta e} \psi_{\alpha \eta} + V_{NC} \psi_{\alpha \beta} \end{aligned} \quad (2.52)$$

Now, combining Eq. 2.49 and Eq. 2.52, we have for the full Hamiltonian

$$\begin{aligned} \langle \nu_{\beta} | H | \nu_{\alpha}(x) \rangle &= \left( p + \frac{m_1^2}{2E} + V_{NC} \right) \psi_{\alpha \beta}(x) \\ &\quad + \sum_{\eta} \sum_k \left( U_{\beta k} \frac{\Delta m_{k1}^2}{2E} U_{\eta k}^* + V_{CC} \delta_{\beta \eta} \delta_{\eta e} \right) \psi_{\alpha \eta}(x) \end{aligned} \quad (2.53)$$

In this form, we see that the term  $p + \frac{m_1^2}{2E} + V_{NC}$  is a common term to all flavor states and does not affect the probability. It can be rotated away. Thus

$$\begin{aligned}\langle \nu_\beta | H | \nu_\alpha(x) \rangle &= \sum_\eta \sum_k \left( U_{\beta k} \frac{\Delta m_{k1}^2}{2E} U_{\eta k}^* + V_{CC} \delta_{\beta\eta} \delta_{\eta e} \right) \psi_{\alpha\eta}(x) \\ &= i \frac{d}{dx} \psi_{\alpha\beta}(x).\end{aligned}\quad (2.54)$$

If we form the vector

$$\Psi_\alpha = \begin{pmatrix} \psi_{\alpha e} \\ \psi_{\alpha\mu} \\ \psi_{\alpha\tau} \end{pmatrix}, \quad (2.55)$$

we can write the Schrödinger equation on matrix form ( $i \frac{d}{dx} \Psi_\alpha = H_F \Psi_\alpha$ ) and compare it with Eq. 2.54 to see that the flavor Hamiltonian takes the form

$$\begin{aligned}H_F &= \frac{1}{2E} (U M^2 U^\dagger + A) \\ &= \frac{1}{2E} \left[ U \begin{pmatrix} 0 & 0 & 0 \\ 0 & \Delta m_{21}^2 & 0 \\ 0 & 0 & \Delta m_{31}^2 \end{pmatrix} U^\dagger \right] + \sqrt{2} G_F N_e \begin{pmatrix} 1 & 0 & 0 \\ 0 & 0 & 0 \\ 0 & 0 & 0 \end{pmatrix}.\end{aligned}\quad (2.56)$$

This is the three-flavor neutrino oscillation Hamiltonian that we will solve numerically to obtain the evolution of  $\Psi_\alpha$ , whose squared components are the probabilities

$$\begin{aligned}P_\alpha &= |\Psi_\alpha|^2 = \begin{pmatrix} |\psi_{\alpha e}|^2 \\ |\psi_{\alpha\mu}|^2 \\ |\psi_{\alpha\tau}|^2 \end{pmatrix} \\ &= \begin{pmatrix} P_{\alpha e} \\ P_{\alpha\mu} \\ P_{\alpha\tau} \end{pmatrix}\end{aligned}\quad (2.57)$$

For  $N_e = 0$ , i.e. in vacuum, these probabilities are identical to the ones that we analytically derived in Eq. 2.26. For matter oscillations with  $N_e \neq 0$ , we do have closed-form solutions, but they are not considered further here.

### 2.3.5 Earth Propagation

We now need to know how the electrons are distributed within the Earth. The Preliminary Earth Reference Model [6] gives us spherically symmetric piecewise polynomials for the Earth density in  $\text{g cm}^{-3}$  shown in the left panel of Fig. 2.3. We note a steep discontinuity at 3480 km where the density is nearly halved. This is the core-mantle boundary and will be visible in our oscillations.

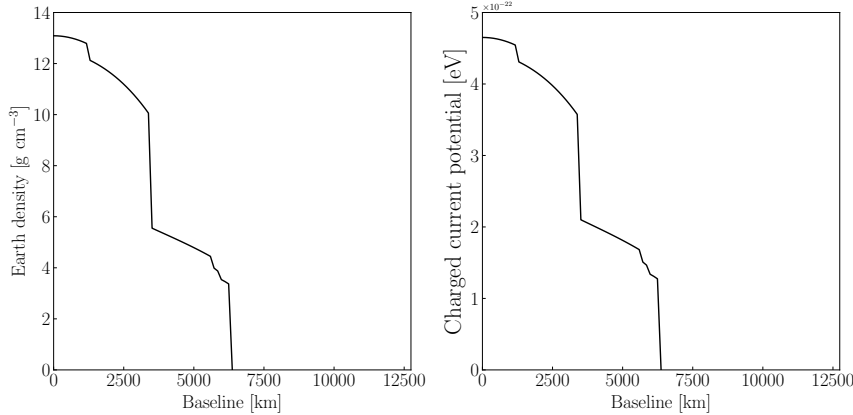


Figure 2.3: *Left panel:* The spherically symmetric Earth density according to PREM [6], as of distance from the core. *Right panel:*  $V_{CC}$  using the PREM density and 1/2 electrons per nucleon.

Using a value of  $Y = 0.5$  electron per nucleon, we express the matter potential as

$$\begin{aligned} V_{CC} &= \sqrt{2}G_F N_e = \sqrt{2}G_F Y N_A \rho \\ &= 3.8 \times 10^{-23} \text{ eV} \times \rho, \end{aligned} \quad (2.58)$$

a low number due to the smallness of  $G_F$ . This is plotted in the right panel of Fig. 2.3

Now, solving the Schrödinger equation with the Hamiltonian from Eq. 2.56 with the matter potential from the PREM, we obtain the nine combinations of probabilities through the Earth diameter. We note that due to our assumption of CP-invariance (and thus, T-invariance), the probabilities  $P_{\alpha\beta}$  and  $P_{\beta\alpha}$  are equivalent. The result for GeV neutrinos is shown in Fig. 2.4.

Now we need to incorporate the *zenith angle*, here defined as the angle between the neutrino direction of travel and south. This way, neutrinos traveling through the entire diameter of the Earth are defined as ‘up-going’, while neutrinos that directly over-head are ‘down-going’. We will mostly work with the quantity  $\cos(\theta_z)$ . Since we are interested in the matter effects, some studies are only looking at up-going neutrinos, i.e. neutrinos with zenith angle  $-1 \leq \cos(\theta_z) \leq 0$ . However, while down-going neutrinos don’t experience matter oscillations (and hardly even vacuum oscillations due to the short baseline), they can be included to reduce systematic errors. We now supplement our probability grid from Fig. 2.4 with the zenith dimension, allowing us to fully see the Earth matter effect on the oscillations in full. This is shown in Fig. 2.5.

In Fig. 2.6, we have plotted the oscillation probabilities for an incoming  $\nu_\mu$  with GeV energy, traveling 12742 km. The red line is the vacuum oscillation, while the

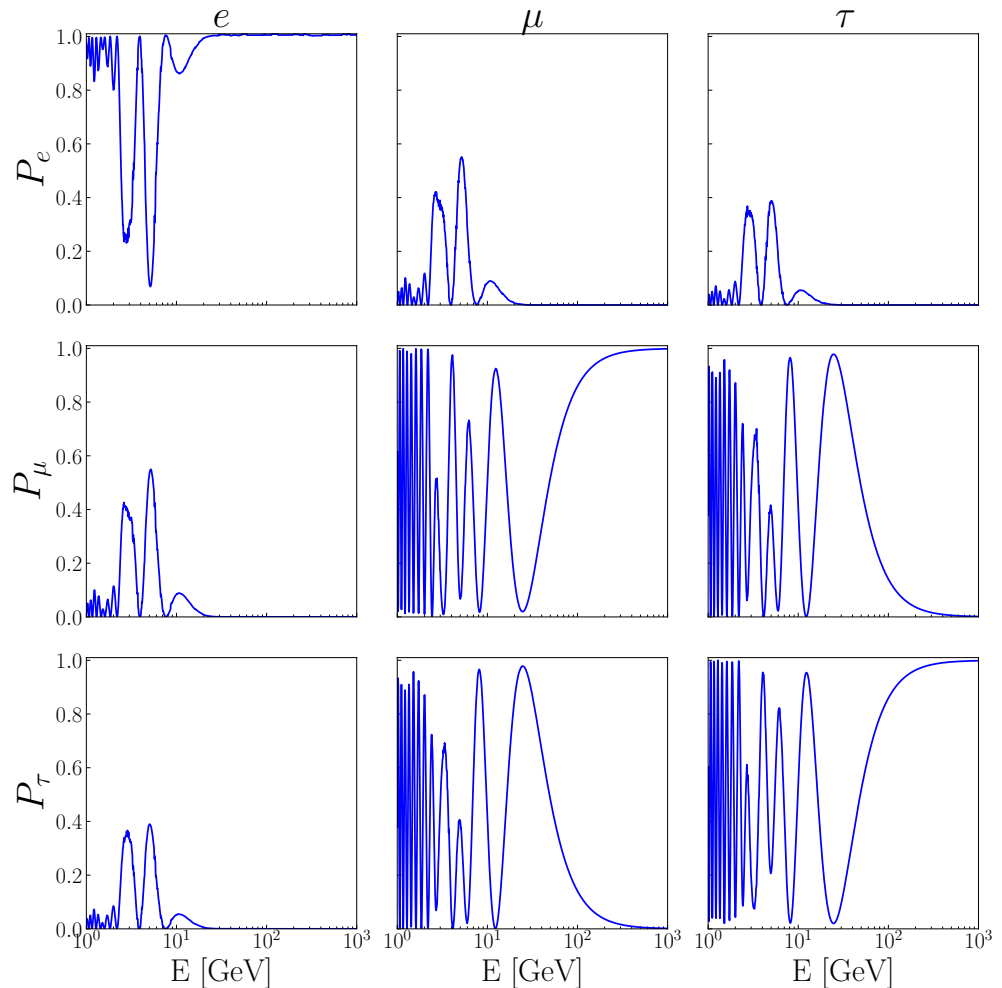


Figure 2.4: Neutrino oscillation probabilities after traversing the diameter of the Earth. Oscillation parameters are taken from NuFit [5] and given in Eq. 3.13.

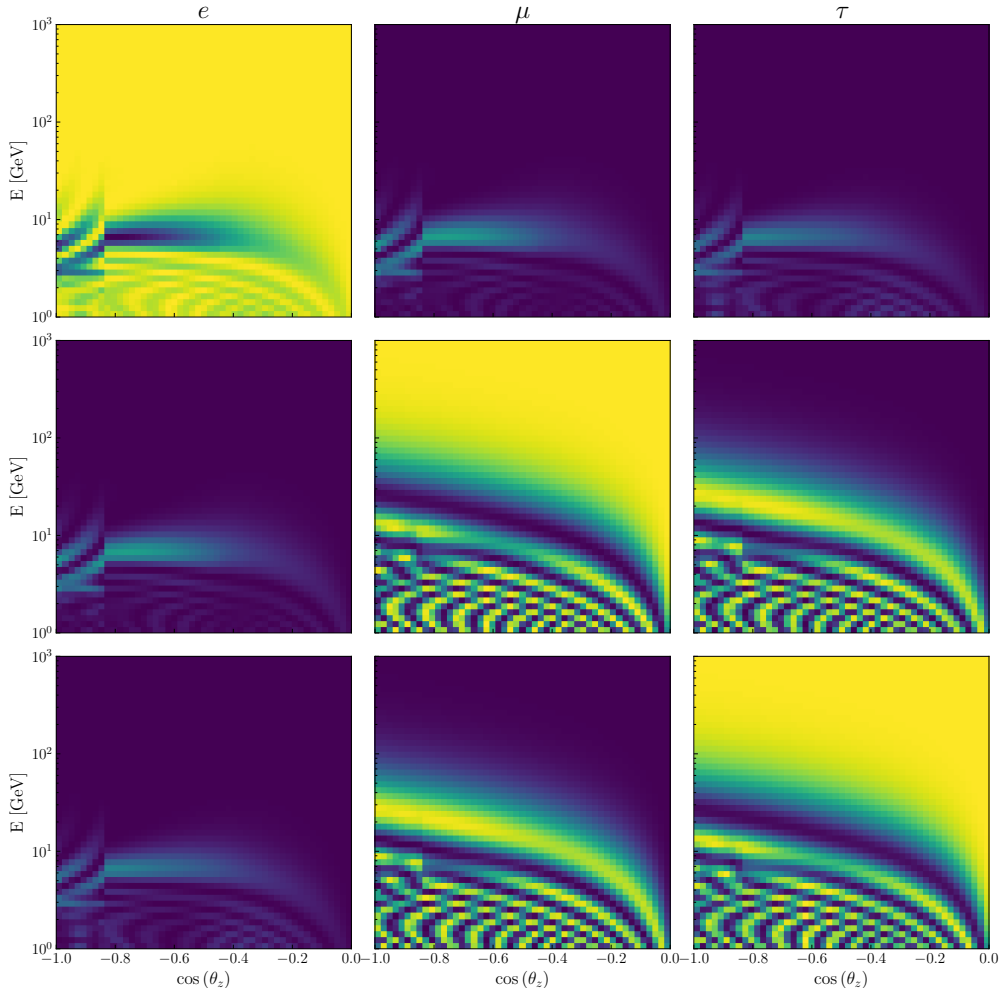


Figure 2.5: Oscillograms showing neutrino oscillations for all flavors in  $E - \cos(\theta_z)$  space using parameters from [5]. Note the panels are symmetric about the diagonal panels, i.e.  $P_{\alpha\beta} = P_{\beta\alpha}$  due to  $\delta_{CP} = 0^\circ$ . The core-mantle boundary from Fig. 2.3 is clearly displayed at  $\cos(\theta_z) = -0.83$  as a sharp discontinuity for all flavors.

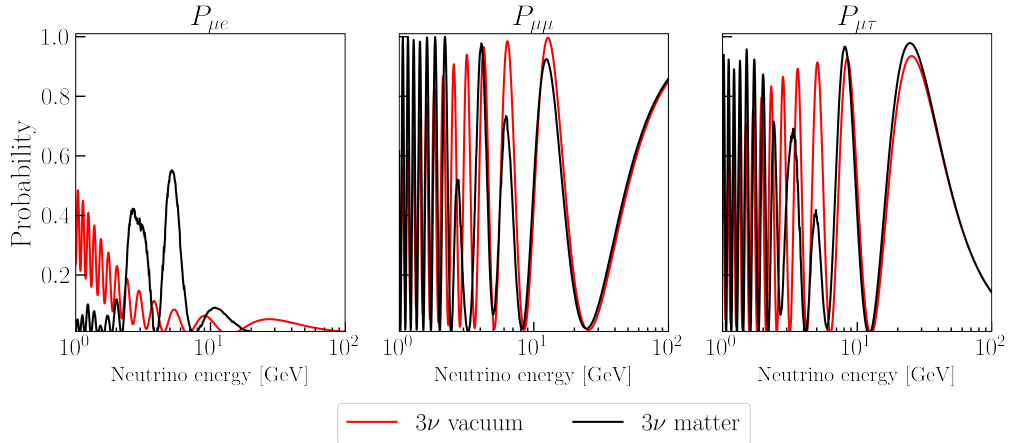


Figure 2.6:  $\nu_\mu$  oscillation probabilities after traversing the diameter of the Earth in black, compared to the vacuum oscillation with the same baseline in red. Oscillation parameters are taken from NuFit [5] and given in Eq. 3.13.

black line is the matter oscillation, traversing through the matter density profile of the Earth. We see that the matter effects are more for some energies, and less for others. At energies above 10 GeV, the matter effects are small for  $P_{\mu\mu}$  and  $P_{\mu\tau}$ , while they heavily deviate for single-digit GeV energies.  $P_{\mu e}$  behaves in a different way, where the matter effects affect the oscillation probability regardless of energy. Here, we start to see the convergence as late as 100 GeV. Thus, matter effects are most important for energies below 100 GeV, for all channels. Above these energies, the density profile of the Earth is less relevant, and the Earth is more or less transparent for  $\nu_\mu$ .

### 2.3.6 The Two Neutrino Picture

By working in the limit where one of the neutrino masses can be neglected, we can reduce the complexity of the neutrino oscillations and obtain tractable analytical expressions. We now only consider the mixing between two neutrino flavors, say between  $\nu_e, \nu_\mu$ , and  $\nu_1, \nu_2$ . In other words, we let  $\Delta m_{31}^2 = 0$ . For simplicity, let  $\delta_{CP} = 0$ .

The three-neutrino oscillation Hamiltonian from Eq. (2.56) now reduces to

$$\begin{aligned} H_F &= \frac{1}{2E}(U M^2 U^\dagger + A) \\ &= \frac{1}{2E} \left[ U \begin{pmatrix} 0 & 0 & 0 \\ 0 & \Delta m_{21}^2 & 0 \\ 0 & 0 & 0 \end{pmatrix} U^\dagger \right] + \sqrt{2} G_F N_e \begin{pmatrix} 1 & 0 & 0 \\ 0 & 0 & 0 \\ 0 & 0 & 0 \end{pmatrix}. \end{aligned} \quad (2.59)$$

We can reduce this down to two dimensions by extracting the upper-left block of

all matrices<sup>2</sup>. We now have the Hamiltonian in a two-dimensional form, and start simplifying:

$$\begin{aligned}
H_F &= \frac{1}{2E} \left[ \begin{pmatrix} c_{12} & s_{12} \\ -s_{12} & c_{12} \end{pmatrix} \begin{pmatrix} 0 & 0 \\ 0 & \Delta m_{21}^2 \end{pmatrix} \begin{pmatrix} c_{12} & s_{12} \\ -s_{12} & c_{12} \end{pmatrix}^\dagger \right] + \sqrt{2}G_F N_e \begin{pmatrix} 1 & 0 \\ 0 & 0 \end{pmatrix} \\
&= \frac{1}{2E} \left[ \begin{pmatrix} 0 & \Delta m_{21}^2 s_{12} \\ 0 & \Delta m_{21}^2 c_{12} \end{pmatrix} \begin{pmatrix} c_{12} & -s_{12} \\ s_{12} & c_{12} \end{pmatrix} \right] + \sqrt{2}G_F N_e \begin{pmatrix} 1 & 0 \\ 0 & 0 \end{pmatrix} \\
&= \frac{1}{2E} \begin{pmatrix} \Delta m_{21}^2 s_{12}^2 & \Delta m_{21}^2 s_{12} c_{12} \\ \Delta m_{21}^2 s_{12} c_{12} & \Delta m_{21}^2 c_{12}^2 \end{pmatrix} + \sqrt{2}G_F N_e \begin{pmatrix} 1 & 0 \\ 0 & 0 \end{pmatrix} \\
&= \frac{1}{4E} \begin{pmatrix} \Delta m_{21}^2 (1 - \cos(2\theta_{12})) & \Delta m_{21}^2 \sin(2\theta_{12}) \\ \Delta m_{21}^2 \sin(2\theta_{12}) & \Delta m_{21}^2 (1 + \cos(2\theta_{12})) \end{pmatrix} + \sqrt{2}G_F N_e \begin{pmatrix} 1 & 0 \\ 0 & 0 \end{pmatrix}
\end{aligned} \tag{2.60}$$

Just as we did with Eq. 2.54, we can subtract a term proportional to the identity matrix without affecting the underlying physics. Thus, we subtract

$$\frac{\Delta m_{21}^2}{4E} - \frac{1}{2}\sqrt{2}G_F N_e \tag{2.61}$$

times the identity from the Hamiltonian, obtaining the final two-neutrino Hamiltonian

$$\begin{aligned}
H_F &= \frac{1}{4E} \begin{pmatrix} -\Delta m_{21}^2 \cos(2\theta_{12}) & \Delta m_{21}^2 \sin(2\theta_{12}) \\ \Delta m_{21}^2 \sin(2\theta_{12}) & \Delta m_{21}^2 \cos(2\theta_{12}) \end{pmatrix} + \frac{1}{2}\sqrt{2}G_F N_e \begin{pmatrix} 1 & 0 \\ 0 & -1 \end{pmatrix} \\
&= \frac{1}{4E} \begin{pmatrix} -\Delta m_{21}^2 \cos(2\theta_{12}) + \sqrt{2}G_F N_e & \Delta m_{21}^2 \sin(2\theta_{12}) \\ \Delta m_{21}^2 \sin(2\theta_{12}) & \Delta m_{21}^2 \cos(2\theta_{12}) - \sqrt{2}G_F N_e \end{pmatrix}
\end{aligned} \tag{2.62}$$

This matrix has eigenvalues which we identify as the effective two-neutrino squared-mass difference  $(\Delta m_{21}^2)^M$ . They are

$$\pm(\Delta m_{21}^2)^M = \pm\sqrt{(\Delta m_{21}^2 \cos(2\theta_{12}) - 2\sqrt{2}G_F N_e E)^2 + (\Delta m_{21}^2 \sin(2\theta_{12}))^2} \tag{2.63}$$

The matrix is diagonalized by the usual rotation matrix  $R_{12}$ , but with a different rotation angle. This now introduces the effective two-neutrino mixing angle  $\theta_{12}^M$ :

$$U^M = R_{12}^M = R_{12}(\theta_{12}^M). \tag{2.64}$$

$U^M$  diagonalizes  $H_F$  if and only if

---

<sup>2</sup>Or, following the method of the derivation of the Hamiltonian in the three- neutrino picture, take  $U$  as one two-dimensional rotation matrix.

$$\tan(2\theta_{12}^M) = \frac{\tan(2\theta_{12})}{1 - \frac{2\sqrt{2}G_F N_e E}{\Delta m_{21}^2 \cos(2\theta_{12})}}. \quad (2.65)$$

Eq. 2.65 has a pole at

$$E^* = \frac{\Delta m_{21}^2 \cos(2\theta_{12})}{2\sqrt{2}G_F N_e}. \quad (2.66)$$

So at a certain electron density, a neutrino with energy  $E^*$  will experience a resonance in the matter mixing angle. This phenomenon is called MSW resonance after Mikheev, Smirnov, and Wolfenstein. At this point,  $\tan(2\theta_{12}^M) \rightarrow \infty$ , which is equivalent to the matter mixing angle  $\theta_{12}^M$  assuming its maximal value,  $\pi/4$ . Thus, the MSW resonance can cause maximal mixing between two flavors.

Now assume that the matter density is sufficiently constant along a trajectory  $x$ , that is  $d\theta_M/dx \approx 0$ . In its diagonalized form, the Schrödinger equation with two-neutrino Hamiltonian can be solved with this assumption. The solutions are the regular neutrino vacuum oscillations of Eq. 2.26 using  $\theta_{13} = \theta_{23} = 0$ , but with the effective parameters of Eqs. (2.63, 2.65). That is

$$P_{e\mu}^M = \sin^2(2\theta_{12}^M) \sin^2\left(\frac{\Delta m_{21}^2 L}{4E}\right). \quad (2.67)$$

While two-neutrino flavor oscillation can only be assumed to hold in regions where mixing into the third flavor can be considered negligible, the fact that the mixing angle in matter depends on the squared-mass difference, and vice versa, gives us an interesting conclusion which is still valid for the full three neutrino oscillations. We previously saw that the oscillation amplitudes were entirely dependant on the mixing angles, and the oscillation frequencies were entirely dependant on the squared-mass difference along with energy and trajectory. After introducing the matter potentials, we now see that the matter effect mixes the mixing matrix elements with the masses and the energy.

In Fig. 2.7, we have plotted the oscillation probabilities for an incoming  $\nu_\mu$  with GeV energy, traveling through the entire Earth diameter. The black lines are the probabilities of  $\nu_\mu$  oscillation, after it has traversing through the diameter of the Earth. The red lines are the probabilities of  $\nu_\mu$  oscillation, but in the two-neutrino picture using Eq. 2.67. So in the left-most panel, we are only considering the mixing between  $\nu_e$  and  $\nu_\mu$ , completely neglecting  $\theta_{13}$  and  $\theta_{23}$ .

The pattern is similar to when we compared  $3\nu$  matter and vacuum oscillations: at 10 GeV, the two pictures converge. It is evident that the full  $3\nu$  picture is required for single-digit GeV energies and that mixings between all three flavors here are abundant. Increasing with energy, however, the influence of the  $\nu_1$  mass eigenstate

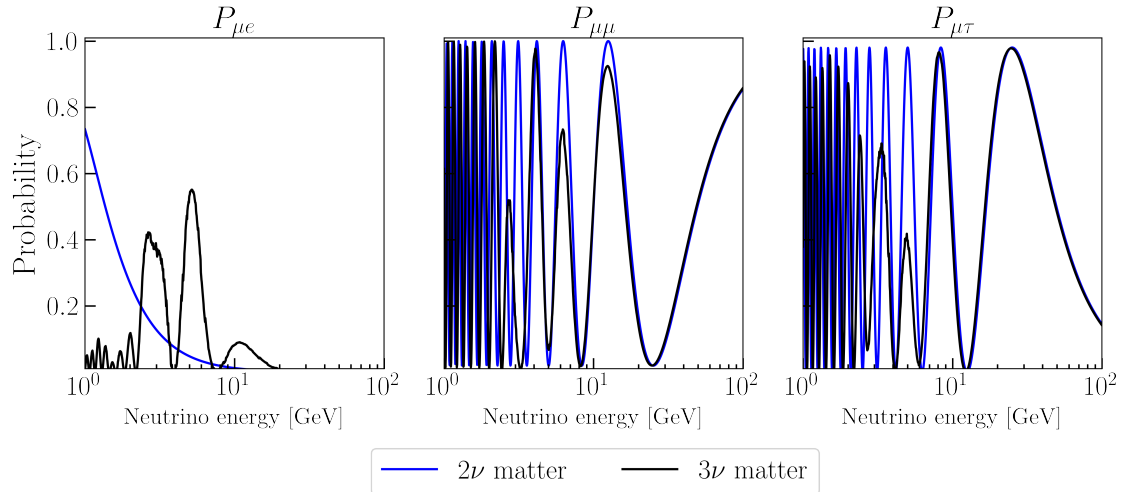


Figure 2.7:  $\nu_\mu$  oscillation probabilities after traversing the diameter of the Earth in black, compared to the two-neutrino picture oscillations with the same baseline and matter potential in blue. The figure showcases the convergence of the  $2\nu$  and  $3\nu$  pictures at energies above 10 GeV. Oscillation parameters are taken from NuFit [5] and given in Eq. 3.13.

on the probabilities is reduced. Thus, we are able to approximate resonant behavior as described in Eq. 2.66 above 100 GeV by only considering mixing between two neutrino species. We will utilize this observation later on, to study a particular resonance in the TeV range.

## Chapter 3

# The Antarctic Detectors

### 3.1 Atmospheric Neutrino Flux

Atmospheric neutrinos originate from cosmic rays composed of high-energy protons interacting with nuclei in the atmosphere. These interactions ultimately produces pions, which decay as

$$\begin{aligned}\pi^+ &\rightarrow \mu^+ + \nu_\mu, & \pi^- &\rightarrow \mu^- + \bar{\nu}_\mu \\ \pi^+ &\rightarrow e^+ + \nu_e, & \pi^- &\rightarrow e^- + \bar{\nu}_e.\end{aligned}\quad (3.1)$$

The heavy muon ( $m_\mu \approx 200m_e$ ) decays further:

$$\mu^+ \rightarrow e^+ + \nu_e + \bar{\nu}_\mu, \quad \mu^- \rightarrow e^- + \bar{\nu}_e + \nu_\mu, \quad (3.2)$$

producing even more neutrinos.

The flux is provided in [7, 8], and a selection is shown in Table 3.1. The flux data is binned in  $\cos(\theta_z)$ . The fluxes are averaged over the azimuthal direction and solar minimum/maximum. The units of the fluxes are given as  $\text{GeV}^{-1} \text{m}^{-2} \text{s}^{-1} \text{sr}^{-1}$  and are omitted from the table for clarity. We note that the fluxes for  $\nu_\tau$  and  $\bar{\nu}_\tau$  are missing. Kaons do not decay into  $\nu_\tau$ . Thus, we never have to use probabilities in the form  $P_{\tau\beta}$ , since we have no starting atmospheric  $\nu_\tau$  flux. Interpolating the data yields makes us capable of approximating all four necessary fluxes for a given true energy and true zenith. The result of  $\phi_\mu$  is shown in Fig. 3.1. We see that the flux is almost entirely zenith independent. The energy dependence of the flux is approximately  $E^{-2.7}$ , so our expected event count at higher energies will suffer from this substantial decline in flux.

$E$ [GeV]	$\phi_\mu$	$\phi_{\bar{\mu}}$	$\phi_e$	$\phi_{\bar{e}}$	$\cos(\theta_z)$
27825	$6.06 \times 10^{-12}$	$3.17 \times 10^{-12}$	$1.56 \times 10^{-13}$	$1.04 \times 10^{-13}$	[-0.2, -0.1]
247707	$5.94 \times 10^{-16}$	$2.92 \times 10^{-16}$	$1.36 \times 10^{-17}$	$8.12 \times 10^{-18}$	[-0.7, -0.6]
22	$3.33 \times 10^{-2}$	$2.78 \times 10^{-2}$	$9.57 \times 10^{-3}$	$7.15 \times 10^{-3}$	[-0.3, -0.2]
432876	$5.19 \times 10^{-17}$	$2.32 \times 10^{-17}$	$1.46 \times 10^{-18}$	$9.83 \times 10^{-19}$	[-1.1, -1.0]
64280	$1.58 \times 10^{-13}$	$8.10 \times 10^{-14}$	$3.49 \times 10^{-15}$	$2.21 \times 10^{-15}$	[-0.4, -0.3]

Table 3.1: A selection of processed atmospheric South Pole fluxes from [7] by Honda et al. [8].

We propagate the atmospheric neutrino flux  $\phi_\alpha^{\text{atm}}(E, \theta_z)$  through the Earth. The oscillation probability  $P_{\alpha\beta}$  acts as a weight to the atmospheric flux, yielding the propagated flux for flavor  $\beta$  at detector level as

$$\phi_\beta^{\text{det}} = \sum_\alpha P_{\alpha\beta} \phi_\alpha^{\text{atm}}, \quad (3.3)$$

where we sum over the initial lepton flavors  $\alpha \in \{e, \mu, \bar{e}, \bar{\mu}\}$ .

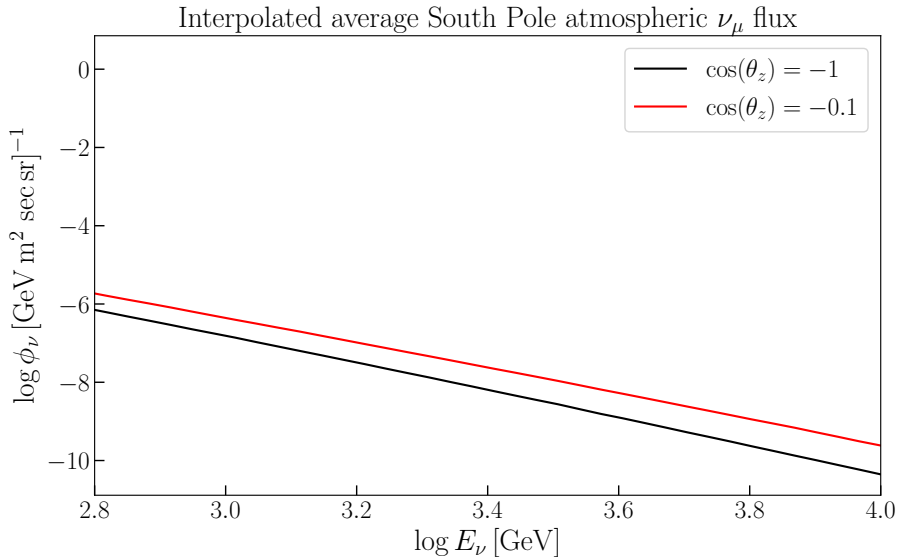


Figure 3.1: Interpolated South Pole atmospheric  $\nu_\mu$  flux with data from [8], displaying a weak zenith angle dependence, but a strong energy dependence. The energy dependence can be parametrized to be approximated by  $E^{-2.7}$ .

## 3.2 Neutrino Detection

We always observe neutrinos indirectly. Regardless of the type of interaction (charged current via the  $W$  boson, or neutral current via the  $Z$ ), a quark or charged lepton exits with altered properties. In the case of CC interactions, the fermion gets its flavor and energy changed, as seen in Eq. 3.4 where an incoming neutrino of flavor  $\alpha$  scatters of a fermion or hadron  $N$ , producing a charged lepton  $\alpha$ , and  $N'$  with charge changed by one unit.

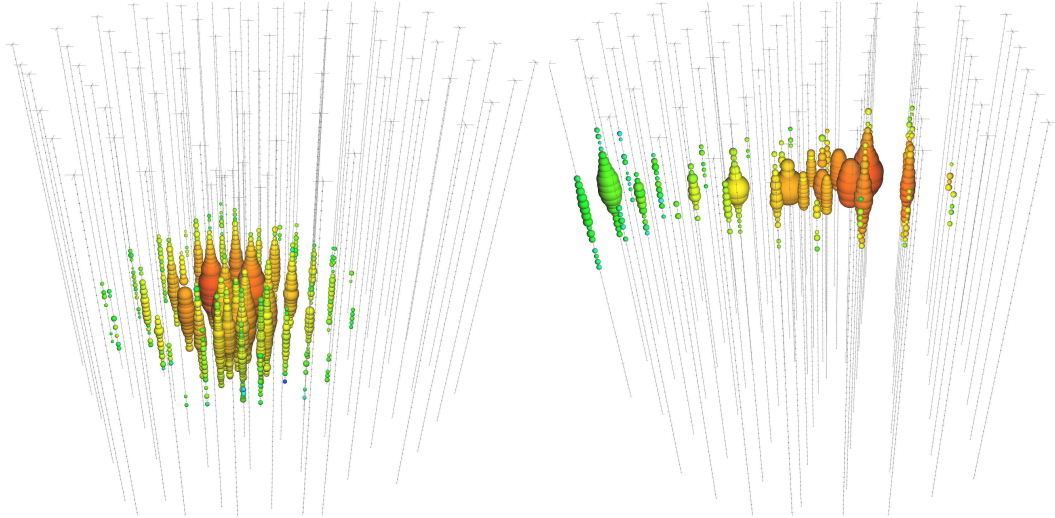
$$\nu_\alpha + N \rightarrow \alpha + N' \quad (3.4)$$

This fermion is directly involved in the interaction with the neutrino, either as both incoming and outgoing particles, or as only the outgoing particle in the case of a hadronic interaction.

In NC interactions, shown in Eq. 3.5, no flavor change can occur, so the fermion leaves with increased energy. The flavor and charge of the fermion or hadron  $N$  interacting with the neutrino are unchanged. However, energy from the neutrino will be transferred to the fermion that violently recoils, later producing a shower of tertiary particles.

$$\nu_\alpha + N \rightarrow \nu_\alpha + N' \quad (3.5)$$

In this work, we only study the detectors buried within the Antarctic ice by the IceCube collaboration. They are of Cherenkov type, which means that they detect



(a) Event classified as cascade, caused by an interaction in Eq. 3.6. (b) Event classified as track, caused by the interaction in Eq. 3.7.

Figure 3.2: The two event types distinguished in the IceCube detector.

a fermion by its emitted Cherenkov light, produced from its travel through the ice. If the secondary particles interact heavily with the ice, they will only travel a short distance. They then decay into a shower which emits a localized flash of Cherenkov light. This event is referred to as a cascade. NC interactions tend to be classified as cascades due to the production of a localized hadronic shower. However, CC  $\nu_e$  interactions can also produce a similar localized flash of Cherenkov light, causing them to also contribute to the cascade events. So what about CC  $\nu_\tau$ ? Due to the heaviness of the  $\tau$ , it rapidly decays - primarily into hadrons - giving us a short path of travel with a final shower, thus manifesting themselves as a cascade [9]. A cascade event is shown in Fig. 3.2a and Eq. 3.6, shows the possible interactions causing a cascade event. Here  $N$  denotes an incoming nucleon (consisting of one fermion due to interact with the neutrino), and the resultant  $N'$  can be a hadron or a hadronic shower.

$$\begin{aligned} \nu_\alpha + N &\rightarrow \nu_\alpha + N' \\ \nu_e + N &\rightarrow e + N' \\ \nu_\tau + N &\rightarrow \tau + N'. \end{aligned} \tag{3.6}$$

If the charged leptons do not interact as much in the ice, they penetrate a larger part of it, emitting light and tertiary particles as they go. This event is called a track and is often due to charged current muon interactions. A track event is shown in Fig. 3.2b, and Eq. 3.7 shows the possible interactions causing a track event.

$$\nu_\mu + N \rightarrow \mu + N' \tag{3.7}$$

So NC interactions and CC  $\nu_e, \nu_\tau$  interactions produce cascades, while CC  $\nu_\mu$  interactions produce tracks. The charged secondary  $N'$  is then detected (or, in the case of CC  $\nu_\tau$ , a tertiary shower from the  $\tau$  decay), and the properties of the neutrino involved in the interaction are then deduced. This deduction will be imperfect, and this introduces complexities that we will handle in Ch. 3.3. However, the detection of the topologies themselves is also not straightforward, and misclassifications are bound to occur. We see this from classifications from ‘Sample B’ of a 2019 DeepCore study [9], from which we summarize the classification information in Table 3.2.

Interaction	Track	Cascade
CC $\nu_e$	30%	70%
CC $\nu_\mu$	70%	30%
CC $\nu_\tau$	29%	71%
NC $\nu$	24%	76%

Table 3.2: The neutrino event classification at 56 GeV from ‘Sample B’ in [9], showing how simulated events were classified.

In order to detect the Cherenkov light, 60 Digital Optical Modules (DOMs) are placed on a long string up to 17 m apart. 86 of these strings are then lowered into 2.5 km deep boreholes in the ice. The holes are then sealed by refreezing the ice, resulting in a total of 5160 DOMs in a volume of approximately 1 km<sup>3</sup> [10].

The strings and DOMs are not spaced evenly, making some parts of the detector more sensitive to certain energy ranges than others. 8 strings packed more tightly than the other 78, making that part of the detector sensitive to neutrino energies down to single-digit GeV. This detector is referred to DeepCore. DeepCore will be treated as a separate and independent detector from the rest of the array, which retains the name IceCube. A view of the current setup can be seen in Fig. 3.3. In this work, we consider DeepCore data between 5.6 GeV to 56 GeV and IceCube data in the range 0.5 TeV to 10 TeV.

In 2017, the PINGU Letter of Intent was published [11]. The ‘Precision Ice-Cube Next Generation Upgrade’ is an upgrade that will supplement DeepCore, i.e. boosting the capabilities of neutrino detection at the GeV scale. As the PINGU upgrade is not yet financed nor built, we are unable to use any data from it. However, the collaboration has released preliminary simulations, which we will use. The simulated events are between 5.6 GeV to 56 GeV, the same range as the DeepCore data. The PINGU simulations have the same structure as the DeepCore data, so our analysis referring to DeepCore will also apply to PINGU except where noted. However, we treat the PINGU detector as independent of the other experiments.

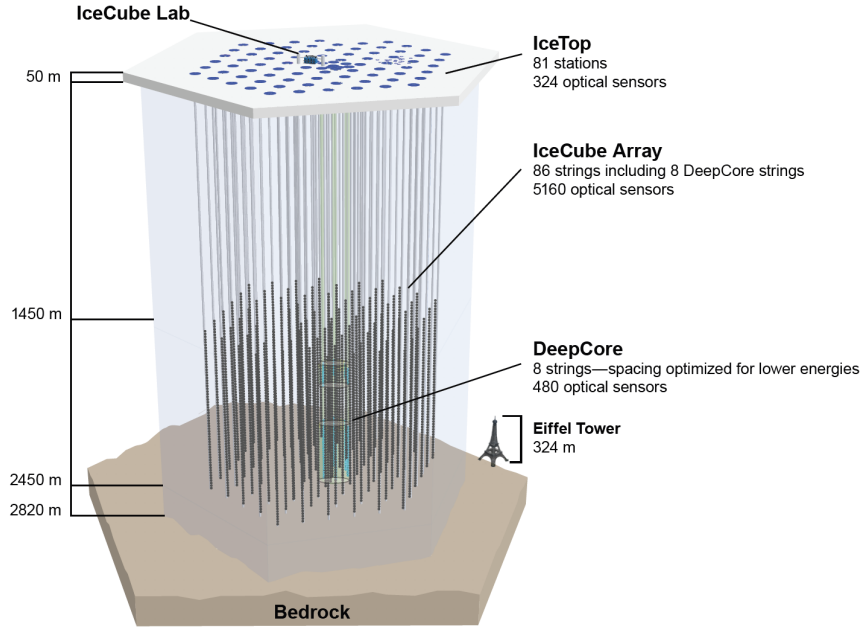


Figure 3.3: View of the full IceCube array, with the Eiffel tower for scale.

### 3.2.1 True and Reconstructed Parameters

After an event has occurred, the IceCube collaboration *reconstruct* the event. Given the parameters recorded by the detector, what are their ‘true’ values? We are interested in two variables: energy and direction. Each event is tagged with a probable energy and zenith angle, called the reconstructed parameters  $E^{reco}$  and  $\cos(\theta_z^{reco})$ , which are the parameters according to the DOMs. In other words, the collaboration uses the recorded data to backtrack the event, using the reconstructed parameters to approximate the true parameters. So a charged lepton hits the DOMs, and we ultimately end up with the associated neutrino’s true energy and zenith angle,  $E^{true}$  and  $\cos(\theta_z^{true})$ . The reconstructed parameters are what we are using to analyze the data (because this is what the detector sees), while the true parameters are used in the determination of that neutrino’s ‘actual’ flux and cross-section (because this is what Nature sees).

How do we then translate between the reconstructed and true parameters? In this work, we are using two different methods, which are based on the form of data available to us. They will be outlined in Sec. 3.3 and Sec. 3.4.

### 3.3 IceCube

As the neutrinos have propagated the Earth, they arrive at the South Pole, where they interact with charged leptons in the ice. The charged lepton then emits the Cherenkov light detected by the array. We construct the event rate for each bin as

$$N_{ij} = T \sum_{\beta} \int_{(\cos \theta_z^r)_i}^{(\cos \theta_z^r)_{i+1}} d \cos \theta_z^r \int_{E_j^r}^{E_{j+1}^r} d E^r \int_0^{\pi} R(\theta^r, \theta^t) d \cos \theta^t \int_0^{\infty} R(E^r, E^t) \phi_{\beta}^{\text{det}} A_{\beta}^{\text{eff}} d E^t, \quad (3.8)$$

where  $T$  is the live time of the detector,  $\beta$  the final neutrino flavors,  $\theta_z^r$  the reconstructed zenith angle, i.e. the deduced direction of the incoming neutrino binned with index  $i$ .  $\theta_z^t$  is the true zenith angle, i.e. the actual direction of the incoming neutrino.  $E^r$  is the reconstructed energy, binned with index  $j$ .  $R(\theta^r, \theta^t)$  is a zenith resolution function that describes the relationship with the reconstructed and true zenith angles, specific to the 86-string configuration of IceCube.  $R(E^r, E^t)$  is an energy resolution function that describes the relationship with the reconstructed and true energies.  $\phi_{\beta}^{\text{det}}$  is the conventional atmospheric neutrino flux for flavor  $\beta$ , propagated to detector level in accordance with Eq. 3.3.

We now are interested in the effective area  $A^{\text{eff}}$ , i.e. the cross-sectional area of the detector that the lepton is exposed to.  $A^{\text{eff}}$  depends on several parameters, some of them being physical detector volume,  $E^{\text{true}}$ ,  $\cos(\theta_z^{\text{true}})$ , and the particle type. Fortunately, the binned  $A^{\text{eff}}$  is provided to us by the collaboration [12]. An excerpt from this data is shown in Table 3.3.

$E_{\text{min}}^{\text{true}}$ [GeV]	$E_{\text{max}}^{\text{true}}$ [GeV]	$\cos(\theta_z^{\text{true}})_{\text{min}}$	$\cos(\theta_z^{\text{true}})_{\text{max}}$	$A^{\text{eff}}$ [ $\text{m}^2$ ]
251	316	-0.92	-0.91	0.0174
794300	1000000	-0.80	-0.79	69.3600
3981	5012	-0.78	-0.77	3.1490
1585	1995	-0.07	-0.06	0.4659
398	501	-0.73	-0.72	0.0555

Table 3.3: IceCube-86 effective area from [12].

Here,  $A^{\text{eff}}$  has been averaged over  $A_{\mu}^{\text{eff}}$  and  $A_{\bar{\mu}}^{\text{eff}}$  by the collaboration. Thus, both  $\mu$  and  $\bar{\mu}$  will, on average, experience the same  $A^{\text{eff}}$  in our model. Just as with the fluxes, we interpolate this in  $E^{\text{true}}$  and  $\cos(\theta_z^{\text{true}})$ , and show the result in Fig. 3.4. Since the IceCube array is slightly rectangular, the zenith angle affects the cross-sectional area to which the array the leptons are exposed to. While the flux was almost flat in  $\cos(\theta_z^{\text{true}})$ , the introduction of the zenith dependent  $A^{\text{eff}}$  will make the result slightly more zenith dependent than the flux itself. Increasing linearly with energy, the effective area of the detector approaches its geometrical area of  $1 \times 10^6 \text{ m}^2$  but is still only in the single-digit range at TeV energies.

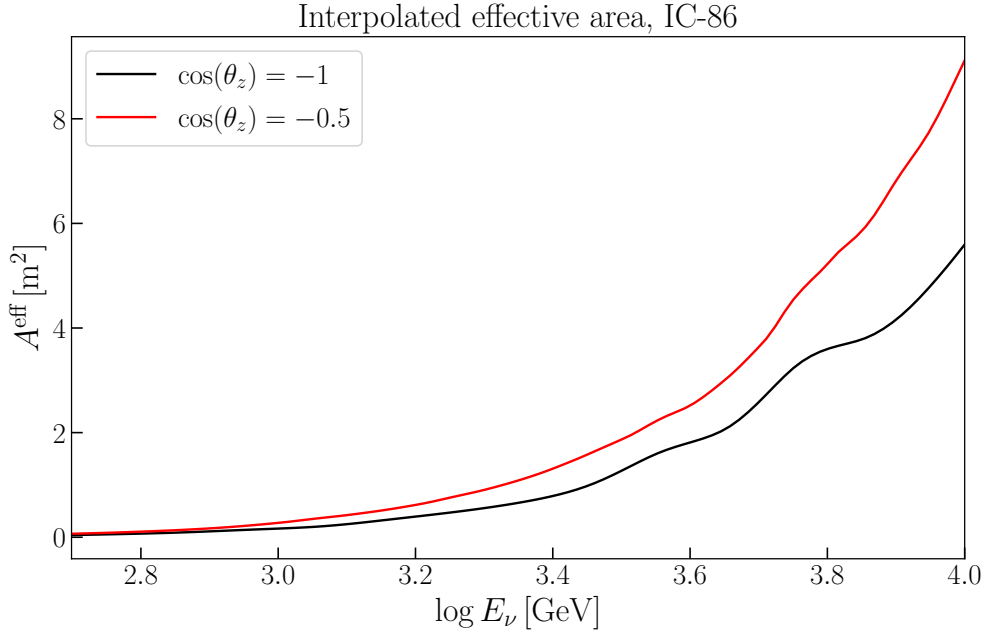


Figure 3.4: Interpolated IceCube effective area with data from [12].

So now we have the physical quantities in the true parameters. As we discussed, we need a way to translate this into the reconstructed parameters that the detector gives us. We will call the relationship between  $E^{reco}$  and  $E^{true}$  the energy resolution function, and the relationship between  $\cos(\theta_z^{reco})$  and  $\cos(\theta_z^{true})$  the zenith resolution function. We assume the relationship to follow a logarithmic Gaussian distribution, giving it the form

$$R(x^r, x^t) = \frac{1}{\sqrt{2\pi}\sigma_{x^r}x^r} \exp\left[-\frac{(\log x^r - \mu(x^t))^2}{2\sigma_{x^r}^2}\right]. \quad (3.9)$$

The parameters of the Gaussian are  $\sigma_{x^r}(x^t)$  and  $\mu(x^t)$ , which are functions of the true parameters. By multiplying the Gaussian in Eq. 3.9, we are reweighing the values by the probability density of that point. This process is also called *smearing* because it effectively spreads out the data around a certain point.

So how do we then obtain  $\sigma_{x^r}(x^t)$  and  $\mu(x^t)$  needed to construct the Gaussian? A Monte Carlo sample publicly released by the collaboration has all the ingredients that we need [13]. In Table. 3.4 we show a selection of the data. The ‘pdg’ column refers to the Monte Carlo particle classification, where 13 is the tag for  $\nu_\mu$ , while -13 refers to an  $\bar{\nu}_\mu$ . Here we note a crucial property of the IceCube dataset that will impact our analysis: the MC released by the collaboration only includes simulated muon events.

First, we let  $\cos(\theta_z^{reco}) = \cos(\theta_z^{true})$  for all values. The angular resolution in IceCube for track-like events is less than  $2^\circ$ , making  $\cos(\theta_z^{true})$  coincide with  $\cos(\theta_z^{reco})$

pdg	$E^{reco}$ [GeV]	$\cos(\theta_z^{reco})$	$E^{true}$ [GeV]	$\cos(\theta_z^{true})$
13	1665	-0.645884	592	-0.653421
13	587	-0.373241	342	-0.424979
-13	1431	-0.177786	1169	-0.189949
-13	831	-0.807226	1071	-0.805559
13	988	-0.370746	1861	-0.367922

Table 3.4: A selection of the data found in [13]

for our study [14]. Thus, we only need to concern ourselves with the energy resolution function. In Fig. 3.5, we have plotted all event counts found in the MC file, over 8 million. However, this is too much data to process efficiently, with many outliers that ultimately do not weigh in that much in the final event count. To resolve this, we have opted to train a Gaussian process regressor on the dataset, from which we can extract the predicted mean and standard deviation for a point. When doing this over  $E^{reco}$ , we sample  $E^{true}$  in the 99th percentile around the predicted mean. We then obtain the shaded band shown in Fig. 3.5.

Note that since atmospheric neutrino flux scales as  $E^{-2.7}$ , the log-normal Gaussian  $R(E^r, E^t)$  as  $E^{-2}$ , and the effective area is approximately linear in  $E$ . Thus, the event count in 3.8 will be proportional to  $E^{-1.7}$ . Having almost a quadratic drop-off, the event count as observed by IceCube will be lower and lower as we probe higher energies, severely limiting our confidence in TeV analyses due to lower statistical significance.

Now, Eq. 3.8 handles the Gaussian smearing, but we are not provided systematic error sources, DOM efficiencies, and other nuisance parameters. To correct this, we will aim to come as close as possible to the IceCube Monte Carlo, and then normalize with it. That way, we know that our null hypotheses will align while we are free to form additional hypotheses with different physics parameters.

The latest available data collected and processed by the collaboration contains 305,735 muon track events, collected over eight years [14]. The data has 13 logarithmically spaced bins in  $E^{reco} \in [500, 9976]$  GeV, and 20 linear bins in  $\cos(\theta_z^{reco}) \in [-1, 0]$ . The data is shown in Fig. 3.6.

## Monte Carlo normalization

Independent researchers outside of the IceCube collaboration will not be able to simulate the detector more precisely. The IceCube Monte Carlo is a complex and proprietary machinery, so our goal in this section is merely to come as close as we can to it. After we are confident that our code displays the same overall features

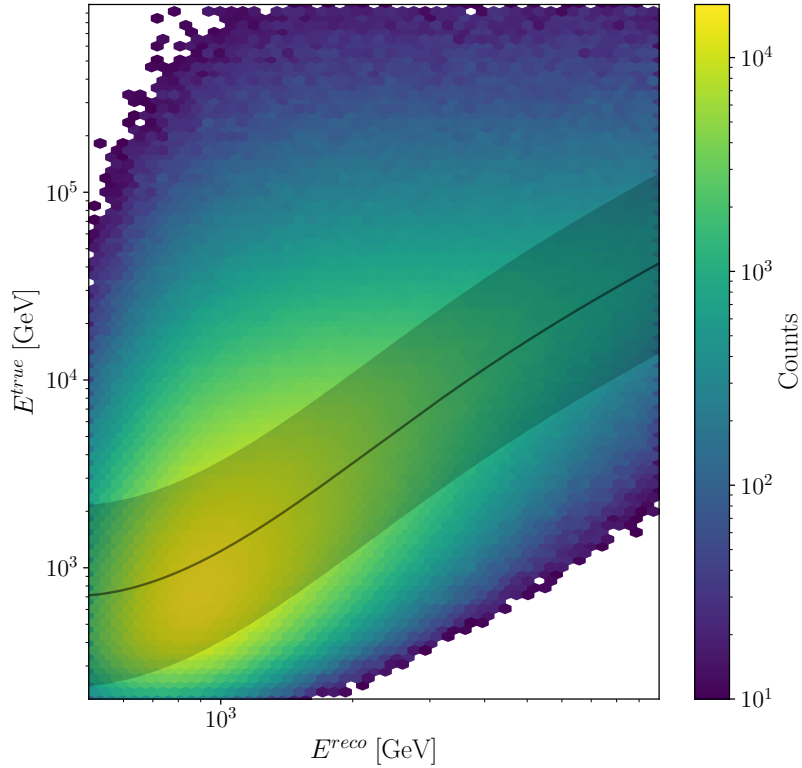


Figure 3.5: Relationship between the true and reconstructed muon energy in the IceCube MC sample [13]. The color indicates the frequency of each simulated point. Shaded area shows the 99th percentile limits predicted by the regressor trained on this set. It is within this band that then will sample the  $E^{true}$  values for each  $E^{reco}$ .

as the ‘official’, we normalize our results  $N_{ij}^{\text{sim}}$  as

$$N_{ij} = \frac{N_{ij}^{\text{null}}}{N_{ij}^{\text{MC}}} N_{ij}^{\text{sim}}. \quad (3.10)$$

For each bin  $i, j$ , we then obtain a correction factor that contains information that we are unable to obtain or sufficiently incorporate. One example of such information is the systematic errors of the DOMs. Recent IceCube data releases do not include such information. Since the systematic errors are affecting the event count on a bin-by-bin basis, they can, in theory, drastically modify the binned results. Another example of an error source that will be remedied by this method is the flux. We are using a fairly simple model of the atmospheric flux that excludes atmospheric prompt and astrophysical fluxes. The IceCube collaboration uses several different flux models, which are initialized by a parametrization of the cosmic ray flux.<sup>1</sup>

In Fig. 3.7, we present the IceCube Monte Carlo obtained from their 2020 sterile

---

<sup>1</sup>Included in the cosmic ray models are e.g. the pion to kaon ratio, which are often used as a nuisance parameter. By not being able to include this in our error analysis, our method will be limited to only consider the overall flux normalization rather than the components that produce the flux in the first place.

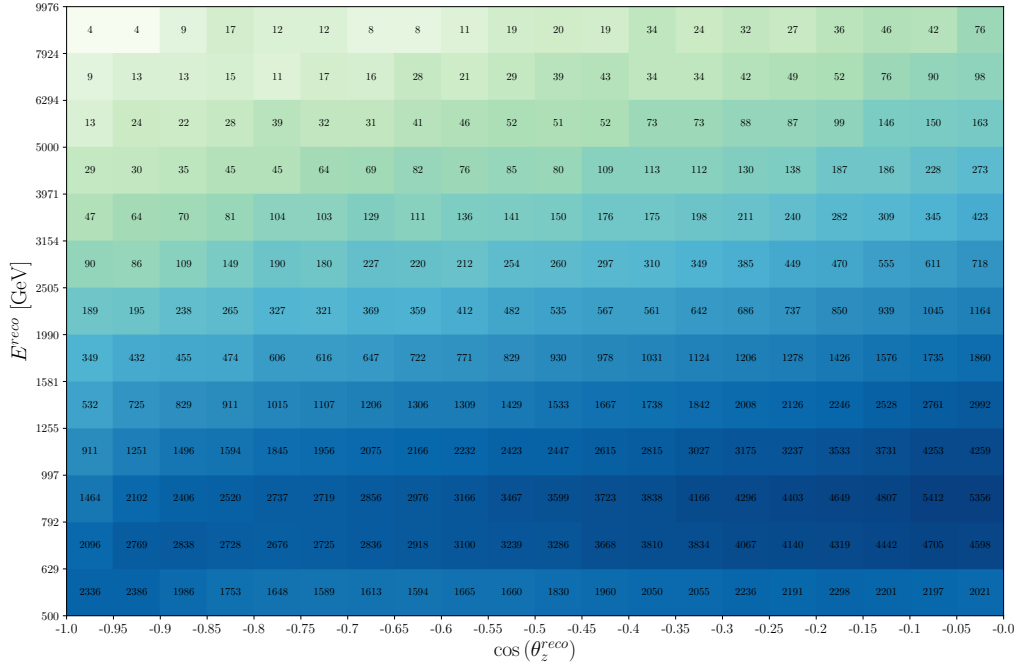


Figure 3.6: IceCube track events from [14], displaying the  $E^{-1.7}$  drop-off in event count.

analysis [14], along with our null hypothesis times a constant factor. We used the best-fit values from NuFit [5] with the exception of the CP-violating phase  $\delta_{\text{CP}}$ , which was set to  $0^\circ$  for simplicity. The values used are

$$\theta_{12} = 33.44^\circ, \quad \theta_{13} = 8.57^\circ, \quad \theta_{23} = 49.2^\circ, \quad \delta_{\text{CP}} = 0^\circ. \quad (3.11)$$

We deemed these shapes to be satisfactory, thus allowing us to multiply Eq. 3.8 by the correction factors of Eq. 3.10. Thus, we are now able to sufficiently approximate the IceCube Monte Carlo, which makes us able to run simulations based on different physics scenarios.

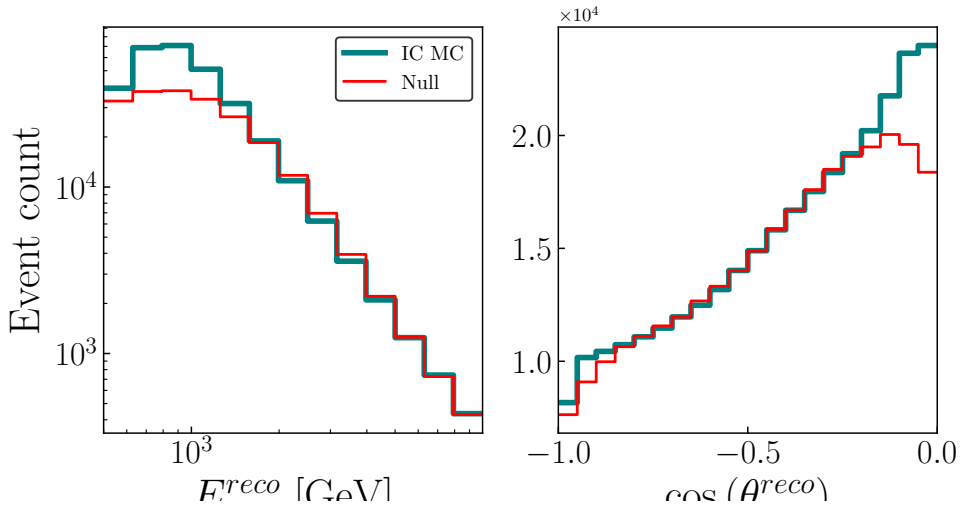


Figure 3.7: IceCube Monte Carlo, binned in  $E^{reco}$  and  $\cos(\theta_z^{reco})$ . We compare this with our simulations shown as ‘Null’ in the plots.

### 3.4 DeepCore

In this part, we use the publicly available DeepCore data sample [15] which is an updated version of what was used by the IceCube collaboration in a  $\nu_\mu$  disappearance analysis [16].

The detector systematics include ice absorption and scattering and overall, lateral, and head-on optical efficiencies of the DOMs. They are applied as correction factors using the best-fit points from the 2019 DeepCore  $\nu_\tau$  appearance analysis [9].

The data include 14901 track-like events and 26001 cascade-like events, both divided into eight  $\log_{10} E^{reco} \in [0.75, 1.75]$  bins, and eight  $\cos(\theta_z^{reco}) \in [-1, 1]$  bins. Each event has a Monte Carlo weight  $w_{ijk,\beta}$ , from which we can construct the event count as

$$N_{ijk} = C_{ijk} \sum_{\beta} w_{ijk,\beta} \phi_{\beta}^{\text{det}}, \quad (3.12)$$

where  $C_{k\beta}$  is the correction factor from the detector systematic uncertainty and  $\phi_{\beta}^{\text{det}}$  is defined as Eq. 3.3. We have now substituted the effect of the Gaussian smearing by treating the reconstructed and true quantities as a migration matrix.

### 3.5 PINGU

The methodology behind the PINGU simulations is the same as with our DeepCore study . We use the public MC [17], which allows us to construct the event count as in Eq. 3.12. However, since no detector systematics is yet modeled for PINGU, the correction factors  $C_{ijk}$  are all unity. As with the DeepCore data, the PINGU Monte Carlo is divided into eight  $\log_{10} E^{reco} \in [0.75, 1.75]$  bins, and eight  $\cos(\theta_z^{reco}) \in [-1, 1]$  bins for both track- and cascade-like events. We generate ‘data’ by predicting the event rates at PINGU with the following best-fit parameters from [5], except for the CP-violating phase, which is set to zero for simplicity.

$$\begin{aligned} \Delta m_{21}^2 &= 7.42 \times 10^{-5} \text{ eV}^2, & \Delta m_{31}^2 &= 2.517 \times 10^{-3} \text{ eV}^2, \\ \theta_{12} &= 33.44^\circ, & \theta_{13} &= 8.57^\circ, & \theta_{23} &= 49.2^\circ, & \delta_{\text{CP}} &= 0^\circ. \end{aligned} \quad (3.13)$$



## Chapter 4

### Beyond the $3\nu$ Picture

$$\mathcal{L}_{\text{NC}} = -2\sqrt{2}G_F \epsilon_{\alpha\beta}^{fX} (\bar{\nu}_\alpha \gamma^\mu P_L \nu_\beta)$$

## 4.1 The Sterile State

In 1996, the LSND experiment reported an excess of  $\bar{\nu}_e$  events from an  $\bar{\nu}_\mu$  beam [18]. Nine years later, MiniBooNE not only reproduced the  $\bar{\nu}_e$  anomaly but observed an excess in the  $\nu_e$  events too [19]. Together with the so-called reactor and gallium anomalies, these reports suggested that the three massive neutrino framework could be amended. By introducing a fourth heavy mass state  $\nu_4$ , both appearance and disappearance anomalies could be minimally accommodated. However, we know from the decay width of the  $Z$  boson that it only can interact with three flavor species<sup>1</sup>, so this fourth mass state cannot be interacting weakly. In other words, it needs to transform as a singlet under the gauge symmetry group  $SU(2)_L \times U(1)_Y$ . We now distinguish between the three original neutrino flavors ( $e$ ,  $\mu$ , and  $\tau$ ) and the new fourth flavor by calling the former *active* neutrinos and the latter *sterile* due to its non-interacting behavior.

The experiments listed above indicate that the mass-squared difference of the sterile neutrino is in the eV<sup>2</sup> scale, while the two others are three and five magnitudes smaller. To remind us of this hierarchy, we write  $3 + 1$ , since the sterile state proposed is heavier than the active states.

Two neutrino physics parameters probed by CMB lensing observations are the effective number of neutrinos  $N_{\text{eff}}$ , and the sum of neutrino masses  $\sum m_i$ . The 2018 results from the Planck Collaboration in [21] constrain the parameters to

$$N_{\text{eff}} = 2.96^{+0.34}_{-0.33}, \quad \sum m_i < 0.12 \text{ eV} \quad (95\%), \quad (4.1)$$

consistent with the Standard Model with oscillations<sup>2</sup> prediction of  $N_{\text{eff}} = 3.045$  degrees [22]. Assuming the Planck data, one thermalized sterile neutrino ( $N_{\text{eff}} = 4$ ) is excluded at  $6\sigma$ . Thus, thermalized sterile neutrinos are strongly in tension with cosmological observations if one does not consider some special mechanism. So if a fourth neutrino species is present in nature, it will have ramifications not only on neutrino physics itself, but on our understanding of the CMB as well.

### 4.1.1 The Hamiltonian

The inclusion of the sterile state in the Hamiltonian is straightforward. We extend the PMNS matrix with terms for the mixing between the new flavor ( $U_{si}$ ) and mass ( $U_{\alpha 4}$ ) eigenstates:

$$U_{4\text{gen}} = \begin{pmatrix} U_{e1} & U_{e2} & U_{e3} & U_{e4} \\ U_{\mu 1} & U_{\mu 2} & U_{\mu 3} & U_{\mu 4} \\ U_{\tau 1} & U_{\tau 2} & U_{\tau 3} & U_{\tau 4} \\ U_{s1} & U_{s2} & U_{s3} & U_{s4} \end{pmatrix}, \quad (4.2)$$

<sup>1</sup>Direct measurements of the invisible  $Z$  decay yields  $N = 2.92 \pm 0.05$  [20].

<sup>2</sup>Of course, the Standard Model *without* neutrino masses dictates  $N_{\text{eff}} = 3$  and  $\sum m_i \equiv 0$ .

where a common parametrization of this new mixing matrix is

$$U_{4gen} = R_{34}R_{24}R_{14}U_{3gen}. \quad (4.3)$$

This parametrization does not affect the physics, but determines the structure of the mixing angles.

The mass matrix extends analogously:

$$M_{4gen}^2 = \begin{pmatrix} 0 & 0 & 0 & 0 \\ 0 & \Delta m_{21}^2 & 0 & 0 \\ 0 & 0 & \Delta m_{31}^2 & 0 \\ 0 & 0 & 0 & \Delta m_{41}^2 \end{pmatrix}. \quad (4.4)$$

Now, the interaction with matter requires a careful reconsideration of the matter potential. We start off with the unaltered potential matrix from Eq. 2.42. Just as with the PMNS matrix, we extend this to  $4 \times 4$ :

$$\begin{pmatrix} V_{CC} + V_{NC} & 0 & 0 & 0 \\ 0 & V_{NC} & 0 & 0 \\ 0 & 0 & V_{NC} & 0 \\ 0 & 0 & 0 & 0 \end{pmatrix}. \quad (4.5)$$

Now we need to include the terms that describes the matter potential felt by the sterile flavor state. Recalling our discussion above, we remind ourselves that the sterile neutrino by definition does not participate in any interaction<sup>3</sup>. Thus, all potential terms involving the sterile state are zero. In other words, the potential matrix in Eq. 4.5 is complete, save for the usual subtraction by a constant times the identity matrix:

$$\begin{aligned} V_{4gen} &= \begin{pmatrix} V_{CC} + V_{NC} & 0 & 0 & 0 \\ 0 & V_{NC} & 0 & 0 \\ 0 & 0 & V_{NC} & 0 \\ 0 & 0 & 0 & 0 \end{pmatrix} - V_{NC} \begin{pmatrix} 1 & 0 & 0 & 0 \\ 0 & 1 & 0 & 0 \\ 0 & 0 & 1 & 0 \\ 0 & 0 & 0 & 1 \end{pmatrix} \\ &= \sqrt{2}G_F \begin{pmatrix} N_e & 0 & 0 & 0 \\ 0 & 0 & 0 & 0 \\ 0 & 0 & 0 & 0 \\ 0 & 0 & 0 & -N_n/2 \end{pmatrix} \\ &= \sqrt{2}G_F N_e \begin{pmatrix} 1 & 0 & 0 & 0 \\ 0 & 0 & 0 & 0 \\ 0 & 0 & 0 & 0 \\ 0 & 0 & 0 & -1/2 \end{pmatrix}. \end{aligned} \quad (4.6)$$

---

<sup>3</sup>The exception to this is of course gravity. The sterile neutrino is not massless.

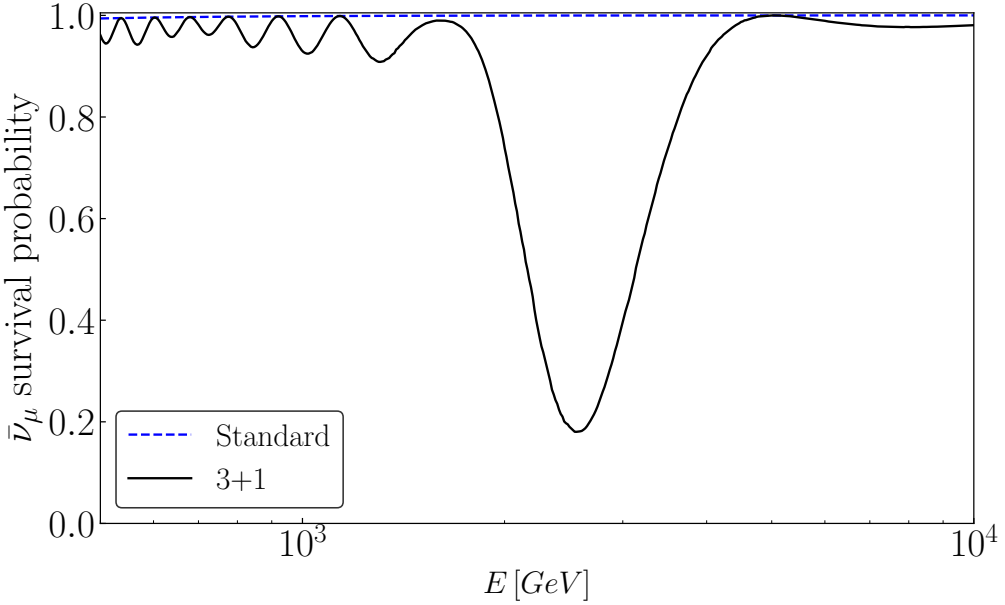


Figure 4.1: Comparing the standard 3+0 hypothesis to the 3+1 hypothesis assuming  $\Delta m_{41}^2 = 1 \text{ eV}^2$  and  $\theta_{24} = 0.04$ . The former, shown as a blue dashed line, shows no  $\bar{\nu}_\mu$  disappearance. The latter, shown as a black solid line, predicts a resonant  $\bar{\nu}_\mu$  disappearance at 2.6 TeV. The standard oscillation parameters are taken from NuFit [5], and the neutrino has traversed the entire Earth diameter.

where we have assumed electrical neutrality in the last step, yielding  $N_e = N_n$ . Thus, the final Hamiltonian with a fourth sterile neutrino is

$$H_{4gen} = \frac{1}{2E} \left[ U \begin{pmatrix} 0 & 0 & 0 & 0 \\ 0 & \Delta m_{21}^2 & 0 & 0 \\ 0 & 0 & \Delta m_{31}^2 & 0 \\ 0 & 0 & 0 & \Delta m_{41}^2 \end{pmatrix} U^\dagger \right] + \sqrt{2} G_F N_e \begin{pmatrix} 1 & 0 & 0 & 0 \\ 0 & 0 & 0 & 0 \\ 0 & 0 & 0 & 0 \\ 0 & 0 & 0 & -1/2 \end{pmatrix}. \quad (4.7)$$

Now, looking at Eqs. 4.3 and 4.4, we see that we have introduced four new parameters:  $\Delta m_{41}^2$ ,  $\theta_{14}$ ,  $\theta_{24}$ ,  $\theta_{34}$ . In our analysis, we reduce the number of parameters by only considering  $\Delta m_{41}^2$  and  $\theta_{24}$ , which are the most important for the  $\nu_\mu$  oscillations.

#### 4.1.2 The Probability Effect of a Sterile Neutrino

Since the new, sterile, neutrino does not interact weakly, how do we know if it's there? If the sterile mixing angle  $\theta_{i4}$  is non-zero, we allow the sterile mass state to mix with the active state  $i$ . The most interesting case is when  $\theta_{24} \neq 0$ , which for  $\Delta m_{41}^2 \sim \text{eV}^2$  gives rise to a resonant disappearance in the for  $P_{\bar{\mu}\bar{\mu}}$ , shown in Fig. 4.1.

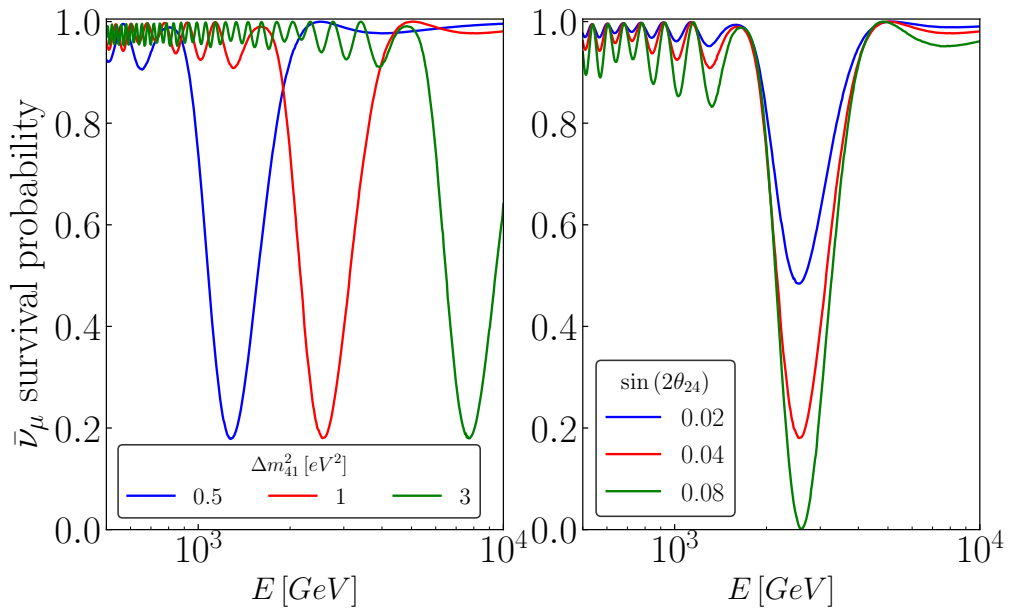


Figure 4.2: Shifting and amplification of the resonance by altering  $\Delta m_{41}^2$  and  $\theta_{24}$ , respectively. Left panel has a fixed value of  $\theta_{[24]} = 0.04$  while varying  $\Delta m_{41}^2$  from 0.5 to 3  $\text{TeV}^2$ . Right panel has a fixed value of  $\Delta m_{41}^2 = 1 \text{ TeV}^2$  while varying  $\theta_{[24]}$  from 0.02 to 0.08. Standard oscillation parameters are taken from NuFit [5], and shown in Eq. 3.13.

So for a eV<sup>2</sup>-scale sterile neutrino and a non-zero  $\theta_{24}$ , we expect a TeV  $\bar{\nu}_\mu$  disappearance. The resonance dip is affected by the value of  $\Delta m_{41}^2$  and  $\theta_{24}$  as shown in Fig. 4.2. We see how the value of  $\Delta m_{41}^2$  shifts the resonance peak, while the mixing angle amplifies it. In the 3 + 0 scenario,  $P_{\bar{\mu}\bar{\mu}} = 1$  in this range. Thus, if we are able to see a  $\bar{\nu}_\mu$  disappearance in the TeV region, we are in a good position to argue for an eV<sup>2</sup>-scale  $\Delta m_{41}^2$ .

Keeping in mind that the event count from Eq. 3.8 scales as  $E^{-1.7}$ , signals at higher energies will be more difficult to detect. Since higher values of  $\Delta m_{41}^2$  shift the  $P_{\bar{\mu}\bar{\mu}}$  resonance peak to higher energies, high  $\Delta m_{41}^2$  values will be harder to rule out because the event count is already lower, as compared to energies at single-digit TeV values. There is then a range of parameters with which our detector will be able to distinguish between the two hypotheses. Using the two-neutrino approximation<sup>4</sup>, we can rewrite the expression for MSW resonance from Eq. 2.66 as

$$E^* = \frac{\Delta m_{41}^2 \cos 2\theta_{24}}{2\sqrt{2}G_F N_e}, \quad (4.8)$$

which for  $\Delta m_{41}^2 = 1 \text{ TeV}^2$  and  $\theta_{24} = 0.04$ , gives us a resonance at  $E^* = 2.58 \text{ TeV}$ , matching the 3 + 1 simulation shown in Fig. 4.1. From the two-neutrino picture, we see that the resonance peak in the  $\bar{\nu}_\mu$  channel scales linearly with  $\Delta m_{41}^2$ , while the mixing angle dependence shows up as  $\cos 2\theta_{24}$ , which is between 0.987 and 0.999 for the  $\theta_{[24]}$  values considered in Fig. 4.2. Since our  $\theta_{24}$  values considered are so low, the location of the resonance peak is essentially only dependent on the value of  $\Delta m_{41}^2$ . Thus, we expect a more stringent constraint of low values of  $\Delta m_{41}^2$ , regardless of the value of  $\theta_{24}$ .

We also note that lower values of  $\theta_{24}$  suppresses the 3+1 signal, making it closer to the 3 + 0 hypothesis. Regardless of the value of  $\Delta m_{41}^2$ , the 3 + 1 hypothesis asymptotically converges to the 3 + 0 hypothesis as  $\theta_{24} \rightarrow 0$ .

---

<sup>4</sup>In this approximation, we only consider mixing between  $\nu_\mu$  and  $\nu_s$ , essentially a ‘1+1’ picture.

## 4.2 Non-Standard Interactions

We have no reason to believe that the Standard Model gauge group is the complete picture. We have already seen how the failure of the Standard Model to predict neutrino masses and oscillations forces us to amend it. Just as the electroweak theory  $SU(2)_L \times U(1)_Y$  is spontaneously broken to  $U(1)_{EM}$ , a higher order theory at a different energy scale with completely different properties might undergo a similar spontaneous symmetry break at high energies, producing at lower energies the Standard Model that we know. In fact, just as the fermion masses originate from the electroweak symmetry breaking, the neutrino masses might be generated from another broken symmetry resulting in the Standard Model gauge group. In this sense, the Standard Model might be considered an effective low energy theory, which yields impressive results in some areas but fails in others.

Compared to other fermions, the lightness of neutrino masses<sup>5</sup> along with their sparse SM interactions might indicate that these particles provide the best starting point for us to probe new physics, in which exotic neutrino interactions might occur [23]. We call these interactions non-standard interactions (NSI) in order to distinguish them from the ‘standard’ interactions of the Standard Model.

Following the approach of the Standard Model that the group generators uniquely determine the gauge bosons, a different gauge theory will have different interactions than those we presently know. These new interactions can be parametrized as model-independent four-fermion effective operators [24, 25]. Following the discussion in [26], we see that the NSI parameters  $\epsilon$  resulting from six-dimensional operators have the scale

$$\epsilon \propto \frac{m_W^2}{m_\epsilon^2} \sim \frac{10^{-2}}{m_\epsilon^2} \quad (4.9)$$

in TeV, so the new interactions generated at a mass scale of  $m_\epsilon = 1$  TeV will produce parameters in the order of  $10^{-2}$ , two magnitudes below the standard matter effect. Thus, if we assume the new interactions to arise from a higher-energy theory above electroweak scale, we then predict that the parameters contribute with at most a factor of  $10^{-2}$  to the standard matter effect, decreasing quadratically.

### 4.2.1 Non-Standard Effects on Neutrino Matter Interactions

Up until now, we have only considered weak neutrino interactions with electrons, protons, and neutrons. We can phenomenologically allow these interactions to include the up and down quarks which are present in the Earth as the fundamental

---

<sup>5</sup>The extreme lightness might be explained by a mass generation at a higher order theory.

components of neutrons and protons, as seen in the Lagrangians

$$\begin{aligned}\mathcal{L}_{\text{CC}} &= -2\sqrt{2}G_F \epsilon_{\alpha\beta}^{ff'X} (\bar{\nu}_\alpha \gamma^\mu P_L \ell_\beta) (\bar{f}' \gamma_\mu P_X f) \\ \mathcal{L}_{\text{NC}} &= -2\sqrt{2}G_F \epsilon_{\alpha\beta}^{fX} (\bar{\nu}_\alpha \gamma^\mu P_L \nu_\beta) (\bar{f} \gamma_\mu P_X f),\end{aligned}$$

where CC denotes the charged current interaction with the matter field  $f \neq f' \in \{u, d\}$ , and NC denotes the neutral current interaction with  $f \in \{e, u, d\}$ . The CC NSI effect affects neutrino production and detection, and will not be considered further. NC NSI affect the matter potential, and is thus of interest to us.

We have no independent sensitivity for the neither chirality nor flavor type of  $\epsilon^X$ , so we sum over these and study the effective matter NSI parameter  $\epsilon_{\alpha\beta}$ :

$$\epsilon_{\alpha\beta} = \sum_{X \in \{L, R\}} \sum_{f \in \{e, u, d\}} \frac{N_f}{N_e} \epsilon_{\alpha\beta}^{fX}. \quad (4.10)$$

Our matter study will be wholly confined to the interior of the Earth, where we assume electrical neutrality and equal distribution of neutrons and protons, we get  $N_u/N_e \simeq N_d/N_e \simeq 3$ . Also we assume the components  $\epsilon_{\alpha\beta}$  to be real. Thus,

$$\epsilon_{\alpha\beta} = \sum_X \epsilon_{\alpha\beta}^{eX} + 3(\epsilon_{\alpha\beta}^{uX} + \epsilon_{\alpha\beta}^{dX}) \quad (4.11)$$

Now,  $\epsilon_{\alpha\beta}$  enters the Hamiltonian as entries of a potential-like matrix. In Eq. 4.12,  $A_{CC}\text{diag}(1, 0, 0)$  is our familiar matter potential from the Standard Model. There is also our new term,  $A_{CC}\epsilon$ , which contains the components  $\epsilon_{\alpha\beta}$ :

$$\begin{aligned}H &= \frac{1}{2E} [UM^2U^\dagger + A_{CC} \text{diag}(1, 0, 0) + A_{CC}\epsilon] \\ &= \frac{1}{2E} \left[ UM^2U^\dagger + A_{CC} \begin{pmatrix} 1 + \epsilon_{ee} & \epsilon_{e\mu} & \epsilon_{e\tau} \\ \epsilon_{\mu e} & \epsilon_{\mu\mu} & \epsilon_{\mu\tau} \\ \epsilon_{\tau e} & \epsilon_{\tau\mu} & \epsilon_{\tau\tau} \end{pmatrix} \right]. \quad (4.12)\end{aligned}$$

In the limit  $\epsilon_{\alpha\beta} \rightarrow 0$ , we recover the standard interaction Hamiltonian from Eq. 2.56. We can draw several conclusions from this form of the Hamiltonian. Any nonzero off-diagonal element  $\epsilon_{\alpha\beta}, \alpha \neq \beta$  contribute to neutrino mixing, just as the off-diagonal elements of  $U$  does in the SM. Moreover, since the SM potential has the same order in  $A_{CC}$  as the NSIs, any  $\epsilon_{\alpha\beta} \sim 1$  will make the new matter effect be the same order as the SM effect.

We have two more modifications to the matrix  $\epsilon$ . First, all terms of the Hamiltonian must of course be Hermitian, thus

$$\begin{pmatrix} \epsilon_{ee} & \epsilon_{e\mu} & \epsilon_{e\tau} \\ \epsilon_{\mu e} & \epsilon_{\mu\mu} & \epsilon_{\mu\tau} \\ \epsilon_{\tau e} & \epsilon_{\tau\mu} & \epsilon_{\tau\tau} \end{pmatrix} = \begin{pmatrix} \epsilon_{ee} & \epsilon_{e\mu} & \epsilon_{e\tau} \\ \epsilon_{e\mu} & \epsilon_{\mu\mu} & \epsilon_{\mu\tau} \\ \epsilon_{e\tau} & \epsilon_{\mu\tau} & \epsilon_{\tau\tau} \end{pmatrix}. \quad (4.13)$$

Now we have reduced the possible number of NSI parameters from 9 down to 6.

By combining oscillation data and neutrino-nucleon scattering at the COHERENT experiment, 90 % CL ranges of some of the NSI parameters were constrained in [27] to

$$\begin{aligned} -0.090 &< \epsilon_{\tau\tau} < 0.38 \\ -0.01 &< \epsilon_{\mu\tau} < 0.009 \\ -0.073 &< \epsilon_{e\mu} < 0.044 \\ -0.15 &< \epsilon_{e\tau} < 0.13. \end{aligned} \quad (4.14)$$

### 4.2.2 IceCube Signal

The effect of NSI on the IceCube event count has been previously discussed in [24, 28, 25]. In our analysis of IceCube, we are constrained to muon track events. Thus, we are not able to test any theory which does not modify  $P_{\alpha\mu}$ . Moreover, the IceCube data is available in the range 500 GeV to 10 TeV range, where any rapid oscillations have averaged out.

Since all standard matter potentials are diagonal, the elements  $\epsilon_{\alpha\beta}$ ,  $\alpha = \beta$  will directly adjust the matter potential felt by flavor  $\alpha$ . The off-diagonal terms have a more interesting theoretical implication as they open up matter interactions across flavors. Remember, in the Standard model, we are restricted to weak interactions that conserve lepton flavor. However, an off-diagonal NSI parameter allows flavor transitions during matter interactions. Thus, the off-diagonal elements constitute new sources of flavor violation. Moreover,  $\epsilon_{\alpha\beta}$  modifies the  $\nu_\alpha \rightarrow \nu_\beta$  transition independently of the mixing matrix. Thus, we are not confined to the parameters of the mixing matrix: now we have introduced the possibility of additional interactions that can cause the flavor change. Moreover, since we have six NSI parameters, and the PMNS matrix is parametrized with only three parameters, we have more degrees of freedom when adjusting the probabilities using the NSI matrix. Each term in the PMNS matrix consists of at least two of the three mixing angles. This makes the individual angles more inter-dependent than the NSI parameters since combinations of them must satisfy the constraints of the matrix elements.

As discussed in Eq. 2.28, the atmospheric  $\nu_\mu \rightarrow \nu_\tau$  transition will be the most abundant, making  $\epsilon_{\mu\tau}$ ,  $\epsilon_{\mu\mu}$ ,  $\epsilon_{\tau\tau}$  the most suitable NSI parameters to constrain from muon events. As we will see,  $\epsilon_{e\mu}$  is also a candidate, albeit a weaker one.

In Fig. 4.3, we see how the introduction of  $\epsilon_{\mu\tau} = 0.02$  alters the  $\nu_\mu$  and  $\bar{\nu}_\mu$  survival probabilities for neutrinos that traverse the entire Earth diameter (i.e.  $\cos(\theta_z^{true}) = -1$ ).  $\epsilon_{\mu\tau}$  does not dramatically change neither amplitude nor frequency of the probabilities. Instead, it seems to stretch or compress the oscillations. Since the only difference between the way neutrinos and antineutrinos interact with matter is the sign of the potential, the probability for  $\nu_\mu$  with positive  $\epsilon_{\alpha\beta}$  is identical to the probability for  $\bar{\nu}_\mu$  with negative  $\epsilon_{\alpha\beta}$ . Thus, the dashed line in the right

panel not only shows the survival probability for  $\bar{\nu}_\mu$  with  $\epsilon_{\mu\tau} = 0.02$ , but also the survival probability for  $\nu_\mu$  with  $\epsilon_{\mu\tau} = -0.02$ . Hence, we note that  $\epsilon_{\mu\tau} > 0$  stretches (compresses)  $P_{\mu\mu}$  for neutrinos (antineutrinos), while  $\epsilon_{\mu\tau} < 0$  compresses (stretches)  $P_{\mu\mu}$  for neutrinos (antineutrinos).

The value of  $\epsilon_{\tau\tau}$  affects neither  $P_{\mu\mu}$  nor  $P_{\bar{\mu}\bar{\mu}}$ , in the IceCube region above 500 GeV. Hence, we will not be able to say anything about  $\epsilon_{\tau\tau}$  in our IceCube study. Comparing the probabilities in Fig. 4.3 with  $\epsilon_{\tau\tau} = 0.05$  with the ones for  $\epsilon_{\mu\tau} = 0.02$  in Fig. 4.3, we see that even though we let  $\epsilon_{\tau\tau}$  take 2.5 times the value of  $\epsilon_{\mu\tau}$ , its effect on  $P_{\mu\mu}$  is smaller. The weakening of the  $P_{\bar{\mu}\bar{\mu}}$  resonance will be visible in DeepCore, but we should expect a less stringent constraint due to the weakness of the effect compared to  $\epsilon_{\mu\tau}$ .

Thus, we will use IceCube to constrain  $\epsilon_{\mu\tau}$  only.

Moving on to  $\epsilon_{e\mu}$  and Fig. 4.4, we see that both probabilities has shifted downwards for  $E^{true} > 500$  GeV. In Fig. 4.4, we see that the muon channel remains largely unaffected of the value of  $\epsilon_{e\tau}$  as we expected. The exception of this lies in the DeepCore region of rapid oscillations, where mixing is more violent.

#### 4.2.3 DeepCore and PINGU Signals

The effect of NSI on the DeepCore event count has been previously discussed in [29], while the NSI effect in PINGU has been studied in [30, 31]. Now we repeat our probability analysis but for the DeepCore/PINGU region of 5.6 GeV to 56 GeV. As we previously saw, we have rapid oscillations, which means that ‘indirect’ modifications (i.e.  $\epsilon_{e\tau}$  will affect the  $P_{\mu\mu}$  channel) will be more apparent since all flavors are involved to a greater degree compared with the more stable region above 500 GeV, where many oscillations have averaged out.

Another feature of our DeepCore study includes the fact that we now have access to cascade events, in which  $\nu_e$  and  $\nu_\tau$  are more abundant. Thus, we are no longer constrained to the  $\mu$  channel alone, but we can now find interesting features in the other channels too. However, we remember that the  $\nu_\mu$  flux is still the most abundant.

Fig. 4.5 shows the electron neutrino and antineutrino survival probabilities, and here we see a clear signal when turning on  $\epsilon_{e\tau}$ .

Fig. 4.3 shows that  $\epsilon_{\mu\tau}$  affects both  $P_{\mu\mu}$  and  $P_{\bar{\mu}\bar{\mu}}$  over the whole energy range. Since IceCube also sees this, we hope to be able to boost the constraining of  $\epsilon_{\mu\tau}$  by combining the two experiments.

Regarding  $\epsilon_{\tau\tau}$  in Fig. 4.4, the signal mainly shows in the  $P_{\bar{\mu}\bar{\mu}}$  channel as a shallower dip in the 20 GeV region. Thus, DeepCore/PINGU alone will be used to constrain this parameter.

$\epsilon_{e\mu}$  in Fig. 4.4 causes a weaker dip for both  $\nu_\mu$  and  $\bar{\nu}_\mu$ .

For  $\epsilon_{e\tau}$ , we see a similar effect on the dip in  $P_{\mu\mu}$  as we did with  $\epsilon_{\tau\tau}$  for  $P_{\bar{\mu}\bar{\mu}}$ . Hence, we should be able to see the  $\epsilon_{e\tau}$  effect in DeepCore/PINGU. Remember that

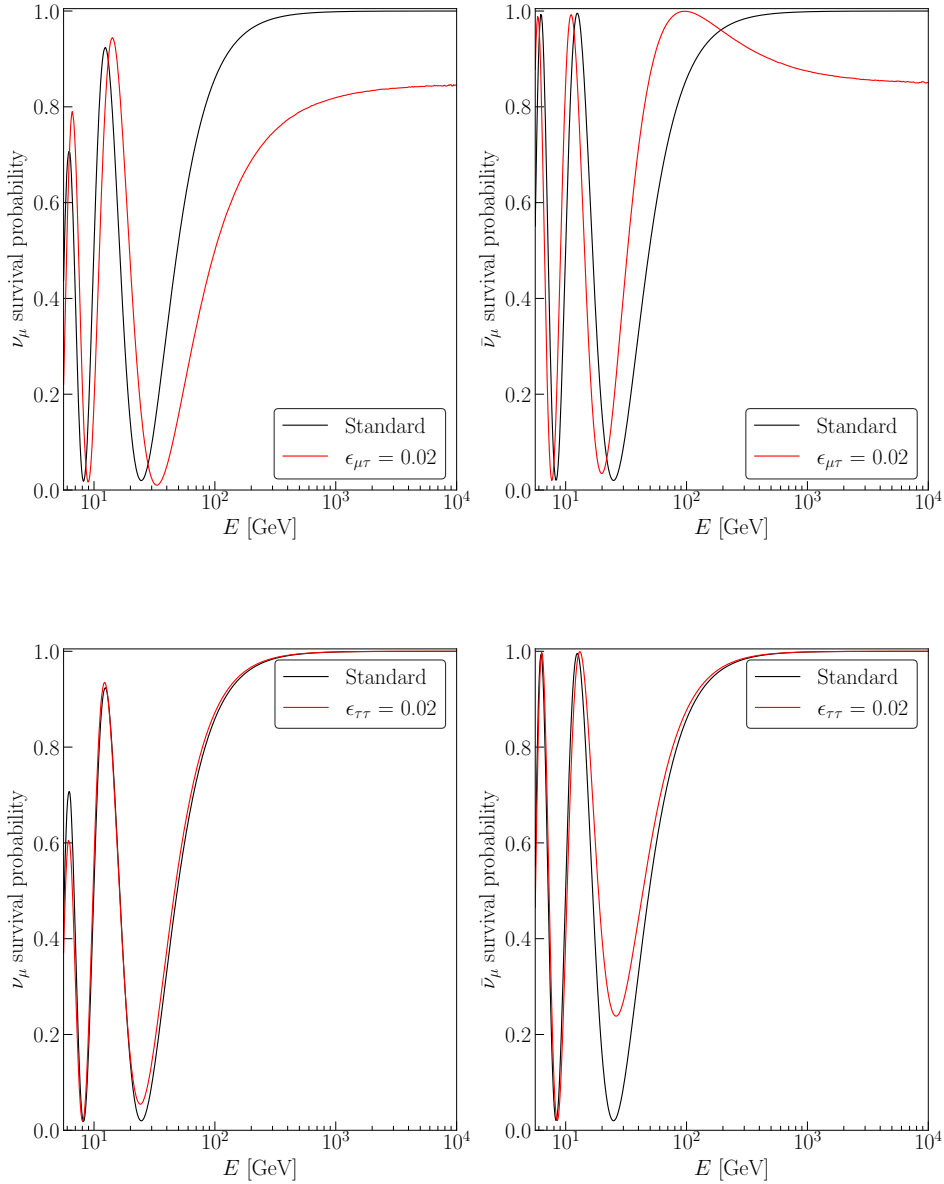


Figure 4.3: *Top panel:* Muon neutrino and antineutrino survival probabilities for  $\cos(\theta_z^{true}) = -1$  when  $\epsilon_{\mu\tau} = 0.02$ . All other NSI parameters are fixed to zero. In the GeV range,  $\epsilon_{\mu\tau}$  shifts the oscillations to the right for  $\nu_\mu$ , and to the left for  $\bar{\nu}_\mu$ . At TeV energies, both probabilities simply get shifted down, resulting in a net reduction of track events. *Bottom panel:* Muon neutrino and antineutrino survival probabilities for  $\cos(\theta_z^{true}) = -1$  when  $\epsilon_{\tau\tau} = 0.05$ . All other NSI parameters are fixed to zero.  $\epsilon_{\tau\tau}$  does not affect the probabilities above 100 GeV and this parameter is thus unable to be constrained by tracks in IceCube in our study. However, the dampening of the  $\bar{\nu}_\mu$  survival probability will be visible to DeepCore and PINGU, since it occurs within their energy ranges.

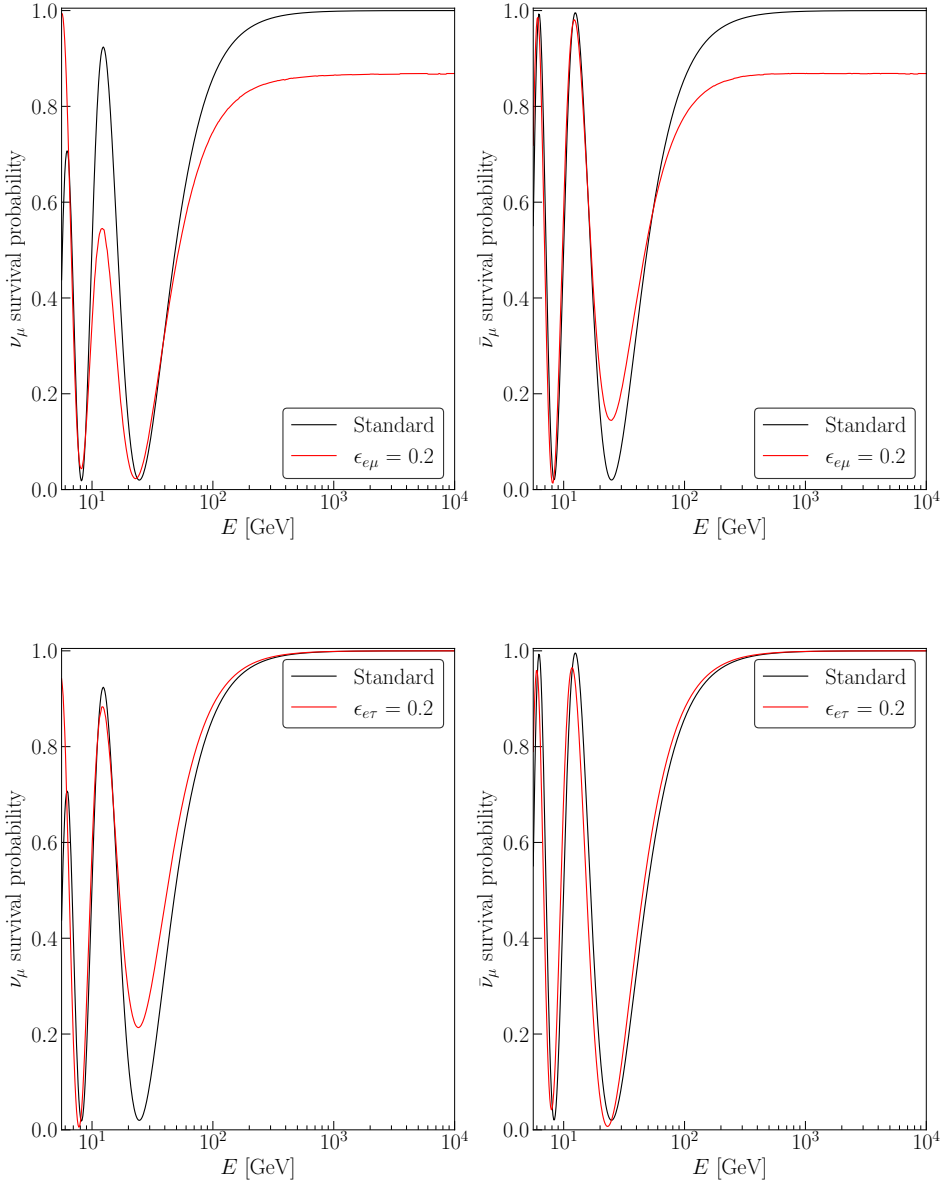


Figure 4.4: Muon neutrino and antineutrino survival probabilities for  $\cos(\theta_z^{true}) = -1$ . *Top panel:*  $\epsilon_{e\mu} = 0.2$ . All other NSI parameters are fixed to zero. Instead of the oscillations shifting to the left or right,  $\epsilon_{e\mu}$  dampens an oscillation peak for low GeV. At TeV, the probability is shifted down, just as with  $\epsilon_{\mu\tau}$ . *Bottom panel:*  $\epsilon_{e\tau} = 0.2$ . All other NSI parameters are fixed to zero. Here, we see a very weak shifting and a  $\nu_\mu$  weaker dip at low GeV, and again, no visible effect at TeV energies.

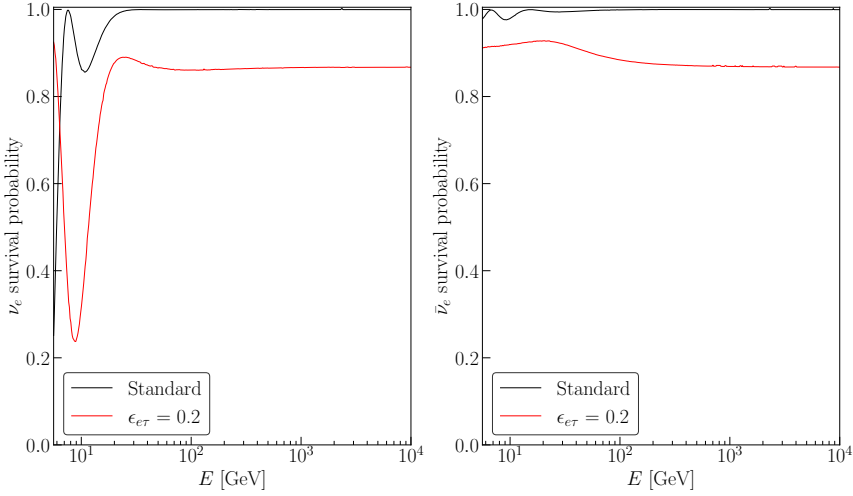


Figure 4.5: Electron neutrino and antineutrino survival probabilities for  $\cos(\theta_z^{true}) = -1$  when  $\epsilon_{e\tau} = 0.2$ . All other NSI parameters are fixed to zero. Here we see a strong difference across the whole energy range, in contrast to the  $\nu_\mu$  and  $\bar{\nu}_\mu$  plots in Fig 4.4.

we now have the option to look at the other flavor channels than  $\mu$  since we have cascade events for DeepCore and PINGU. If we simulate  $P_{\mu e}^{NSI}$  at three different energies, and let both  $\epsilon_{e\mu}$  and  $\epsilon_{e\tau}$  vary together between the values  $\{-0.3, 0.3\}$ , we produce a two-dimensional grid of probabilities. Subtract the regular  $P_{\mu e}^{SI}$  (that is, no NSI), and take the absolute value of the difference. We see the result in Fig. 4.6. The middle and right panels, which show the absolute probability difference at 25 and 50 GeV, respectively, are very bleak, indicating that the impact of the NSI parameters  $\epsilon_{e\mu}$  and  $\epsilon_{e\tau}$  is not as strong at these energy levels. Turning to the left-most panel, we see a region in which the difference again is close to zero, but now surrounded by fringes of very large differences, up to 50% difference in the  $P_{\mu e}$  probability. This indicates that the NSI parameters are much more influential at these energies, and that we should be able to constrain both  $\epsilon_{e\mu}$  and  $\epsilon_{e\tau}$  from 5 GeV cascade events.

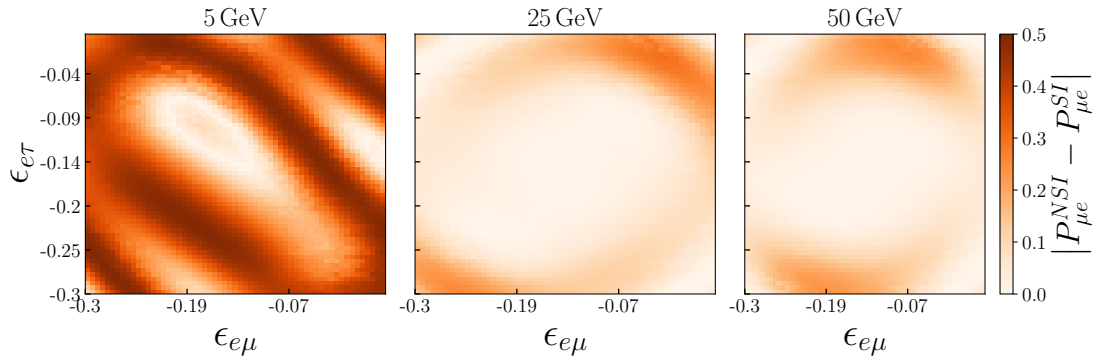
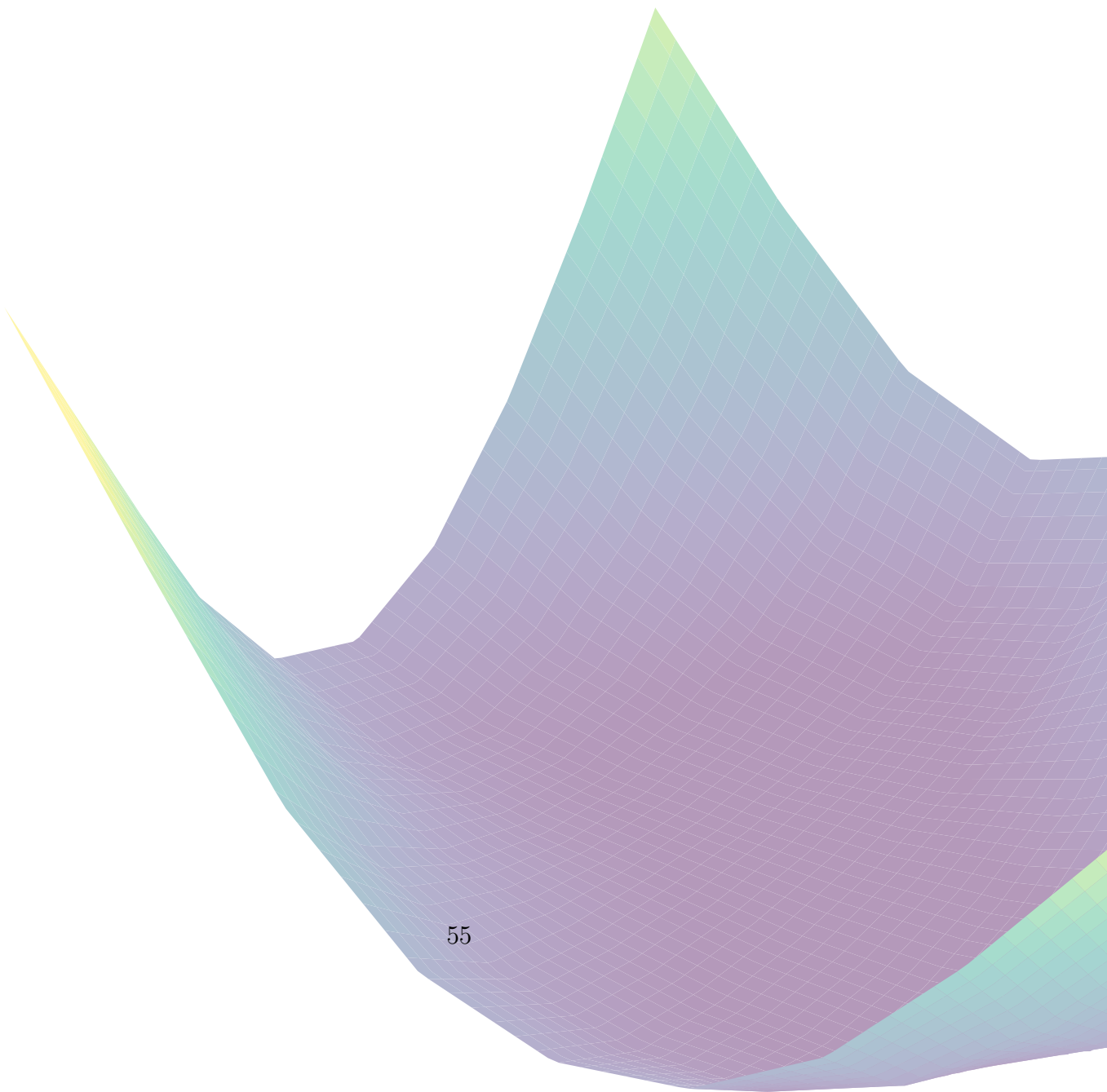


Figure 4.6: The quantity  $|P_{\mu e}^{NSI} - P_{\mu e}^{SI}|$  when we let  $\epsilon_{e\mu}$  and  $\epsilon_{e\tau}$  independently vary over the range  $\{-0.3, 0.3\}$  at 5, 25, and 50 GeV. At 5 GeV, we see strong deviations in the probabilities, showing a promising indication that constriction of  $\epsilon_{e\mu}$  and  $\epsilon_{e\tau}$  is possible using cascade events at these energies.

# Chapter 5

## Results



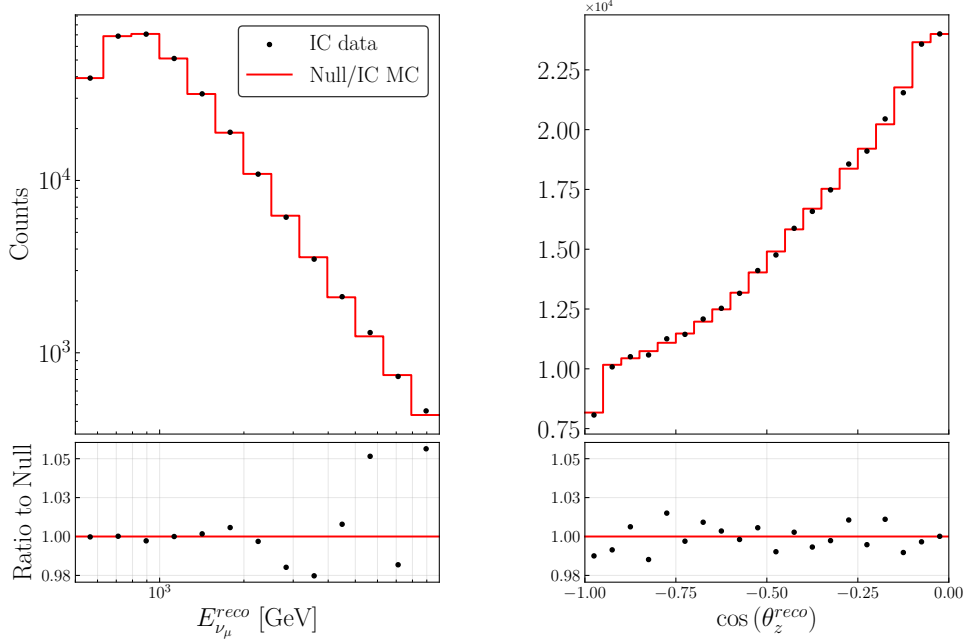


Figure 5.1: How the IceCube null hypothesis from [14] compares to their collected data.

## 5.1 The Sterile Neutrino Hypothesis

With the null ( $3\nu$ ) hypothesis normalized to the IceCube Monte Carlo as in Eq. 3.10, we are now in good shape to study the sterile neutrino effect on the probabilities, and how that compares to data<sup>1</sup>. First, let us see how the collected data from Fig. 3.6 deviates from the predicted  $3\nu$  oscillations. Fig. 5.1 shows an impressive agreement to the standard  $3\nu$  oscillation picture, with the largest deviations of 6% for neutrinos at 10 TeV values. In zenith, the data only deviates  $\pm 2\%$ .

### 5.1.1 $\chi^2$ Minimization

For our analyses, we define our  $\chi^2$  as

$$\chi^2(\hat{\theta}, \alpha, \beta) = \sum_{ij} \frac{(N_{ij}^{\text{th}} - N_{ij}^{\text{data}})^2}{(\sigma_{ij}^{\text{data}})^2 + (\sigma_{ij}^{\text{syst}})^2} + \frac{(1 - \alpha)^2}{\sigma_{\alpha}^2} + \frac{\beta^2}{\sigma_{\beta}^2} \quad (5.1)$$

where we minimize over the model parameters  $\hat{\theta}$ , the penalty terms  $\alpha$  and  $\beta$ .  $N_{ij}^{\text{th}}$  is the expected number of events from theory, and  $N_{ij}^{\text{data}}$  is the observed number of

---

<sup>1</sup>We do not consider DeepCore nor PINGU in the sterile neutrino analysis because the  $P_{\bar{\mu}\bar{\mu}}$  resonance does not appear in the GeV region for eV<sup>2</sup>-scale  $\Delta m_{41}^2$ , as shown in Fig. 4.1. We bring DeepCore and PINGU back in the next section.

events in that bin. We set  $\sigma_\alpha = 0.25$  as the atmospheric flux normalization error, and  $\sigma_\beta = 0.05$  as the zenith angle slope error [32]. The observed event number has an associated Poissonian uncertainty  $\sigma_{ij}^{\text{data}} = \sqrt{N_{ij}^{\text{data}}}$ . For IceCube, the event count takes the form

$$N_{ij}^{\text{th}} = \alpha [1 + \beta(0.5 + \cos(\theta_z^{\text{reco}})_i)] N_{ij}(\hat{\theta}), \quad (5.2)$$

with  $N_{ij}(\hat{\theta})$  from Eq. 3.10. Here, the term  $\beta(0.5 + \cos(\theta_z^{\text{reco}})_i)$  allows the event distribution to rotate with angle  $\beta$  around the median zenith angle of  $\cos(\theta_z^{\text{reco}}) = -0.5$ . We also have an uncorrelated systematic error  $\sigma_{ijk}^{\text{syst}}$ . We set  $\sigma_{ijk}^{\text{syst}} = f \sqrt{N_{ijk}^{\text{data}}}$ , where  $f$  is a factor of our own choosing.

The minimization of Eq. 5.1 simply returns a value for each set of model parameters. We use this value to quantify to what extent our theoretical simulations  $N_{ij}^{\text{th}}$  agree with the data  $N_{ij}^{\text{data}}$  within the error bounds provided by  $\sigma_a, \sigma_b$ , and  $f$ . We then select the smallest set of  $\chi^2$  values, and our allowed parameters are then their associated  $\hat{\theta}$ . We then translate the  $\chi^2$  distribution by subtracting the best-fit point, and analyze  $\Delta\chi^2 = \chi^2 - \chi^2_{\min}$ . From the  $\chi^2$ -distribution, one can show that the 90% confidence level has a value of 2.71 for two degrees of freedom. When slicing through the two-dimensional grid of  $\Delta\chi^2$  at this level, we then obtain a contour plot that tells us what parameter values are within our 90% confidence level and what regions are not.

### 5.1.2 Sterile Mass and Mixing

Let us start with looking at the best-fit event distribution resulting from the  $\chi^2$  minimization. Fig. 5.3 now contains the best-fit event distribution assuming the 3+1 hypothesis. The best-fit values are  $\Delta m_{41}^2 = 0.01 \text{ eV}^2$  and  $\sin(2\theta_{24})^2 = 0.67$  ( $\theta_{24} = 27.5^\circ$ ). The contour plot shown in Fig. 5.2 divides the parameter space into two regions. To the right of the boundary, the  $\Delta\chi^2$  has values above the confidence level, meaning that those parameter pairs can be excluded at a certain confidence level.

By tuning the scaling  $f$  of the uncorrelated systematic error, we can shift the contour. We extract the contour from the IceCube sterile neutrino analysis [14], and compare in Fig. 5.2. We see that the contour in the higher  $\Delta m_{41}^2$  region above  $1 \text{ eV}^2$  is very sensitive to the tuning, while the lower region between  $1 \times 10^{-1} \text{ eV}^2$  to  $1 \text{ eV}^2$  remains fixed. Using the case of 15% uncorrelated systematic error, we obtain best-fit values of  $\Delta m_{41}^2 = 0.01 \text{ eV}^2$  and  $\theta_{24} = 0.67$  ( $\sin^2 2\theta_{24} = 0.95$ ) at a p-value of 20%. This is not statistically significant, hence we find no evidence for a sterile neutrino within the parameter range  $0.01 \leq \Delta m_{41}^2 \leq 1 \text{ eV}^2, 0.01 \leq \sin(2\theta_{24})^2 \leq 1$  in IceCube data.

We now in Fig. 5.3 plot the best-fit 3+1 hypothesis with the data from Fig. 5.1, to finally see how the best 3+1 hypothesis compares to data.

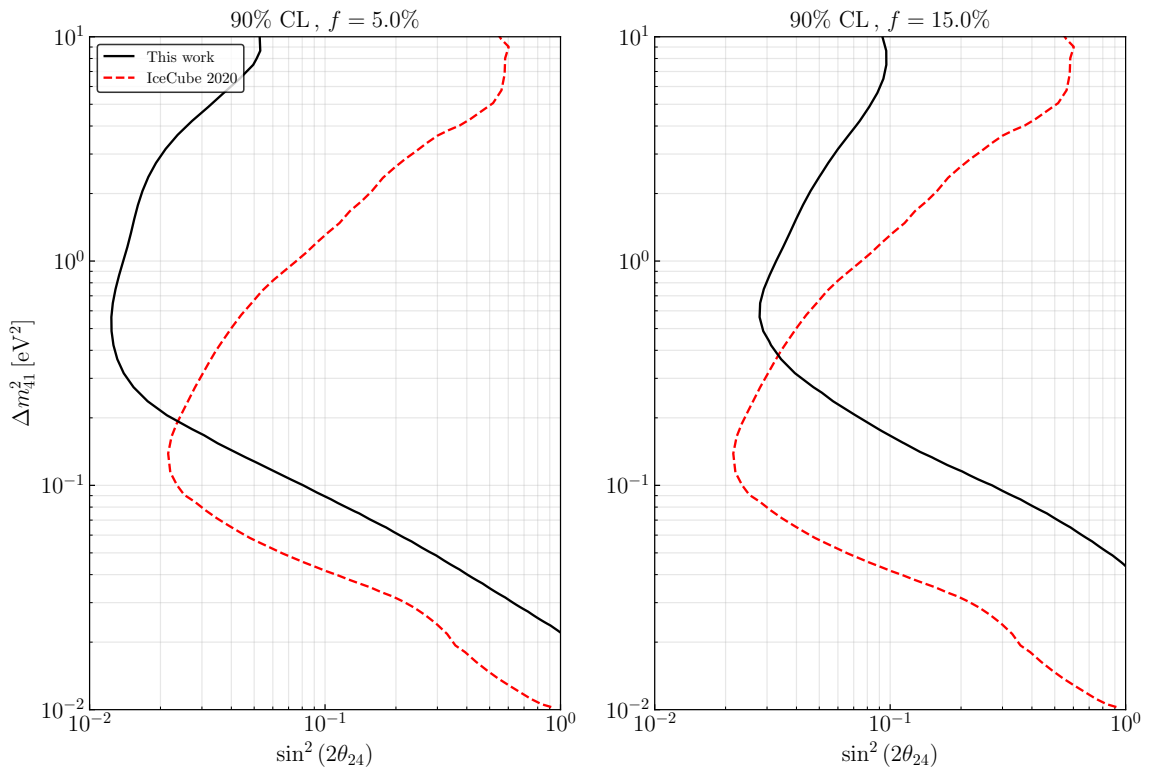


Figure 5.2: The 90% CL contour with two different systematic error scalings, compared with the official IceCube result from [14].

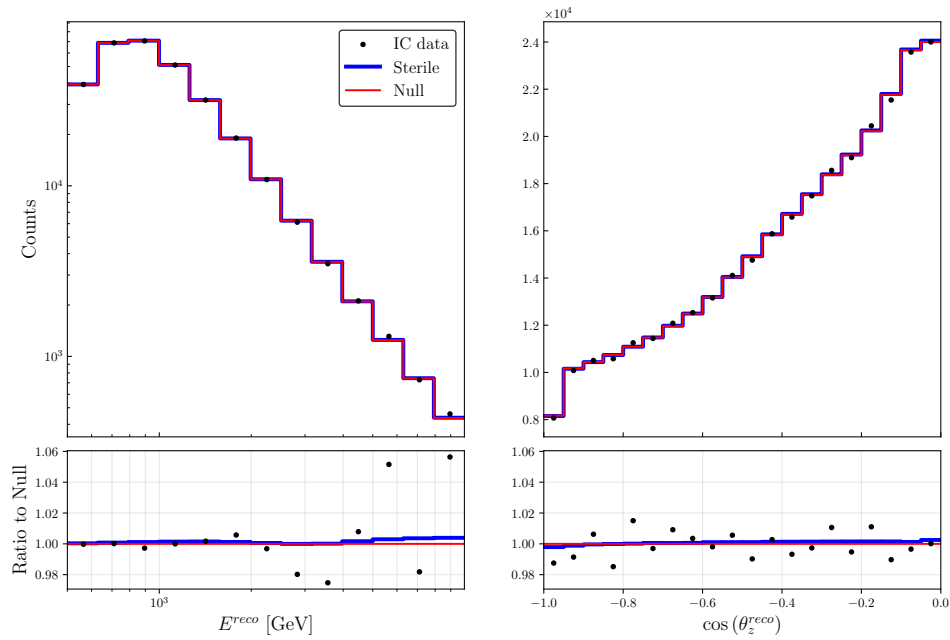


Figure 5.3: The predicted binned event count assuming our best-fit 3+1 hypothesis in blue with  $\Delta m_{41}^2 = 0.01 \text{ eV}^2$  and  $\theta_{24} = 0.67$ , compared with the null 3+0 hypothesis in red and data points from [14] in black.

Wanting to investigate the effect of  $\theta_{34}$ , we also simulated the 3+1 hypothesis using  $\theta_{24} = \theta_{34}$ . However, we did not see a difference in the exclusion regions compared to the regions when  $\theta_{34} = 0$ . Thus, we conclude that in our work, IceCube was not able to distinguish any effect due to the  $\theta_{34}$  parameter. However, since our dataset only included muon track events in the 0.5 TeV to 10 TeV range, one might be able to expect a larger effect of  $\theta_{34}$  if one includes cascade events as well.

## 5.2 The NSI Hypothesis

In this section, we will constrain the four NSI parameters  $\epsilon_{\tau\tau}$ ,  $\epsilon_{\mu\tau}$ ,  $\epsilon_{e\mu}$ , and  $\epsilon_{e\tau}$ . As we shall see, the impacts of NSI mainly manifest themselves at GeV energies, causing us to bring back DeepCore and PINGU. We will consider the results obtained from these three detectors separately as well as jointly.

### 5.2.1 $\chi^2$ Minimization

For our analyses, we define our  $\chi^2$  as

$$\chi^2(\hat{\theta}, \alpha, \beta, \kappa) = \sum_{ijk} \frac{(N^{\text{th}} - N^{\text{data}})_{ijk}^2}{(\sigma_{ijk}^{\text{data}})^2 + (\sigma_{ijk}^{\text{syst}})^2} + \frac{(1 - \alpha)^2}{\sigma_\alpha^2} + \frac{\beta^2}{\sigma_\beta^2} \quad (5.3)$$

where we minimize over the model parameters  $\hat{\theta} \in \{\Delta m^2, \theta_{23}, \epsilon\}$ , the penalty terms  $\alpha$  and  $\beta$ , and the free parameter  $\kappa$ .  $N_{ijk}^{\text{th}}$  is the expected number of events from theory in bin  $\{i, j, k\}$ , where  $i$  denotes the  $E^{\text{reco}}$  bin,  $j$  denotes the  $\cos(\theta_z^{\text{reco}})$  bin, and  $k$  denotes the event-type bin, i.e. track or cascade.  $N_{ijk}^{\text{data}}$  is the observed number of events in that bin.  $\sigma_{ijk}^{\text{data}}$  is the experimental uncertainty, and  $\sigma_{ijk}^{\text{syst}}$  the uncorrelated systematic uncertainty.

In our simulations of  $N_{ijk}^{\text{th}}$ , we set all standard oscillation parameters to their current best-fit values of Eq. 3.13, except for  $\Delta m_{31}^2$  and  $\theta_{23}$  which we vary over their  $3\sigma$  limits  $2.435 \times 10^{-3} \text{ eV}^2$  to  $2.598 \times 10^{-3} \text{ eV}^2$  and  $40.1^\circ$  to  $51.7^\circ$ , respectively [5].

We set  $\sigma_\alpha = 0.25$  as the atmospheric flux normalization error, and  $\sigma_\beta = 0.05$  as the zenith angle slope error [32]. The observed event number has an associated Poissonian uncertainty  $\sigma_{ijk}^{\text{data}} = \sqrt{N_{ijk}^{\text{data}}}$ . For IceCube, the event count takes the form

$$N_{ij}^{\text{th}} = \alpha [1 + \beta(0.5 + \cos(\theta_z^{\text{reco}})_i)] N_{ij}(\hat{\theta}), \quad (5.4)$$

with  $N_{ij}(\hat{\theta})$  from Eq. 3.8. Here, we allow the event distribution to rotate around the median cosine-zenith of  $\cos(\theta_z^{\text{reco}}) = -0.5$ . The event index  $k$  is omitted since we only have track events for IceCube.

For DeepCore and PINGU, and the event count takes the form

$$N_{ijk}^{\text{th}} = \alpha [1 + \beta \cos(\theta_z^{\text{reco}})_i] N_{ijk}(\hat{\theta}) + \kappa N_{ijk}^{\mu\text{atm}}, \quad (5.5)$$

with  $N_{ijk}(\hat{\theta})$  from Eq. 3.12.  $N_{ijk}^{\mu\text{atm}}$  is the muon background, which is left to float freely in the DeepCore analysis. The detectors experience an uncorrelated systematic error, which comes from the muon background, i.e. events misclassified as muons from  $\nu_\mu$  interactions rather than from pion decay. For the DeepCore analysis, we will have to consider this background when calculating the events. For IceCube events, we scan a higher energy range where the muon background can be

Experiment	Best case	Baseline	Worst case
IceCube	5%	10%	15%
PINGU	0%	3%	5%

Table 5.1: Our definition of the best, baseline, and worst case scenarios considered in each experiment, modelled by  $\sigma_{ijk}^{\text{syst}} = f \sqrt{N_{ijk}^{\text{data}}}$  with  $f$  from the table. We do not consider different DeepCore scenarios because her systematic error distribution is already provided in the data release [15].

neglected. For the PINGU events, the IceCube detector is expected to be able to act as a veto for this background. Thus, the error introduced from the muon background is expected by the collaboration to be negligible [11]. The background at PINGU can be considered negligible to first order [17], and we thus put  $\kappa = 0$  when calculating the PINGU  $\chi^2$ . For DeepCore and PINGU, the median cosine-zenith is  $\cos(\theta_z^{\text{reco}}) = 0$ , and we allow the event count to rotate around this point.

We treat the uncorrelated systematic uncertainties differently for each detector. For IceCube, we set  $\sigma_{ij}^{\text{syst}} = f \sqrt{N_{ij}^{\text{data}}}$ . We consider best, normal, and worst-case scenarios in IceCube using  $f = 5\%$ ,  $10\%$ , and  $15\%$  respectively. For PINGU, we use the same form but instead use  $f = 0\%$ ,  $3\%$ , and  $5\%$ . For DeepCore, we use the provided systematic error distribution which accounts for uncertainties in the finite MC statistics and the data-driven muon background estimate [15]. This is summarized in Table 5.1.

For the joint analysis, we follow the parameter goodness-of-fit prescription [33] and construct the joint  $\chi^2$  as

$$\chi_{\text{joint}}^2 = \sum_{\text{exp}} \chi_{\text{exp}}^2 - \chi_{\text{exp,min}}^2 \quad (5.6)$$

with test statistic  $\chi_{\text{joint,min}}^2$ . The  $\Delta\chi_{\text{joint}}^2$  is then  $\Delta\chi_{\text{joint}}^2 = \chi_{\text{joint}}^2 - \chi_{\text{joint,min}}^2$ .

### 5.2.2 Constraining the NSI parameters

We let each of the four NSI parameters considered assume a value, while keeping the other three fixed at zero. We consider the following ranges of values for each parameter:

$$\begin{aligned} -0.07 &\leq \epsilon_{\tau\tau} \leq 0.07 \\ -0.03 &\leq \epsilon_{\mu\tau} \leq 0.03 \\ -0.3 &\leq \epsilon_{e\mu} \leq 0.3 \\ -0.3 &\leq \epsilon_{e\tau} \leq 0.3 \end{aligned} \quad (5.7)$$

After the oscillation parameters  $\Delta m_{31}^2$  and  $\theta_{23}$  have been marginalized out, we plot  $\Delta\chi^2$  for each of the four NSI parameters in Fig. 5.4. The results are shown in Fig. 5.5 and summarized in Tables 5.2 and 5.3. Each region is bounded by the best and worst-case scenario, as defined in Table 5.1, while the middle line is the baseline scenario. We again emphasize that no uncertainty scenarios are considered for DeepCore, since they already provided in the data release [15].

Comparing the PINGU and the DeepCore results in Fig. 5.4, we note that the best-fit for each NSI parameter for the PINGU experiment is expected to be zero. This is because the ‘data’ we generated during the PINGU simulations assume no NSI since they have yet to be observed in nature. This introduces a non-NSI bias in all joint analyses, which include PINGU since PINGU has stronger statistics than DeepCore and will thus pull the joint  $\chi^2$  towards  $\epsilon = 0$ . Moreover, we see that we can expect PINGU to be sensitive to systematic uncertainty, especially when constraining  $\epsilon_{e\mu}$  and  $\epsilon_{e\tau}$  from the negative side.

We compare our results to a similar analysis performed on the same DeepCore dataset in [34]. In that publication, the constraints found at 90% CL were

$$\begin{aligned} -0.055 &< \epsilon_{\tau\tau} < 0.056 \\ -0.023 &< \epsilon_{\mu\tau} < 0.016 \\ -0.21 &< \epsilon_{e\mu} < 0.20 \\ -0.19 &< \epsilon_{e\tau} < 0.20 . \end{aligned} \quad (5.8)$$

Comparing 5.8 to our results from Table 5.2 at 90% CL, namely

$$\begin{aligned} -0.054 &< \epsilon_{\tau\tau} < 0.067 \\ -0.029 &< \epsilon_{\mu\tau} < 0.0070 \\ -0.12 &< \epsilon_{e\mu} < 0.15 \\ -0.084 &< \epsilon_{e\tau} < 0.15 , \end{aligned} \quad (5.9)$$

we see that our results for  $\epsilon_{e\mu}$ ,  $\epsilon_{e\tau}$  are more stringent, while the results for  $\epsilon_{\mu\tau}$  and  $\epsilon_{\tau\tau}$  are similar but more lenient. It is worth noting that the results from [34] are have been obtained by including more systematic uncertainties, such as the spectral index, hadron production, and baryon resonance. However, the overall flux normalization in [34] is 20%, while we opted for a slightly higher figure of 25%, which could compensate for the exclusion of the statistical uncertainties mentioned.

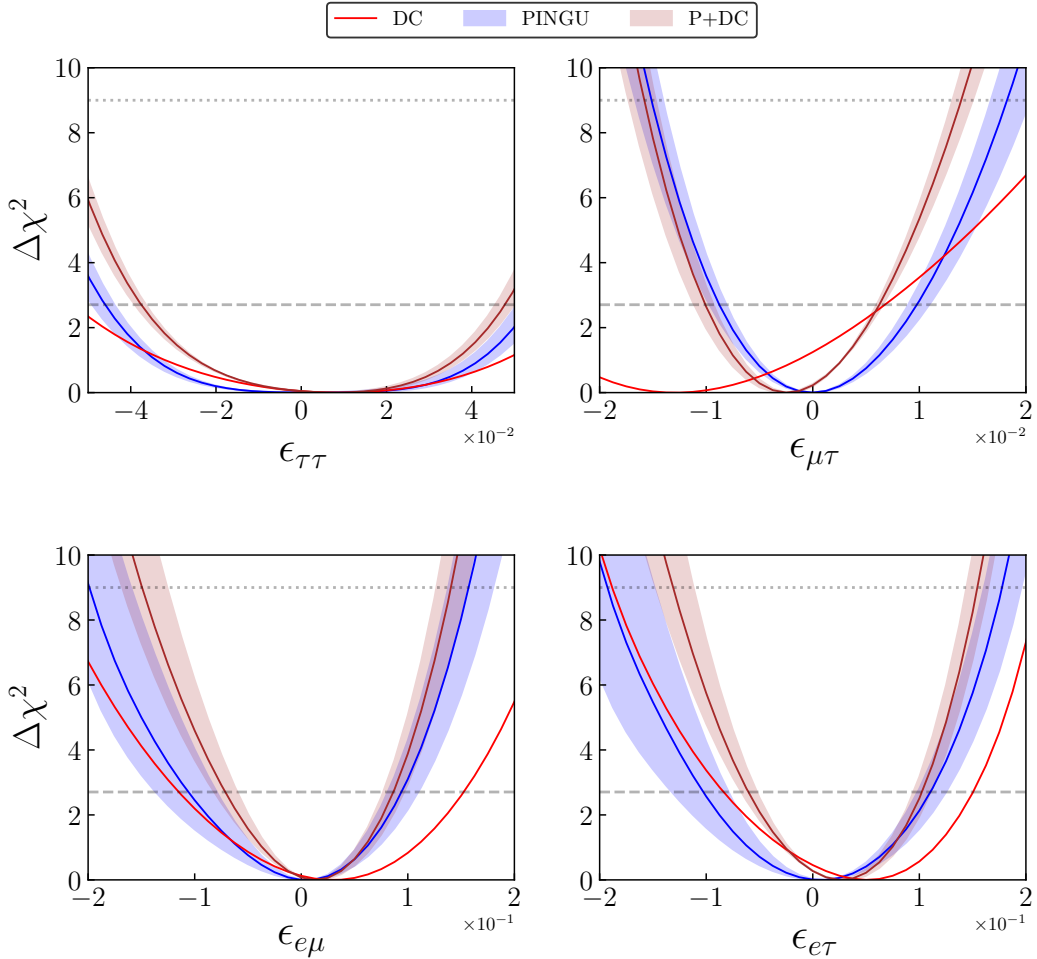


Figure 5.4: Confidence regions for PINGU and DeepCore scenarios listed in Table 5.1, with their joint  $\Delta\chi^2$  in maroon.  $\Delta m_{31}^2$  and  $\theta_{23}$  have been marginalized out, and all other NSI parameters not shown in each panel are fixed to zero. IceCube tracks only reveal  $\epsilon_{\mu\tau}$ , and are displayed separately in Fig. 5.5. Dotted lines are the 90% and 3 $\sigma$  CL levels.

Parameter	Best 90% CL	Best $3\sigma$
IceCube		
$\epsilon_{\mu\tau}$	[-0.012, 0.011]	[-0.017, 0.016]
DeepCore		
$\epsilon_{\tau\tau}$	[-0.054, 0.067]	[-0.089, 0.10]
$\epsilon_{\mu\tau}$	[-0.029, 0.0070]	[-0.041, 0.026]
$\epsilon_{e\mu}$	[-0.12, 0.15]	[-0.23, 0.24]
$\epsilon_{e\tau}$	[-0.084, 0.15]	[-0.19, 0.21]
IceCube + DeepCore		
$\epsilon_{\mu\tau}$	[-0.013, 0.0070]	[-0.017, 0.013]

Parameter	Baseline 90% CL	Baseline $3\sigma$
IceCube		
$\epsilon_{\mu\tau}$	[-0.015, 0.014]	[-0.022, 0.021]
DeepCore		
$\epsilon_{\tau\tau}$	[-0.054, 0.067]	[-0.089, 0.10]
$\epsilon_{\mu\tau}$	[-0.029, 0.0070]	[-0.041, 0.026]
$\epsilon_{e\mu}$	[-0.12, 0.15]	[-0.23, 0.24]
$\epsilon_{e\tau}$	[-0.084, 0.15]	[-0.19, 0.21]
IceCube + DeepCore		
$\epsilon_{\mu\tau}$	[-0.016, 0.0070]	[-0.022, 0.016]

Parameter	Worst 90% CL	Worst $3\sigma$
IceCube		
$\epsilon_{\mu\tau}$	[-0.018, 0.017]	[-0.025, 0.024]
DeepCore		
$\epsilon_{\tau\tau}$	[-0.054, 0.067]	[-0.089, 0.10]
$\epsilon_{\mu\tau}$	[-0.029, 0.0070]	[-0.041, 0.026]
$\epsilon_{e\mu}$	[-0.11, 0.15]	[-0.23, 0.24]
$\epsilon_{e\tau}$	[-0.084, 0.15]	[-0.188, 0.212]
IceCube + DeepCore		
$\epsilon_{\mu\tau}$	[-0.018, 0.0070]	[-0.024, 0.018]

Table 5.2: IceCube and DeepCore results from the  $\Delta\chi^2$  in Fig. 5.5.  $\Delta m_{31}^2$  and  $\theta_{23}$  have been marginalized out, and all other NSI parameters other than the one shown for each row are set to zero. Best, baseline, and worst refer to the systematic uncertainty scenarios considered as in Table 5.1.

Parameter	Best 90% CL	Best $3\sigma$
PINGU		
$\epsilon_{\tau\tau}$	[-0.044, 0.051]	[-0.062, 0.069]
$\epsilon_{\mu\tau}$	[-0.008, 0.009]	[-0.014, 0.017]
$\epsilon_{e\mu}$	[-0.079, 0.081]	[-0.16, 0.138]
$\epsilon_{e\tau}$	[-0.079, 0.098]	[-0.148, 0.161]
DeepCore + PINGU		
$\epsilon_{\tau\tau}$	[-0.036, 0.046]	[-0.056, 0.064]
$\epsilon_{\mu\tau}$	[-0.0090, 0.0060]	[-0.015, 0.013]
$\epsilon_{e\mu}$	[-0.060, 0.077]	[-0.13, 0.13]
$\epsilon_{e\tau}$	[-0.052, 0.095]	[-0.11, 0.14]
IceCube + DeepCore + PINGU		
$\epsilon_{\mu\tau}$	[-0.0080, 0.0050]	[-0.012, 0.011]
Parameter	Baseline 90% CL	Baseline $3\sigma$
PINGU		
$\epsilon_{\tau\tau}$	[-0.046, 0.054]	[-0.065, 0.073]
$\epsilon_{\mu\tau}$	[-0.0090, 0.010]	[-0.015, 0.018]
$\epsilon_{e\mu}$	[-0.11, 0.094]	[-0.20, 0.16]
$\epsilon_{e\tau}$	[-0.10, 0.11]	[-0.19, 0.18]
DeepCore + PINGU		
$\epsilon_{\tau\tau}$	[-0.038, 0.048]	[-0.058, 0.067]
$\epsilon_{\mu\tau}$	[-0.010, 0.0060]	[-0.016, 0.014]
$\epsilon_{e\mu}$	[-0.071, 0.086]	[-0.15, 0.14]
$\epsilon_{e\tau}$	[-0.061, 0.10]	[-0.13, 0.16]
IceCube + DeepCore + PINGU		
$\epsilon_{\mu\tau}$	[-0.009, 0.0060]	[-0.014, 0.012]
Parameter	Worst 90% CL	Worst $3\sigma$
PINGU		
$\epsilon_{\tau\tau}$	[-0.049, 0.057]	[-0.07, 0.078]
$\epsilon_{\mu\tau}$	[-0.01, 0.011]	[-0.017, 0.02]
$\epsilon_{e\mu}$	[-0.137, 0.11]	[-0.228, 0.18]
$\epsilon_{e\tau}$	[-0.132, 0.125]	[-0.226, 0.196]
DeepCore + PINGU		
$\epsilon_{\tau\tau}$	[-0.039, 0.050]	[-0.060, 0.070]
$\epsilon_{\mu\tau}$	[-0.011, 0.0070]	[-0.017, 0.015]
$\epsilon_{e\mu}$	[-0.082, 0.097]	[-0.168, 0.16]
$\epsilon_{e\tau}$	[-0.067, 0.11]	[-0.15, 0.17]
IceCube + DeepCore + PINGU		
$\epsilon_{\mu\tau}$	[-0.010, 0.0060]	[-0.016, 0.013]

Table 5.3: PINGU and joint results from the  $\Delta\chi^2$  in Fig. 5.4.  $\Delta m_{31}^2$  and  $\theta$ [23] have been marginalized out, and all other NSI parameters other than the one shown for each row are set to zero. Best, baseline, and worst refer to the systematic uncertainty scenarios considered as in Table 5.1.

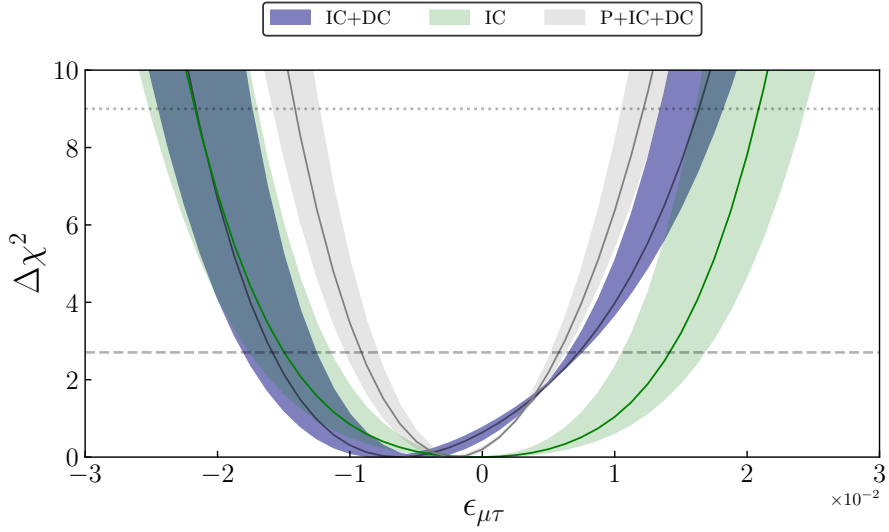


Figure 5.5:  $\epsilon_{\mu\tau}$   $\Delta\chi^2$  regions for scenarios as defined in Table 5.1.  $\Delta m_{31}^2$  and  $\theta_{23}$  have been marginalized out, and all other NSI parameters other than  $\epsilon_{\mu\tau}$  are fixed to zero. Dotted lines are the 90% and 3 $\sigma$  CL levels. The zones contain the three uncertainty scenarios considered, and we see that the inclusion of PINGU is expected to drastically make the bound on  $\epsilon_{\mu\tau}$  more stringent.

Parameter	Best fit		
	$\Delta m_{31}^2$	$\theta_{23}$	$\epsilon$
DeepCore			
$\epsilon_{\tau\tau}$	2.435	47.84	0.0125
$\epsilon_{\mu\tau}$	2.435	43.97	-0.005
$\epsilon_{e\mu}$	2.435	43.97	0
$\epsilon_{e\tau}$	2.435	43.97	0.05
IceCube			
$\epsilon_{\mu\tau}$	2.435	51.70	0
IceCube + DeepCore			
$\epsilon_{\mu\tau}$	2.517	43.97	-0.01

Table 5.4: Best fit points for  $\Delta m_{31}^2$  and  $\theta_{23}$  are given in units of  $10^{-3}\text{eV}^2$  and degrees, respectively.

Using the baseline case of 3% systematic uncertainty at 90% CL, we find from Table 5.3, that our predictions for the proposed PINGU detector are

$$\begin{aligned} -0.049 &< \epsilon_{\tau\tau} < 0.057 \\ -0.010 &< \epsilon_{\mu\tau} < 0.011 \\ -0.137 &< \epsilon_{e\mu} < 0.11 \\ -0.132 &< \epsilon_{e\tau} < 0.125, \end{aligned} \quad (5.10)$$

which displays an improvement over the DeepCore results in Eq. 5.9, except for  $\epsilon_{e\tau}$  which is worse.

Finally, the joint results for  $\epsilon_{\mu\tau}$  using IceCube and DeepCore from 5.3 at 90% CL are

$$-0.016 < \epsilon_{\mu\tau} < 0.0070, \quad (5.11)$$

and when combining IceCube, DeepCore, and PINGU, the 90% CL constraint on  $\epsilon_{\mu\tau}$  in our baseline scenario is predicted to be

$$-0.010 < \epsilon_{\mu\tau} < 0.0060, \quad (5.12)$$

which is more stringent for  $\epsilon_{\mu\tau} > 0$  than the result in [35].

We plot the event pull  $(N_{NSI} - N_{SI})/\sqrt{N_{SI}}$  where  $N_{(N)SI}$  are the numbers of expected events assuming (non-)standard interactions in Fig. 5.6. This gives the normalized difference in the number of expected events at the detector and illustrates the expected sensitivity of DeepCore for the NSI parameters.

Now we will compare the probability plots with the final event counts in DeepCore. It is not enough to only study the effect at probability level, since that is in true quantities. Since the detector data comes in reconstructed quantities, it might be the case that a feature at probability level gets averaged out in the reconstruction, and not showing up at all in the data. In general, features showing at probability level can be averaged out at reconstruction if they occur in the rapidly oscillating part of single-digit GeV energies.

The top right panel shows a surplus of DeepCore track events at 20 GeV to 30 GeV for through-going neutrinos when we turn on  $\epsilon_{\tau\tau}$ . This is what we expected from the bottom right panel in Fig. 4.3, where we saw that we had an increase in  $\bar{\nu}_\mu$  survival probability at 20 GeV to 40 GeV.

The third right panel shows the expected event pull for  $\epsilon_{e\mu}$ . Comparing with the probabilities in Fig. 4.4, we see that the surplus of the  $\bar{\nu}_\mu$  survival in the 20 GeV to 30 GeV and the deficit above 40 GeV is intact, while the 10 GeV  $\nu_\mu$  deficit is completely averaged out.

There is no reason for us to assume that only one NSI parameter exists in Nature, unless we impose a symmetry on the gauge group which generates NSI. For example, the matter potential matrix in our Hamiltonian from Eq. (2.42) is diagonal since

the interaction Lagrangian respects lepton flavor conservation. So ideally, we would simulate a grid where all NSI parameters are allowed to vary, but this is not feasible. Thus, we take we set  $\epsilon_{\tau\tau} = 0$  and let  $\epsilon_{\mu\tau}, \epsilon_{e\mu}, \epsilon_{e\tau}$  vary, along with  $\Delta m_{31}^2$  and  $\theta_{23}$ . We let  $\epsilon_{\tau\tau} = 0$  because we saw that it did not influence the other parameters. We then marginalize out the standard oscillation parameters and one of the NSI parameters and plot the remaining two in Fig. 5.7. We see that the pairs  $\epsilon_{e\mu} - \epsilon_{\mu\tau}$  and  $\epsilon_{e\tau} - \epsilon_{\mu\tau}$  are symmetrical. Hence, we can see that no relationship exists between them. With  $\epsilon_{e\tau} - \epsilon_{e\mu}$ , however, the contours are assuming a different shape. The contour allows positive values of  $\epsilon_{e\tau}$  and  $\epsilon_{e\mu}$  to a greater degree than mixed or negative values. Thus, we can draw the conclusion that, given  $\epsilon_{\tau\tau} = 0$ , PINGU might expect to observe that  $\epsilon_{e\mu}$  and  $\epsilon_{\mu\tau}$  are anti-correlated while we expect no significant correlation to be seen between the pairs  $\epsilon_{\mu\tau} - \epsilon_{e\mu}$ , and  $\epsilon_{\mu\tau} - \epsilon_{e\tau}$ . This is consistent with our observation of the effect of these parameters on  $P_{\mu e}$  in Fig. 4.6, from which we saw that  $\epsilon_{e\mu}$  and  $\epsilon_{e\tau}$  strongly affect  $P_{\mu e}$  for single-digit GeV energies.

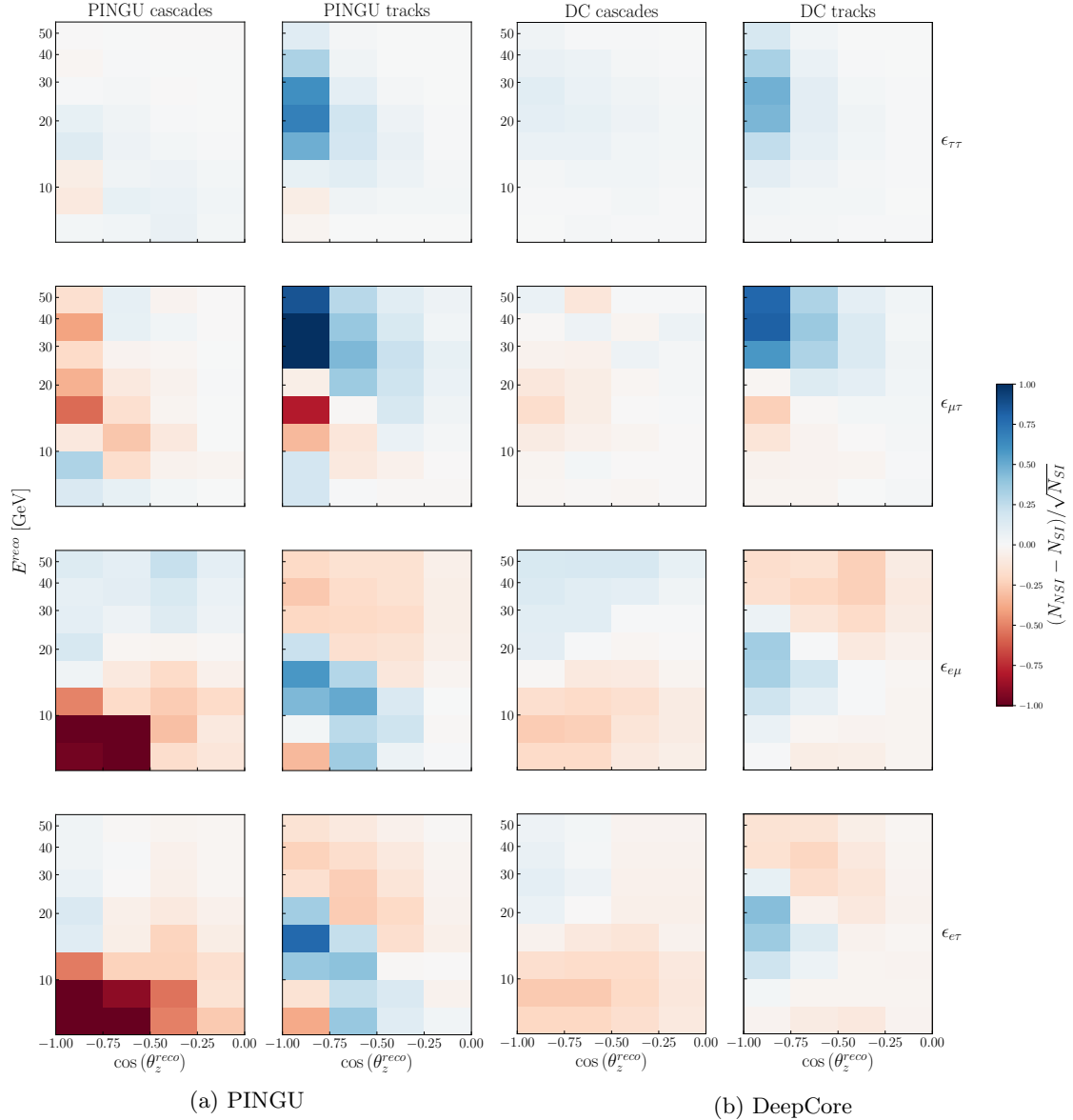


Figure 5.6: Expected pulls of the form  $(N_{NSI} - N_{SI})/\sqrt{N_{SI}}$  for PINGU and DeepCore after 3 years of data. Each row has only one NSI non-zero parameter, with the first row having  $\epsilon_{\tau\tau} = -0.07$ , second  $\epsilon_{\mu\tau} = -0.03$ , third  $\epsilon_{e\mu} = -0.3$ , and fourth  $\epsilon_{e\tau} = -0.3$ . We clearly see the increased statistics of the PINGU detector, especially in cascade events. The low values of  $\epsilon_{\tau\tau}$  and  $\epsilon_{\mu\tau}$  produce a weak pull in DeepCore, while PINGU can be expected to observe multiple regions of strong pulls for  $\epsilon_{\mu\tau}$ ,  $\epsilon_{e\mu}$ , and  $\epsilon_{e\tau}$ .

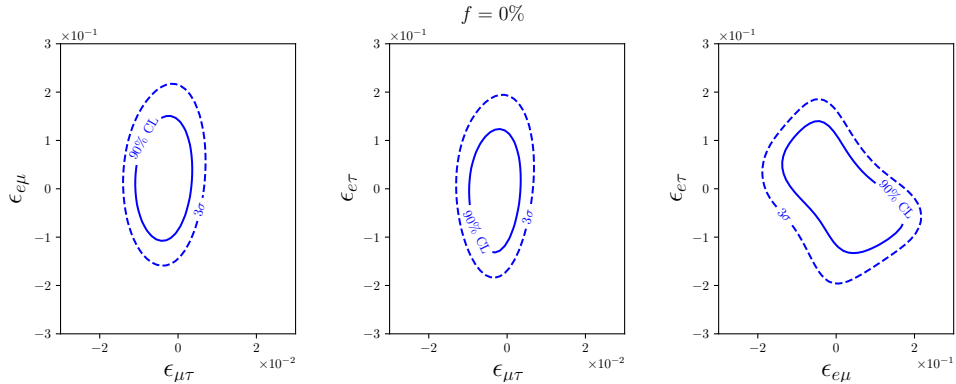


Figure 5.7: Allowed regions for some of the NSI parameters after three years of PINGU data, assuming no uncorrelated systematic error. All plots are made with  $\epsilon_{\tau\tau} = 0$ . The two standard oscillation parameters  $\Delta m_{31}^2$  and  $\theta_{23}$  along with the one NSI parameter not shown have been marginalized out. We observe an anti-correlation between  $\epsilon_{e\mu}$  and  $\epsilon_{e\tau}$ , consistent with our observation of the effect of these parameters on  $P_{\mu e}$  in Fig. 4.6. The values of the standard oscillation parameters are taken from NuFit [5].



# Chapter 6

## Conclusion

In this thesis, we have explored the potential of explaining new physics using detectors handled by the IceCube collaboration. We started off by introducing the Standard Model in Sec. 2.1, and noted that it has several shortcomings. We mentioned the Super-Kamiokande experiment and that their 1998 result found no other explanation than  $\nu_e \rightarrow \nu_\mu$  mixing [2], in direct violation of the Standard Model. We saw that, by adding a right-handed neutrino field, neutrino masses are generated by the Higgs mechanism, thus enabling neutrino oscillations to occur. In Sec. 2.3, we saw how the neutrino mixing matrix could be constructed and derived formulas describing neutrino oscillations in the two- and three-neutrino pictures. Adding a term for matter potential, we then arrived at a Hamiltonian that we used in the time-dependent Schrödinger equation to solve for the oscillation probabilities in matter.

In Sec.4.1, we learned that the LSND experiment found an excess in neutrino events that could be explained by a fourth, sterile, neutrino  $\nu_s$  [18]. We modified the Hamiltonian to incorporate mixing with this new neutrino species, and saw how a eV<sup>2</sup> scale  $\nu_s$  with  $\theta_{24} \neq 0$  affects the  $P_{\bar{\mu}\bar{\mu}}$  oscillation probability by giving us a resonant TeV  $\bar{\nu}_\mu$  disappearance.

We then put the sterile neutrino aside and introduced Non-Standard Interactions (NSI) in Sec.4.2 as a possible example of new physics beyond the Standard Model. We then studied the effects of NSI on the neutrino oscillation probabilities and saw that NSI effects other than those stemming from  $\epsilon_{\mu\tau}$  are not apparent in the TeV region. Moreover, we saw in  $P_{\mu e}$  that we could expect a correlation between  $\epsilon_{e\mu}$  and  $\epsilon_{e\tau}$  in the single-digit GeV range. We also saw that  $\epsilon_{\mu\tau}$  effects were visible on probability level in both the GeV and TeV regions.

First, we described our method in testing the sterile neutrino hypothesis (3+1). We simulated the 86 string IceCube detector with track events, explained in Sec.3.3. After simulating event counts in Sec. 5.1 for the 3+1 hypothesis, we were able to find best-fit parameters of  $\Delta m_{41}^2 = 0.01 \text{ eV}^2$  and  $\theta_{24} = 0.67$  ( $\sin^2 2\theta_{24} = 0.95$ ) at a p-value of 20%. Even though we found a best-fit for two parameters of the sterile neutrino, they are not statistically significant. Hence, we found no evidence of a sterile

neutrino in IceCube data. We also investigated the case when  $\theta_{24} = \theta_{34}$ , which produced an identical contour as in the case with  $\theta_{34} = 0$ . From this observation, we concluded that IceCube is currently insensitive to any impact of  $\theta_{34}$ , with track events alone. However, when opening up the  $\tau$  channel by allowing  $\theta_{34} \neq 0$ , it is possible that with the inclusion of cascade events from  $\nu_\tau$ , IceCube could be able to better observe an impact of  $\theta_{34}$ . With these results, we then completely left the sterile neutrino behind.

In Sec. 5.2, we moved on to the NSI parameter  $\epsilon_{\mu\tau}$  and its effect events captured by IceCube. Using a  $\chi^2$  test, we found that the bound from IceCube on  $\epsilon_{\mu\tau}$  at 90 % confidence level was

$$-0.015 < \epsilon_{\mu\tau} < 0.014 \quad (90\% \text{ CL}) \quad (6.1)$$

for our ‘baseline’ case of 15% uncorrelated systematic uncertainty.

In Sec. 3.4, we moved on and explained our method of simulating a second detector, DeepCore. Armed with simulations possible for this detector, we then continued to explore the possibility of NSI, this time including both track and cascade events and a lower energy region. Using the  $\chi^2$  test defined in Eq. 5.3 and after marginalizing  $\Delta m_{31}^2$  and  $\theta_{23}$  out, we found the following constraints on the NSI parameters at 90% confidence level:

$$\begin{aligned} -0.054 &< \epsilon_{\tau\tau} < 0.067 \\ -0.029 &< \epsilon_{\mu\tau} < 0.0070 \\ -0.12 &< \epsilon_{e\mu} < 0.15 \\ -0.084 &< \epsilon_{e\tau} < 0.15 \quad (\text{all at } 90\% \text{ CL}) . \end{aligned} \quad (6.2)$$

We compared these constraints to literature and found that the bounds for  $\epsilon_{e\mu}$  and  $\epsilon_{e\tau}$  were more stringent than those obtained in [34]. Then, we did a joint  $\chi^2$  test using simulated events from both IceCube and DeepCore. At 90% confidence level, the bound of  $\epsilon_{\mu\tau}$  improved to

$$-0.016 < \epsilon_{\mu\tau} < 0.0070 \quad (90\% \text{ CL}) . \quad (6.3)$$

In Sec. 3.5 we described our method of simulating a proposed upgrade to the IceCube array: PINGU. Since PINGU is not yet live, we produced data for it assuming a standard 3+0 hypothesis with parameters from [5]. After a  $\chi^2$  analysis, we obtained the following constrains on the NSI parameters at 90% confidence level:

$$\begin{aligned} -0.049 &< \epsilon_{\tau\tau} < 0.057 \\ -0.010 &< \epsilon_{\mu\tau} < 0.011 \\ -0.137 &< \epsilon_{e\mu} < 0.11 \\ -0.132 &< \epsilon_{e\tau} < 0.125 \quad (\text{all at } 90\% \text{ CL}) . \end{aligned} \quad (6.4)$$

After that, we did a joint  $\chi^2$  analysis combining IceCube, DeepCore and simulated PINGU events to further constrict  $\epsilon_{\mu\tau}$ . The bound at 90% confidence level obtained was

$$-0.010 < \epsilon_{\mu\tau} < 0.0060. \quad (90\% \text{ CL}) \quad (6.5)$$

We were then able to draw the conclusion that we expect PINGU to successfully be able to observe the impact of NSI. Moreover, a joint analysis between PINGU and at least one of the other detectors under the IceCube collaboration will be able to constrain the parameters even further. We saw that can expect PINGU to be more sensitive to NSI effects than DeepCore. We were also able to see that when constraining  $\epsilon_{e\mu}$  and  $\epsilon_{e\tau}$  from the negative side, we can expect the result to be highly dependent on the systematic uncertainty of PINGU.

Finally, we simulated the event count in PINGU, allowing  $\epsilon_{\mu\tau}$ ,  $\epsilon_{e\mu}$ , and  $\epsilon_{e\tau}$  to vary, but setting  $\epsilon_{\tau\tau} = 0$ . After and marginalizing out  $\Delta m_{31}^2$ ,  $\theta_{23}$ , and  $\epsilon_{\mu\tau}$ , we saw that the effect of  $\epsilon_{e\mu}$  and  $\epsilon_{e\tau}$  on  $P_{\mu e}$  had indeed propagated through to the event count, manifesting as an anti-correlation between the  $\epsilon_{e\mu}$  and  $\epsilon_{e\tau}$  at both 90% and  $3\sigma$  confidence levels. No other pair of NSI parameters were observed to have a significant correlation.



# Bibliography

- [1] C. Giunti and C. W. Kim, Fundamentals of Neutrino Physics and Astrophysics, Oxford University Press.
- [2] Super-Kamiokande Collaboration et al., Evidence for Oscillation of Atmospheric Neutrinos 81 (8) 1562–1567. doi:10.1103/PhysRevLett.81.1562.
- [3] B. Pontecorvo, Mesonium and antimesonium Vol: 33.  
URL <https://www.osti.gov/biblio/4343073>
- [4] Z. Maki et al., Remarks on the Unified Model of Elementary Particles 28 (5) 870–880. doi:10.1143/PTP.28.870.
- [5] I. Esteban et al., The fate of hints: Updated global analysis of three-flavor neutrino oscillations 2020 (9) 178. doi:10.1007/JHEP09(2020)178.
- [6] A. M. Dziewonski and D. L. Anderson, Preliminary reference Earth model 25 (4) 297–356. doi:10.1016/0031-9201(81)90046-7.
- [7] M. Honda, HKKM2014 flux table one year average.  
URL <http://www.icrr.u-tokyo.ac.jp/~mhonda/nflux2014/index.html>
- [8] M. Honda et al., Atmospheric neutrino flux calculation using the NRLMSISE-00 atmospheric model 92 (2) 023004. doi:10.1103/PhysRevD.92.023004.
- [9] The IceCube Collaboration, Measurement of atmospheric tau neutrino appearance with IceCube DeepCore 99 (3) 032007. doi:10.1103/PhysRevD.99.032007.
- [10] C. Weaver, Evidence for Astrophysical Muon Neutrinos from the Northern Sky.
- [11] The IceCube Gen2 Collaboration, Letter of Intent: The Precision IceCube Next Generation Upgrade (PINGU). arXiv:1401.2046.
- [12] The IceCube Collaboration, All-sky point-source IceCube data: Years 2010–2012. doi:10.21234/B4F04V.
- [13] The IceCube Collaboration, Search for sterile neutrinos with one year of IceCube data.  
URL <https://icecube.wisc.edu/data-releases/2016/06/search-for-sterile-neutrinos-with-one-year-of-icecube-data/>

- [14] The IceCube Collaboration et al., Searching for eV-scale sterile neutrinos with eight years of atmospheric neutrinos at the IceCube Neutrino Telescope 102 (5) 052009. doi:[10.1103/PhysRevD.102.052009](https://doi.org/10.1103/PhysRevD.102.052009).
- [15] The IceCube Collaboration, Three-year high-statistics neutrino oscillation samples. doi:[10.21234/ac23-ra43](https://doi.org/10.21234/ac23-ra43).
- [16] The IceCube Collaboration, Measurement of Atmospheric Neutrino Oscillations at 6–56 GeV with IceCube DeepCore 120 (7) 071801. doi:[10.1103/PhysRevLett.120.071801](https://doi.org/10.1103/PhysRevLett.120.071801).
- [17] The IceCube Collaboration, IceCube Upgrade Neutrino Monte Carlo Simulation. doi:[10.21234/qfz1-yh02](https://doi.org/10.21234/qfz1-yh02).
- [18] LSND Collaboration et al., Evidence for  $\tau \rightarrow e$  Oscillations from the LSND Experiment at the Los Alamos Meson Physics Facility 77 (15) 3082–3085. doi:[10.1103/PhysRevLett.77.3082](https://doi.org/10.1103/PhysRevLett.77.3082).
- [19] T. M. Collaboration, A Search for Electron Neutrino Appearance at the Delta  $m^2 \sim 1 \text{ eV}^2$  Scale 98 (23) 231801. arXiv:[0704.1500](https://arxiv.org/abs/0704.1500), doi:[10.1103/PhysRevLett.98.231801](https://doi.org/10.1103/PhysRevLett.98.231801).
- [20] Particle Data Group et al., Review of Particle Physics 2020. doi:[10.1093/ptep/ptaa104](https://doi.org/10.1093/ptep/ptaa104).
- [21] P. Collaboration et al., Planck 2018 results. VI. Cosmological parameters 641 A6. arXiv:[1807.06209](https://arxiv.org/abs/1807.06209), doi:[10.1051/0004-6361/201833910](https://doi.org/10.1051/0004-6361/201833910).
- [22] P. F. de Salas and S. Pastor, Relic neutrino decoupling with flavour oscillations revisited 2016 (07) 051. doi:[10.1088/1475-7516/2016/07/051](https://doi.org/10.1088/1475-7516/2016/07/051).
- [23] M. B. Gavela et al., Minimal Flavour Seesaw Models 2009 (09) 038–038. arXiv:[0906.1461](https://arxiv.org/abs/0906.1461), doi:[10.1088/1126-6708/2009/09/038](https://doi.org/10.1088/1126-6708/2009/09/038).
- [24] J. Salvado et al., Non-standard interactions with high-energy atmospheric neutrinos at IceCube 2017 (1) 141. arXiv:[1609.03450](https://arxiv.org/abs/1609.03450), doi:[10.1007/JHEP01\(2017\)141](https://doi.org/10.1007/JHEP01(2017)141).
- [25] Y. Farzan and M. Tortola, Neutrino oscillations and Non-Standard Interactions. arXiv:[1710.09360](https://arxiv.org/abs/1710.09360).
- [26] T. Ohlsson, Status of non-standard neutrino interactions 76 (4) 044201. arXiv:[1209.2710](https://arxiv.org/abs/1209.2710), doi:[10.1088/0034-4885/76/4/044201](https://doi.org/10.1088/0034-4885/76/4/044201).
- [27] P. Coloma et al., A COHERENT enlightenment of the neutrino Dark Side 96 (11) 115007. arXiv:[1708.02899](https://arxiv.org/abs/1708.02899), doi:[10.1103/PhysRevD.96.115007](https://doi.org/10.1103/PhysRevD.96.115007).
- [28] The IceCube Collaboration, All-flavor constraints on nonstandard neutrino interactions and generalized matter potential with three years of IceCube DeepCore data. arXiv:[2106.07755](https://arxiv.org/abs/2106.07755).

- [29] A. Esmaili and A. Y. Smirnov, Probing Non-Standard Interaction of Neutrinos with IceCube and DeepCore 2013 (6) 26. [arXiv:1304.1042](https://arxiv.org/abs/1304.1042), doi:10.1007/JHEP06(2013)026.
- [30] S. Choubey and T. Ohlsson, Bounds on Non-Standard Neutrino Interactions Using PINGU 739 357–364. doi:10.1016/j.physletb.2014.11.010.
- [31] T. Ohlsson et al., Effects of nonstandard neutrino interactions at PINGU 88 (1) 013001. doi:10.1103/PhysRevD.88.013001.
- [32] M. Honda et al., Calculation of atmospheric neutrino flux using the interaction model calibrated with atmospheric muon data. doi:10.1103/PhysRevD.75.043006.
- [33] M. Maltoni and T. Schwetz, Testing the statistical compatibility of independent data sets 68 (3) 033020. [arXiv:hep-ph/0304176](https://arxiv.org/abs/hep-ph/0304176), doi:10.1103/PhysRevD.68.033020.
- [34] S. Demidov, Bounds on non-standard interactions of neutrinos from IceCube DeepCore data 2020 (3) 105. doi:10.1007/JHEP03(2020)105.
- [35] The IceCube Collaboration, Search for nonstandard neutrino interactions with IceCube DeepCore 97 (7) 072009. doi:10.1103/PhysRevD.97.072009.